國立臺灣大學理學院化學系

博士論文

Department of Chemistry
College of Science
National Taiwan University

Doctoral Dissertation

合成與探索發色團之光物理性質與光動力療法應用

Synthesis and Exploitation of Chromophores for Their Photophysics and Application of Photodynamic Therapy

李曜麟

Yao-Lin Lee

指導教授：周必泰 博士

Advisor: Pi-Tai Chou, Ph.D.

中華民國 111 年 8 月

August, 2022

doi:10.6342/NTU202201631

國立臺灣大學博士學位論文
口試委員會審定書

合成與探索發色團之光物理性質與光動力療法應用

Synthesis and Exploitation of Chromophores for Their Photophysics and Application of Photodynamic Therapy

本論文係 李曜麟 （學號 D06223117 ）在國立臺灣大學化學系完成之博士學位論文，於民國 111 年 1 月 6 日承下列考試委員審查通過及口試及格，特此證明。

口試委員：

（簽名）

（指導教授）

系主任、所長 （簽章）

doi:10.6342/NTU202201631

謝辭

時光飛逝日月如梭，不才北漂接近十年，看到許多學長姐畢業高就，如今終於換到我了，感慨自己並無太過驚人的研究成果可以分享，但還是對一路上指導我幫助我的師長和朋友深深的感謝。

首先感謝我的指導教授周必泰老師給我充分的知識與資源，讓我能在研究之路上無後顧之憂，感謝何佳安老師與周易德博士在生物實驗方面的大力幫助，再來感謝汪根欉老師、吳耀庭老師與洪文誼老師擔任我的口試評委，幫助我修訂論文並提供建設性的意見，我也要感謝我在大學時期的指導教授陳昭岑老師她教授我嚴謹的有機合成技巧與訓練。再來是我的同事們，感謝凱信學長和偉志學長在實驗、論文修訂上的幫助，感謝知行與其錡在光譜測量與理論計算上的支援，感謝大均學長、宇強與郁璇時常與我討論實驗刺激成長，感謝雨軒、瀞涵和聖夫常常陪我聊天度過平淡的實驗生活。最後要感謝我的家人給我心理和經濟上的支援，讓我在遇到低谷時也能重新爬起。

最後的最後我想感謝五年前的自己做了正確的選擇，當時看似大膽的決定最後也能順利達成，也許這就是天助自助者。期勉未來 PTC Lab 的學弟妹們能跟上周老師的腳步，一起追逐最新穎的研究成果。

學生 李曜麟 20220720

doi:10.6342/NTU202201631

摘要

量子產率小於 1%的吩噻嗪限制了它做更多的應用而硝基已知的螢光淬滅基，有趣的是當我們將兩者結合在一起時會組成電荷轉移態進而增強螢光放射。首先將在吩噻嗪 3 號為上分別接上推電子基 (OMe) 和拉電子基 (CN, CHO, NO_2) 命名為 **PTZ-OMe, PTZ-CN**, **PTZ-CHO** and **PTZ-NO_2**, 理論計算顯示 **PTZ** 和 **PTZ-OMe** 的過度態是由 π 軌域的 HOMO 到 π*軌域與未成對電子混成的 LUMO 而成，使得其過度態屬於軌域部分禁止的，對比之下拉電子基可以降低硫的未成對電子軌域使其無法影響到 π*軌域，讓 **PTZ-CN**, **PTZ-CHO** and **PTZ-NO_2** 屬於 π-π*軌域允許的過度態，而計算結果與光物理性質相符合，相比於 **PTZ** 和 **PTZ-OMe** 的不放光，吩噻嗪接上拉電子基使得放光增強，值得一提的是 **PTZ-NO_2** 在非極性溶劑下具有 100%的螢光量子產率。最後在電化學分析上，我們發現拉電子基可以降低 LUMO 的能量讓硫的未成對電子軌域無法參與第一激發態的過渡。這個研究證明一個良好的分子設計去調控吩噻嗪衍生物的過度態進而影響到其放光。

關鍵字: 吩噻嗪、硝基、電荷轉移、未成對電子軌域

doi:10.6342/NTU202201631

摘要

烷基或苯基為取代基於苯芘二醯亞胺為主體設計一個具有同步顯影追蹤與針對性光動力療法的分子。經過硫化反應之後得到一取代至四取代硫的產物，在此研究中我們以苯基取代的苯芘二醯亞胺為主體命名為 **1S-PDI-D**, **2S-*cis*-PDI-D**, **2S-*trans*-PDI-D**, **3S-PDI-D** 和 **4S-PDI-D**。在所有的硫化分子中光物理性質跟氮上取代基與硫化數量有相關。在吸收光譜中，主要的吸收峰屬於 $S_0 \rightarrow S_2(\pi\pi^*)$的過度態並且會隨著硫化數增加而紅移。最低能階單重態 $S_1(n\pi^*)$屬於過度態禁止的構型而且其能階與硫化數量與不同取代基有關，在本篇中苯基取代硫化苯芘二醯亞胺的能階低於烷基取代的苯芘二醯亞胺。在室溫下的正常氣體或是除氣條件下，所有的合成的硫化化合物皆不放螢光。經由瞬態吸收光譜與理論計算的支持下，激發態具有超快的系間交叉 $S_1(n\pi^*) \rightarrow T_1(\pi\pi^*)$將能量轉移到三重態。由理論計算可得最低階三重態的能量排序為 **1S-PDI-D** (1.10 eV) > **2S-*cis*-PDI-D** (0.98 eV) ~ **2S-*trans*-PDI-D** (0.98 eV) > **3S-PDI-D** (0.87 eV) > **4S-PDI-D** (0.77 eV)，而 **1S-PDI-D** 比單氧激發態更高因此具有 100%的單氧產率並以此為基底作成兩個目標化合物:第一是將兩端接上具有選擇性的胜肽 FC131 命名為 **1S-FC131**，第二是一端接 FC131 一端接 Cyanine 5 命名為 **Cy5-1S-FC131**。在細胞實驗，**1S-FC131** 具有光動力療法且能夠辨認 A549 細胞而非另外三種正常細胞(WI-38, IMR90 and HEL299)。**Cy5-1S-FC131** 被證實具有中等選擇性光動力療法與同步螢光顯影在癌細胞中，在 A549 xenografted 腫瘤老鼠中，兩種藥物皆具有良好的抗腫瘤能力。

關鍵字: 苯芘二醯亞胺、FC131、Cy5, 光動力療法、選擇性、顯影

doi:10.6342/NTU202201631

Abstract

Phenothiazine (PTZ) with weak fluorescent quantum yield (>1% in cyclohexane) limit its derivatives for extensive application. Besides, a strong electron withdrawing group, nitro group (NO_2), was a popular fluorescent quencher. Unexpectedly, we combined both moieties together to form strong charge transfer model to enhance their emission. First, PTZ were coupled with electron-donating group (OMe) and electron-withdrawing group (CN, CHO, NO_2) at 3 position to form **PTZ-OMe**, **PTZ-CN**, **PTZ-CHO** and **PTZ-NO_2,** respectively. Second, theoretical calculation showed that the transitions of **PTZ-OMe** and **PTZ** were mainly from HOMOs of π orbitals to LUMOs dominated by π mixed with nonbonding orbitals of sulfur, meaning its transition were partially forbidden. Conversely, the modification of electron withdrawing groups could reduce their energy levels of the nonbonding orbital from sulfur on **PTZ**, therefore blocking the incorporation of nonbonding orbital of sulfur with their π* orbital of **PTZ** to LUMO, and hence their allowed π-π* transition becomes major transition. Third, the series compounds were synthesized and measured their photophysical properties. The phenothiazines with EWGs displayed increased fluorescence rather than **PTZ** or **PTZ-OMe**. Worth to talk about that, **PTZ-NO_2** attained 100% photoluminescent quantum yield in the nonpolar solvent. Last, in electrochemical analysis, we found that the EWGs reduced the LUMO's energy, which prevent nonbonding of sulfur incorporating in the first excited state. This research developed a series of PTZ analogues with a tunable transition and emission through a wise molecular design.

Keyword: phenothiazine, nitro group, charge transfer, nonbonding orbital

doi:10.6342/NTU202201631

Abstract

Bearing an aim of simultaneous imaging tracking and targeted photodynamic therapy (PDT), the core chromophore 3,4,9,10-perylenetetracarboxylic diimide (PDI) is anchored by alkyl or phenyl substituents at the imide N-site, followed by delicate thionation, yielding a comprehensive series of thione products. In this study, the phenyl derivatives endowed with n= 1, 2, 3 and 4 thione groups, namely **1S-PDI-D**, **2S-*cis*-PDI-D**, **2S-*trans*-PDI-D**, **3S-PDI-D** and **4S-PDI-D**, respectively, are the main focus. For all studied **nS-PDI**s, the photophysical properties are dependent of the N-substitution and number of anchored thiones, where the observed prominent lower lying absorption is assigned to be the $S_0 \rightarrow S_2$ ($\pi\pi^*$) transition and is red shifted significantly upon increasing number of thione. The lowest lying singlet state is ascribed to an $S_1(n\pi^*)$ configuration, which is a transition forbidden state and its energy depends on not only the thione group but also the N-substitution, being lower in N-phenyl substitution (cf. N-alkyl substitution) at the same number of thione substitution among all n**S-PDI**s. All synthesized n**S-PDI**s are virtually non-emissive in both aerated and degassed solution at room temperature. Supported by femtosecond transient absorption and computation, the excited-state relaxation is dominated by fast $S_1(n\pi^*) \rightarrow T_1(\pi\pi^*)$ intersystem crossing (ISC), resulting in ~100% triplet population. The lowest lying $T_1(\pi\pi^*)$ energy is calculated to be in the order of **1S-PDI-D** (1.10 eV) > **2S-*cis*-PDI-D** (0.98 eV) ~ **2S-*trans*-PDI-D** (0.98 eV) > **3S-PDI-D** (0.87 eV) > **4S-PDI-D** (0.77 eV), where the T1 energy of **1S-PDI-D** is close but higher than that (0.97 eV) of the $^1O_2$ $^1\Delta_g$ state, rendering 100% yield of $^1O_2$. **1S-PDI-D** is further modified by two synthetic strategies: 1. its conjugation with peptide FC131 on the two terminal sides, forming **1S-FC131** and 2. the linkage of peptide FC131 and Cyanine5 dye on each terminal side, yielding **Cy5-1S-FC131**. *In vitro* experiments prove that **1S-FC131** is able to recognize A549 cells out of other three lung normal cells (WI-

doi:10.6342/NTU202201631

38, IMR90 and HEL299) and perform effective PDT. **Cy5-1S-FC131** further demonstrate modest selective PDT and simultaneous fluorescence imaging on the cancer cells. *In vivo*, both molecular composites also demonstrate outstanding antitumor ability in A549 xenografted tumor mouse.

Keyword: Perylene diimide, FC131, Cy5, photodynamic therapy, selectivity, imaging

doi:10.6342/NTU202201631

Contents

doi:10.6342/NTU202201631

doi:10.6342/NTU202201631

Figure Contents

doi:10.6342/NTU202201631

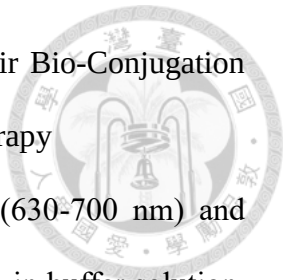

doi:10.6342/NTU202201631

doi:10.6342/NTU202201631

doi:10.6342/NTU202201631

Table Contents

doi:10.6342/NTU202201631

Chemical Structure Index

Part I

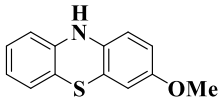

PTZ-OMe

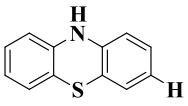

PTZ

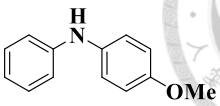

DPA-OMe

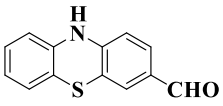

PTZ-CHO

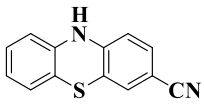

PTZ-CN

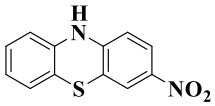

PTZ-NO$_2$

Part II

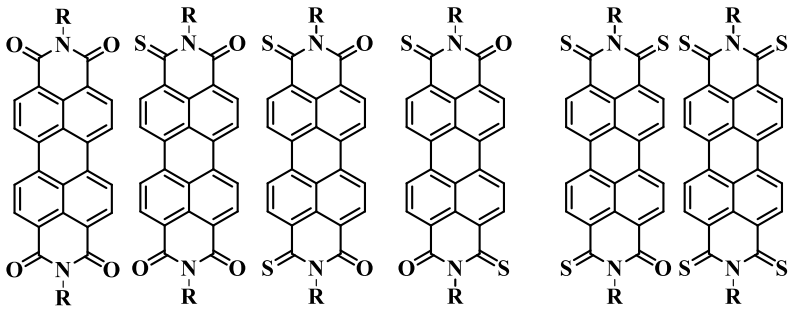

PDI-P 1S-PDI-P 2S-*cis*-PDI-P 2S-*trans*-PDI-P

R:

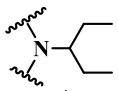

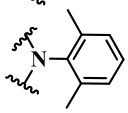

PDI-D 1S-PDI-D 2S-*cis*-PDI-D 2S-*trans*-PDI-D 3S-PDI-D 4S-PDI-D

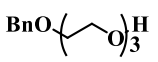

1

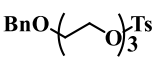

2

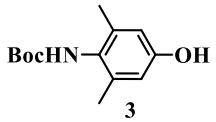

3

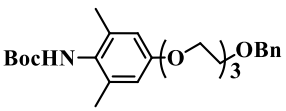

4

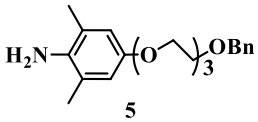

5

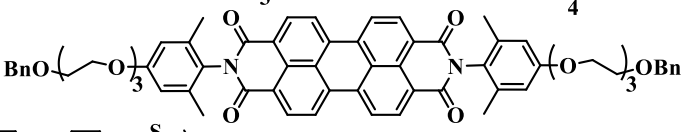

6

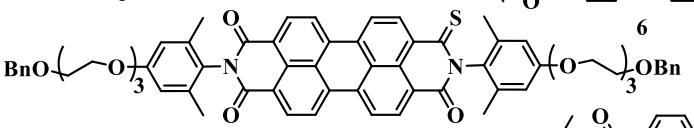

7

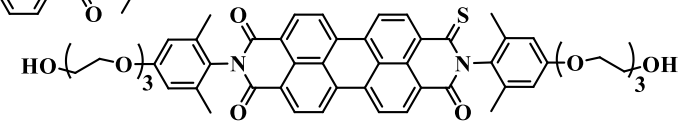

8

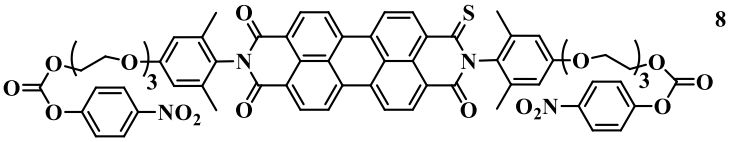

1S-NO$_2$

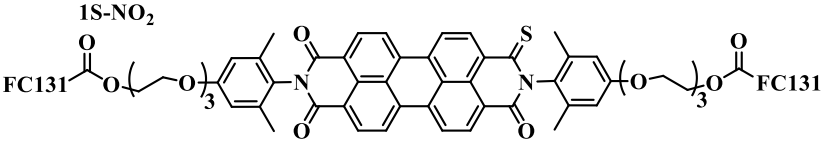

1S-FC131

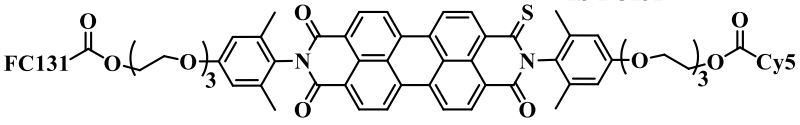

Cy5-1S-FC131

doi:10.6342/NTU202201631

doi:10.6342/NTU202201631

Part I. Tuning Electron-Withdrawing Strength on Phenothiazine Derivatives: Achieving 100% Photoluminescence Quantum Yield by NO_2 Substitution

1.1 Introduction

Phenothiazine (**PTZ**)-based derivatives have applied in many different aspects, like dye-sensitized solar cells (DSSCs),[1] thermally activated delayed fluorescence materials (TADF),[2] pharmaceutical industry,[3] supramolecular host–guest chemistry,[4] and organic light-emitting diodes sources.[5] Anthracene-shaped heterocyclic **PTZ** possessed sulfur and nitrogen atoms with nonbonding orbitals in the middle six-membered ring in Figure 1-1. Therefore, electron density of **PTZ** was higher than other heterocyclic congeners, including carbazole, acridine, and. phenoxazine (**PXZ**)[2f, 6] Except for these, **PTZ** could be converted into distinct states after treatments, like neutral, oxygenated sulfoxide, and cation radical forms, simplifying synthetic strategies in the pharmaceutical chemistry.[7] On the other hand, versatile biosynthesis pathway also encouraged us to develop **PTZ** derivatives for fluorescent biosensing. Nevertheless, their practical and extensive applications were hampered by their weak photoluminescence quantum yields (PLQYs) in the solid as well as solution states.[8] Compared with **PTZ**, Phenoxazine (**PXZ**) ,replacing sulfur in **PTZ** with oxygen, possessed a mild fluorescent yield (PLQY=2.7% in cyclohexane).[9] This comparison implied the non-negligible influences of sulfur atom in **PTZ** on their transition and emission.[10] Hence, the electron rich sulfur atom with higher energy level of nonbonding orbitals, which caused that the n-π* state was raised in close proximity to the π-π* state in **PTZ**. These two close states could incorporate and let the transition of PTZ become partially forbidden. Moreover, the nonplanarity in ground state and twisting motions in the excited state of the **PTZ** could also increase nonradiative relaxation and casue their weak fluorescence for **PTZ** in

doi:10.6342/NTU202201631

Figure1-1.

On the other hand, nitro group, NO_2, was a well-known electron withdrawing group in organic synthesis, applied on extensive areas e.g. industrial materials,[11] military weapon,[12] pharmaceutical and agricultural ingredients.[13] However, the nitro group in chromophore was usually regarded as a fluorescent quencher.[14] This photophysical property has been attributed to in two main reasons. First, the lone pair of nitro group would provide the resource of nonbonding orbital which locates at relatively high energy level. As a result, the nitrated compounds often possessed n-π^* transition in the first excited state.[15] Second, the nitro group as a strong electron withdrawing group could form the charge transfer state after excitation. Compared to the localized excited state, the charge transfer state has stronger solvatochromism and smaller energy gap between excited state and ground state, suggesting that their emission could be apt to be quenched by solvent or relaxed in nonradiative pathway due to the energy gap law.[16] In order to overcome the quenching mechanism of nitro group, the scientists have provided several possible strategies. One of them was extension of aromatic ring. An enlarged aromatic system could enhance the highest occupied π orbital energy and prevent the incorporation of the nonbonding orbital of nitro group. [17] However, the large aromatic ring could not only raise the π-orbital energy but also reduce the energy gap between highest occupied molecular orbital (HOMO) and lowest occupied molecular orbital (LUMO), which might increase the rate of nonradiative pathway based on energy gap law.[18] Moreover, the enlarged structure possessed more degree of freedom for rotation and vibration. On the other hand, the design of optical electron transfer system was also an available strategy. Optical electron transfer system has strong interaction between donor and acceptor and large overlap between HOMO and LUMO, meaning that this system could have high extinction coefficient and emission.[19]

doi:10.6342/NTU202201631

Herein, in our work, we wanted to connect the two “dark” moieties together in order to design an enhancing emissive compound via optical electron transfer system. In our design, we chose three electron withdrawing groups: cyanide (**PTZ-CN**), aldehyde (**PTZ-CHO**) and nitro group (**PTZ-NO$_2$**) to **PTZ** at 3 position directly in Figure 1-1. As a control molecule, we gained methoxy-substituted **PTZ-OMe** as a typical electron donating group and got commercially available **PTZ**. The 3-substitued **PTZ** would strongly affect the molecular properties. First, 3-EWG **PTZ** could have the inductive effect on sulfur at meta position to lower the lone-pair electron energy, which prevented fluorescence quenching mechanism of **PTZ**. Second, these substitutes on 3 position as an acceptor and 2^o amine at 10-position as a donor could consist of strong charge transfer character. Owing to the different degree of withdrawing ability, we could tune their emissive wavelength and enhance their intensity. In our experiment, we would like to conduct the theoretical calculation to confirm our design, and then afford all five target compounds by organic synthesis to affirm their photophysical properties. At last, cyclic voltammetry data was used for demonstration of the fluorescent mechanism.

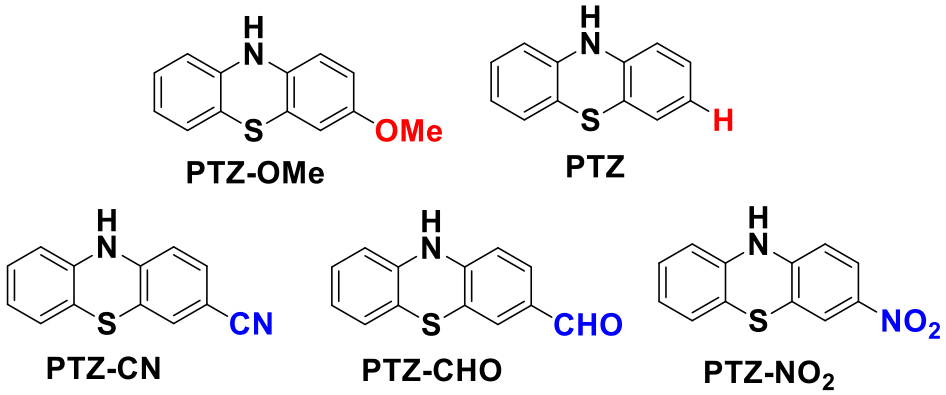

Figure 1- 1 Chemical structures of **PTZ** and its analogues modified at C3-position.

doi:10.6342/NTU202201631

1.2 Results and Discussions

1.2.1 Theoretical Calculation

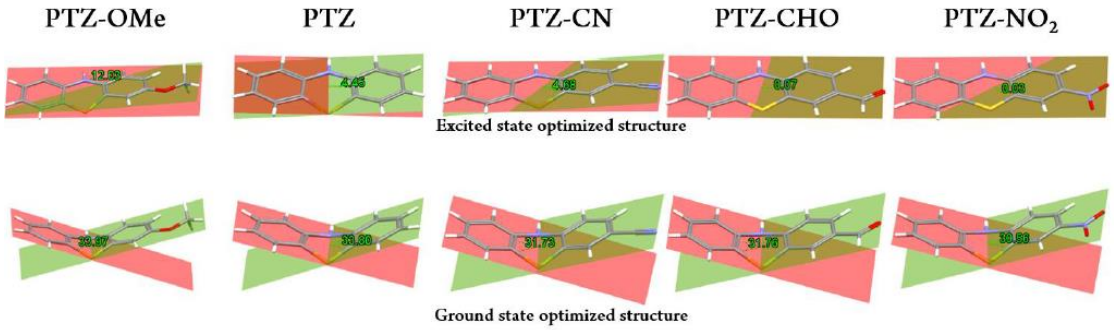

Figure 1- 2 Ground-state and excited-state optimized structure with bending angle, which was defined as follow. Red plane was calculated from six carbons in the left benzene ring, green plane was calculated from six carbons in the right benzene ring, and the bending angle (θ) was defined as the smaller angle between red and green plane.

To verify our assumption of ground and excited state of all five target compounds, their theoretical calculations were ordered by time-dependent density functional theory (TD-DFT) with 6-31+G (d,p) basis set by M062X functional. Despite of B3LYP functional widely used for theoretical calculation, the wavelengths of absorbance and emission from M062X functional existed less deviations from our experimental data. Thus, we present theoretical calculation of the M062X functional here.

In the geometric optimization of all five target compounds in the ground states (S_0), they possessed a bending geometry in the ground state due to the electron-rich and large size of sulfur. In Figure 1-2, the bending angle (θ) was defined by the angle intersected by the two benzenes of **PTZ.** The bending angles (θ) of the five target compounds in the ground state decreased in the order **PTZ-OMe** (33.97) > **PTZ** (33.80) > **PTZ-CN** (31.73) & **PTZ-CHO** (31.76) > **PTZ-NO$_2$** (30.56), and however, the bending angles of the five target compounds in the lowest excited state (S_1) decreased in the order **PTZ-OMe** (12.03)

doi:10.6342/NTU202201631

> **PTZ** (4.45) & **PTZ-CN** (4.68) > **PTZ-CHO** (0.07) > **PTZ-NO_2** (0.03). Though this was a common result in **PTZ** and other heterocyclic derivatives such as acridine and phenoxazine, electron withdrawing groups indeed resulted in the structural planarization. About **PTZ-NO_2** and **PTZ-CHO** with much more planar than other three products, we proposed that the electron density of sulfur would be reduced due to the inductive effect of nitro and aldehyde group. A planar structure in the conjugated system could form a better charge transfer system and enhancing emission. This was a positive implication for us that **PTZ-NO_2** and **PTZ-CHO** would be the standard charge transfer molecules as our design.

doi:10.6342/NTU202201631

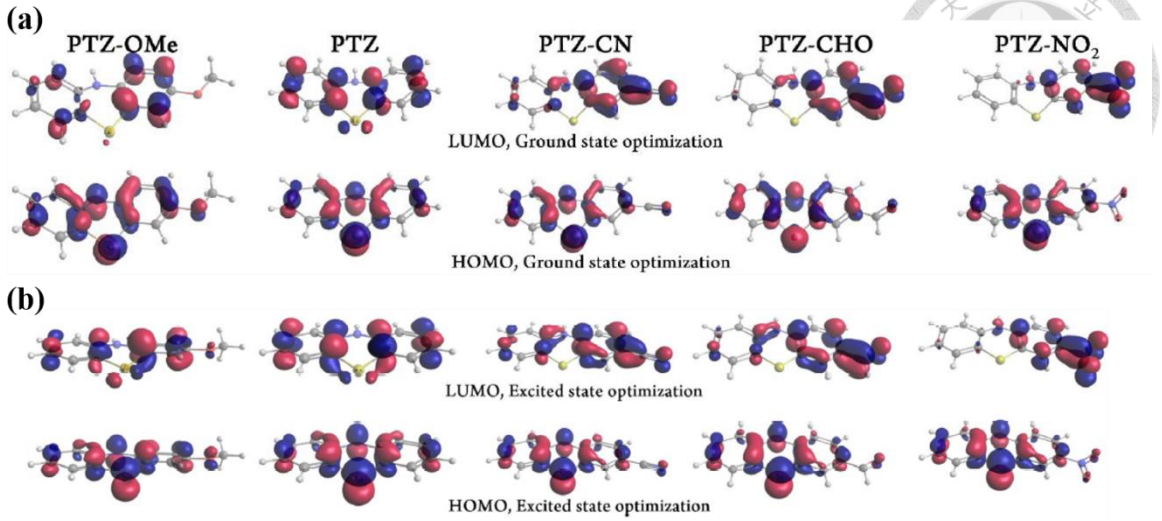

Figure 1- 3 (a) Ground-state (b) Excited-state optimization of LUMO (upper) and HOMO (lower) orbitals for five compounds in cyclohexane.

Table 1- 1 Calculated wavelength (λ), oscillator strength (f) and orbital transition for five titled molecules with m062x

	Absorption (nm)	f	Contribution	Weight	Emission (nm)	f	Contribution	Weight
PTZ-OMe	302	0.0041	HOMO→LUMO	68%	426	0.0061	HOMO←LUMO	96%
PTZ	303	0.0007	HOMO→LUMO	92%	420	0.008	HOMO←LUMO	97%
PTZ-CN	323	0.0741	HOMO→LUMO	85%	443	0.0559	HOMO←LUMO	95%
PTZ-CHO	340	0.1248	HOMO→LUMO	83%	461	0.1067	HOMO←LUMO	92%
PTZ-NO_2	362	0.1876	HOMO→LUMO	89%	496	0.1694	HOMO←LUMO	92%

We collected both ground and excited state orbitals in Figure 1-3. In order to predict their photophysics, we implemented a geometric optimization of the lowest-lying excited states (S_1) in Figure 1-3b and data in Table 1-1. The LUMOs of **PTZ-OMe** and **PTZ** in the excited state were majorly distributed over the **PTZ** moiety with an apparent contribution of lone pair electron of sulfur in **PTZ**, suggesting locally excited state transition. These data revealed that the lowest-lying transition consisted of π-π* in character and partially nonbonding character from the sulfur. In comparison, introducing electron withdrawing groups into **PTZ** led to their apparent charge disconnection between LUMO and HOMO in the ground and excited state. In these three compounds, there were

doi:10.6342/NTU202201631

high electron density on the benzene substituted EWGs in the LUMO and another benzene in the HOMO. Except for this, there were no electron density on the sulfur in the middle six-member ring, meaning that the π-orbital contribution surpassed the nonbonding orbital from sulfur due to the inductive effect of EWGs. It was worth noting that HOMO of **PTZ-NO$_2$** was π orbital rather than nonbonding orbital. It was because that the coupling of strong EWG (nitro) and EDG (**PTZ**) elongated the conjugation of charge transfer system, which let π-π* transition be majority. According to theoretical calculation of five target compounds, **PTZ-OMe** and **PTZ** might have weak emission due to participation of nonbonding orbital from sulfur, and on the other side, **PTZ-CN**, **PTZ-CHO** and **PTZ-NO$_2$** were standard optical charge transfer model as our design. Calculated wavelength, oscillator strength and orbital transition of five molecules were collected in Table 1-1. Compared to the oscillator strengths of **PTZ-OMe** (0.0041/0.0061) and **PTZ** (0.0007/0.008), **PTZ-CN** (0.0741/0.0559), **PTZ-CHO** (0.1248/0.1067) and **PTZ-NO$_2$** (0.1873/0.1694) possessed higher oscillator strengths. Based on the theoretical calculation, PTZ conjugated with EWGs would form the enhancing fluorescent charge transfer systems which prevented nonbonding orbital of sulfur or oxygen incorporating in HOMO/LUMO.

doi:10.6342/NTU202201631

1.2.2 Synthetic Methods

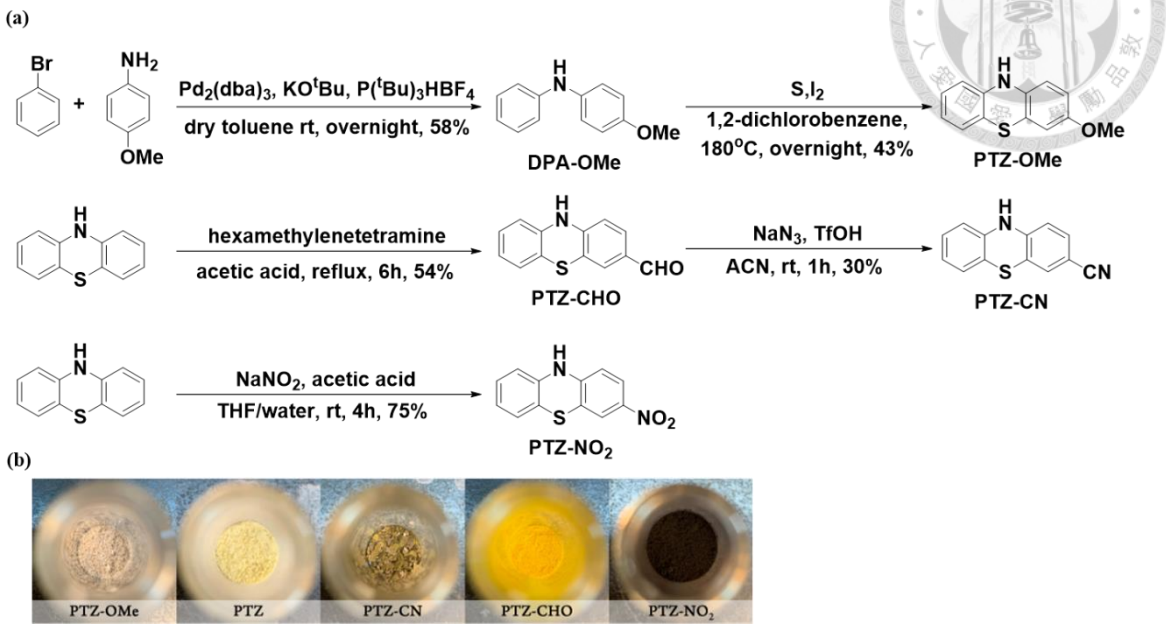

Figure 1- 4 (a) Synthesis routes of five titled molecules. (b) The appearance of titled compounds under regular indoor light.

the synthetic routes of five target compounds were shown in Figure 1-4a and experimental section was collected in the Supporting information. Five target compounds were featured by ^{1}H-NMR, ^{13}C-NMR, mass and FT-IR spectroscopy. The photograph of the five compounds were displayed in Figure 1-4b. First, 4-methyloxyaniline was coupled with bromobenzene by Pd-catalyst in dry toluene overnight to afford **DPA-OMe** (58%).[20] **DPA-OMe** was cyclized by reaction with sulfur and iodine in refluxed 1,2-dichlorobenzene to obtain **PTZ-OMe** (43%).[21] Second, **PTZ** was refluxed with hexamethylenetetramine in acetic acid in 6 hours to afford **PTZ-CHO** (54%) via Duff reaction.[22] Further, **PTZ-CHO** could transfer to **PTZ-CN** (30%) by Schmidt-type reaction mediated by triflic acid.[23] Last, **PTZ** was reacted with sodium nitrite in THF/water/acetic acid (5/2/1.5) in room temperature for 4 hours to yield **PTZ-NO$_2$** (75%).[24] The proposed mechanism of nitration was shown in Figure 1-5. Nitrite group

doi:10.6342/NTU202201631

protonated by acetic acid could be resonated with nitro group. Activated phenothiazine with partial negative charge at para position as a nucleophile attacked nitro group and then protonated by H_3O^+ to afford **PTZ-NO2**.

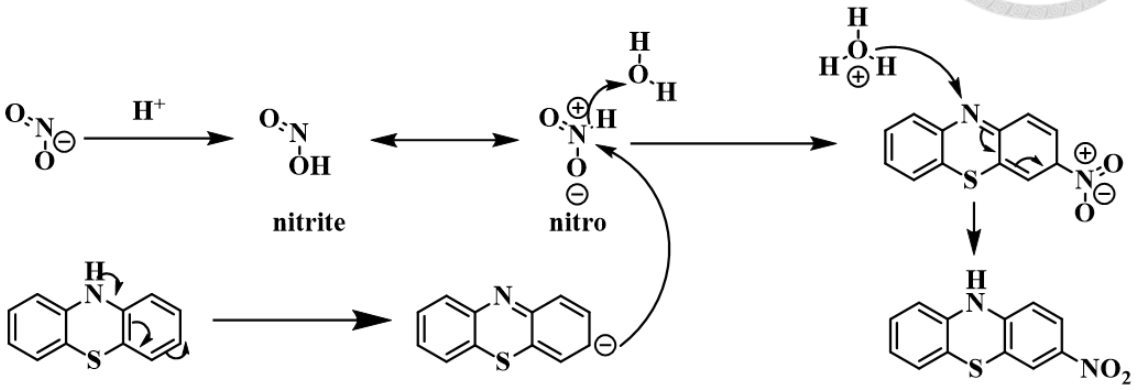

Figure 1- 5. the proposed mechanism of nitration

doi:10.6342/NTU202201631

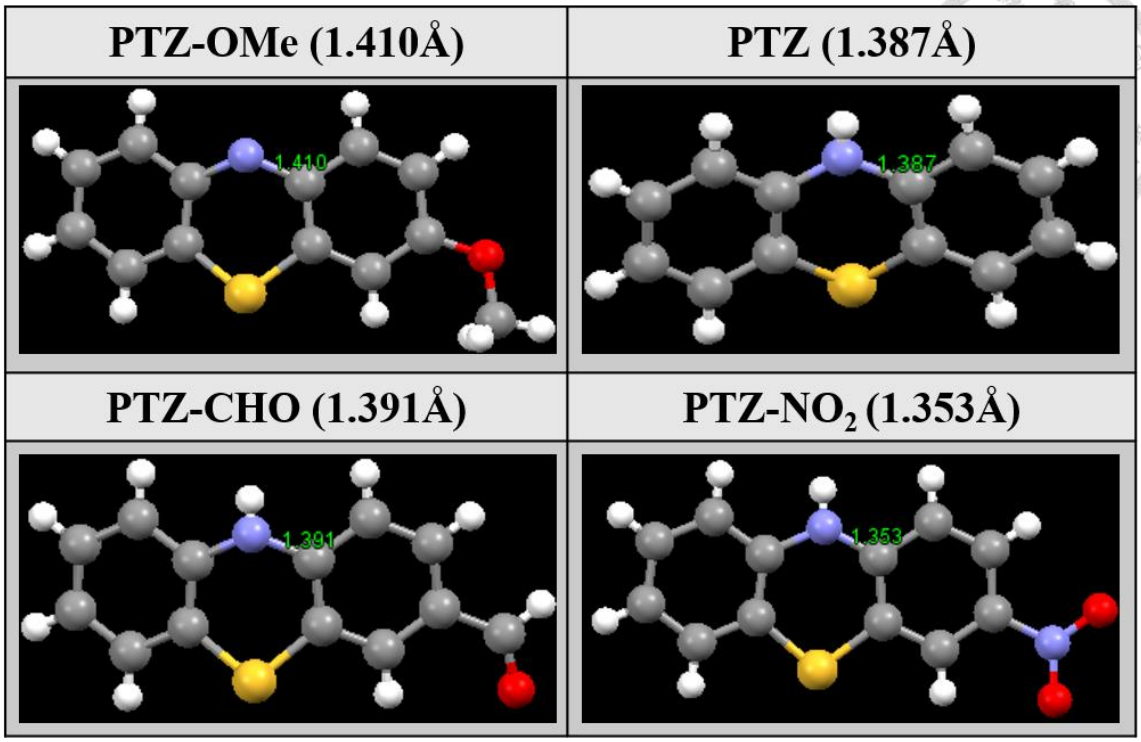

Figure 1- 6 Crystals and N-C distances in **PTZ-OMe**, **PTZ, PTZ-CHO** and **PTZ-NO$_2$**

With an aim to further confirm their properties, we tried to gain the single crystals of five target compounds. We gained and analyzed four single crystals **PTZ-OMe**, **PTZ**, **PTZ-CHO**, and **PTZ-NO$_2$** by XRD. Detailed and basic crystallographic data were collected in the Supporting information.

The crystals of both **PTZ-OMe** and **PTZ** belonged to monolithic array with a space group of P21/c, and however, the crystals of **PTZ-NO$_2$** as well as **PTZ-CHO** belonged to orthorhombic array with a space group of Pna21. **PTZ-NO$_2$** without clear structural categories were herringbone packing,[25] which implied that **PTZ-NO$_2$** existed strong π-π interactions between distinct layers in the crystal. It was worth noting that the strength of charge-transfer reflected on the distance between donor and acceptor. In other words, the shorter their distance was, the stronger the charge-transfer system was. The distances between nitrogen and substituted benzene in **PTZ-OMe**, **PTZ**, **PTZ-CHO** and **PTZ-NO$_2$** were 1.410, 1.387, 1.391 and 1.351 Å, supporting that the strength of charge-transfer

doi:10.6342/NTU202201631

system were **PTZ-OMe** < **PTZ** < **PTZ-CHO** < **PTZ-NO2**.

1.2.3 Photophysical Properties

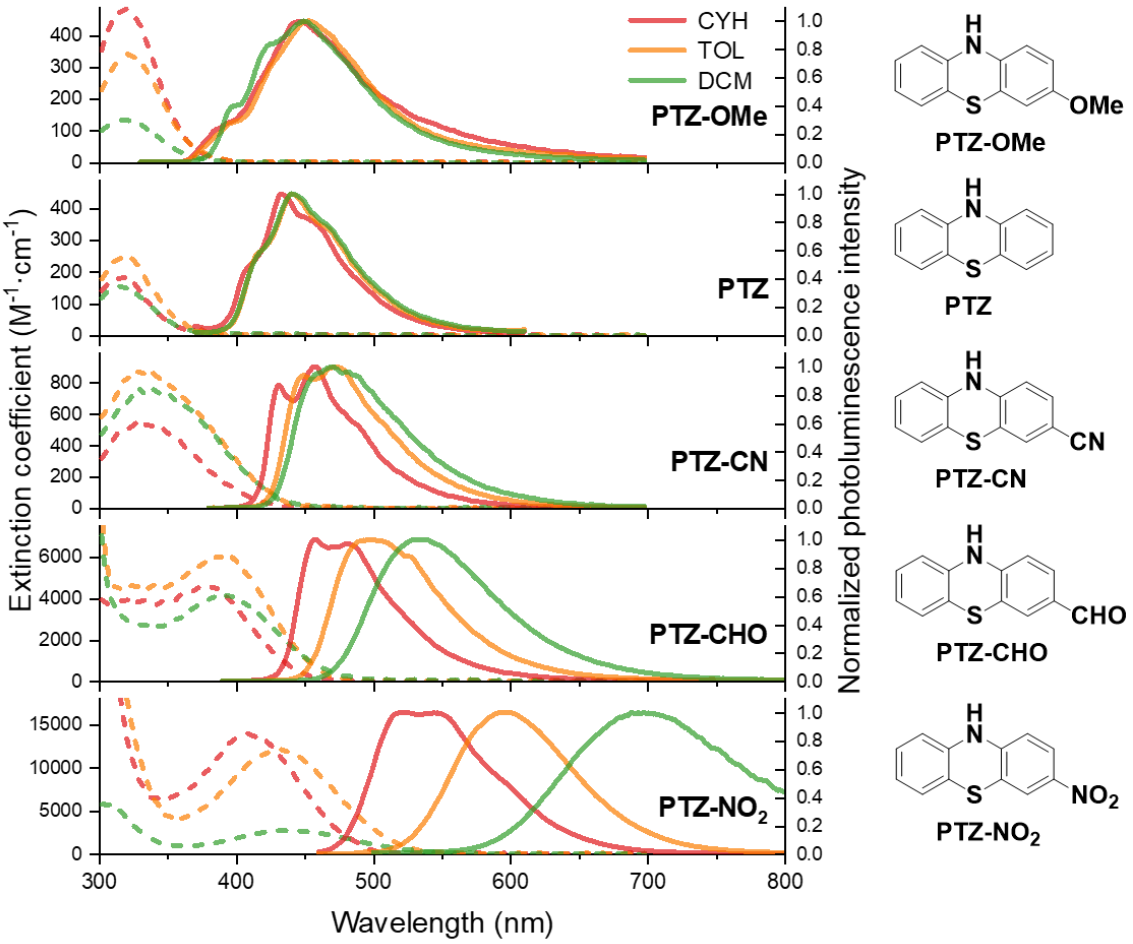

Figure 1- 7 Steady-state absorption spectra (dashed line), recorded as a function of the extinction coefficient, and photoluminescence spectra (solid line) of five compounds in various solvents at room temperature.

doi:10.6342/NTU202201631

Table 1- 2 Absorption and emission of five titled compounds

Abs / Em / QY	CYH	TOL	DCM
PTZ-OMe	314 / 448 / 0.29	322 / 453 / 0.42	317 / 449 / 0.56
PTZ	318 / 433 / 0.16	319 / 441 / 0.24	313 / 441 / 0.22
PTZ-CN	331 / 457 / 6.60	334 / 472 / 11.0	339 / 471 / 11.0
PTZ-CHO	376 / 458 / 44.0	390 / 498 / 46.0	388 / 531 / 41.0
PTZ-NO_2	408 / 522 / 100	430 / 595 / 29	440 / 697 / 0.54

Absorbance(nm) / Emission(nm) / Quantum Yield %

Figure 1-5 and Table 1-2 showed the absorptive spectrum as well as fluorescent spectrum of our five target compounds in three solvents: cyclohexane (CYH), toluene (TOL), and dichloromethane (DCM). The absorption as well as fluorescent spectrum in high polar solvent like ethanol or acetonitrile and detailed photophysical data were present in the Supporting information. As present in Figure 1-5, the absorption band of **PTZ-OMe** at 320 nm with the lower extinction coefficient (less than 10^3 $M^{-1}cm^{-1}$) could be assigned to a π-π* transition incorporating with a partially forbidden transition due to the nonbonding orbital of sulfur. Further, the fluorescent peak of **PTZ-OMe** did not shift with different polarities and present mirror-image emissive band with the absorptive band, which confirmed the locally excited emission (LE) with a vibronic profile. Similar properties could be found in **PTZ** with an absorption peak at 320 nm and a vibronic weak emissive maximum at 440 nm in all three solvents. In comparison, modified by an electron withdrawing group at 3-position in **PTZ**, **PTZ-CN** present a longer absorption wavelength at 340 nm (cf. **PTZ**). In the different solvent environments, the red-shifted emissive peaks of **PTZ-CN** were observed at 457, 472 and 471 nm in CYH, TOL, and DCM, respectively. This solvatochromism apparently suggested that the lowest excited state of **PTZ-CN** was characterized by a noticeable CT transition rather than the LE transition. This phenomenon was further affirmed by the modification of the formyl group

doi:10.6342/NTU202201631

and nitro group. For **PTZ-CHO**, the wavelength of the absorption was obviously increased with solvent polarity, which showed typical CT transition. Besides, the fluorescent peaks were measured at 458, 498, and 531 nm in CYH, TOL and DCM, respectively. More apparently, the emission band of **PTZ-NO_2** with the strongest electron-withdrawing NO_2 group was redshifted from 522 nm in CYH to as far as 697 nm in DCM, thereby showing the strongest excited-state CT transition among five target compounds. Hence, based on the degree of solvatochromism, the strength of the CT transition among five target compounds arranged in the order **PTZ-OMe** ≈ **PTZ** < **PTZ-CN** < **PTZ-CHO** < **PTZ-NO_2**, which be consistent well with electron withdrawing ability of these five substituents. The transformation from LE to CT transition correspond was in harmony with our frontier orbital prediction in the theoretical calculation**.** The photophysical data of our five target compounds were summarized in Table 1-2. **PTZ-OMe** and **PTZ** had poor emission (< 1%) due to their LE transition incorporated in nonbonding orbital of sulfur. **PTZ-CN**, **PTZ-CHO** and **PTZ-NO_2** exhibited tunable emission depending on their electron withdrawing strength. Nitro group was popularly considered as a fluorescent quencher, but, impressively, **PTZ-NO_2** had adequate emission from near 100% in CYH to 0.54% in DCM.in our cases. It was worthwhile to mention that the emissive wavelength of **PTZ-NO_2** reached to near infrared band as far as 700 nm in DCM, which might form other nonradiative relaxation for the quenching of the excited state. This quenching mechanism, called energy gap law, increased with decreasing energy gap, rendering lower fluorescent quantum yield in the high-polar solvents.[4d, 26]

doi:10.6342/NTU202201631

Table 1- 3 Photophysical data in cyclohexane

	Absorption (nm)	Emission (nm)	Stokes shift [cm^{-1}]	Quantum yield %	Lifetime[a] (ns)	$k_{radiative}$	$k_{nonradiative}$
PTZ-OMe	314	448	9526	0.29	0.38	$7.56x10^6$	$2.60x10^9$
PTZ	318	433	8352	0.16	0.74	$2.16x10^6$	$1.35x10^9$
PTZ-CN	331	457	8330	6.6	5.07	$1.31x10^7$	$1.84x10^8$
PTZ-CHO	376	458	4762	44	8.22	$5.30x10^7$	$6.87x10^7$
PTZ-NO_2	408	522	5353	100	7.63	$1.31x10^8$	-

[a] Lifetimes were measured by TCSPC with an excitation wavelength at 360 nm for all five compounds.

For the purposes of deeper research, the excited state dynamics were conducted by time-correlated single photon counting (TCSPC). The fluorescent dynamics for five target molecules in five different solvents (CYH, TOL, DCM, ACN and ethanol) were shown in the Supporting information. photophysical data in cyclohexane. In Table 1-3, k_r, k_{obs} , and k_{nr} denoted the radiative decay rate constant, the experimentally observed decay rate constant, and the nonradiative decay rate constant, respectively, where PLQY was defined as $k_r / k_{obs} = k_r / (k_r + k_{nr})$. Gathering k_{obs} derived experimentally PLQY, k_{nr} and k_r could be calculated and summarized in Table 1-3. The results, in a qualitative manner, suggested that an increase in the electron withdrawing ability of the substituent led to a decrease in k_{nr} and an increase in k_r. For instance, k_r for **PTZ** in CYH was deduced to be 2.16×10^6 s^{-1}, which was smaller over 60 times than that of **PTZ-NO_2** (1.31×10^8 s^{-1}). These results combined with the large k_{nr} for **PTZ** in CYH (1.35×10^9 s^{-1}) led to its relatively much lower emission compared with the electron withdrawing group-substituted **PTZ** molecules. Actually, k_r of **PTZ** (2.16×10^6 s^{-1}) belonged to a forbidden lowest-lying transition. Furthermore, in Table 1-3, increasing k_r following their electron withdrawing ability showed that their lowest-lying transition were more flexible Observing the tendency of k_r and k_{nr}, we could find that an increase energy of the forbidden n-π* character result from the less incorporation of the nonbonding orbitals of sulfur upon increasing the electron-withdrawing ability, and hence the forbidden n-π*

doi:10.6342/NTU202201631

transition was disconnected from the π-π* state. This deduction was also supported by the increasing extinction coefficient from electron donating group-substituted **PTZ** (e.g., OMe, ca. 500 $M^{-1}cm^{-1}$ at the peak in CYH) to the Electron withdrawing group-substituted **PTZ** derivatives (e.g., NO_2, > 10^4 $M^{-1}cm^{-1}$ at the peak in CYH, TOL and DCM; Figure 1-7). On the other hand, decreasing k_{nr} might echo planarization of the **PTZ** moiety with increasing CT transition. Support for these deductions were analyzed in the ground and excited state geometry optimization of theoretical calculation.

doi:10.6342/NTU202201631

1.2.4 Cyclic Voltammetry Analysis

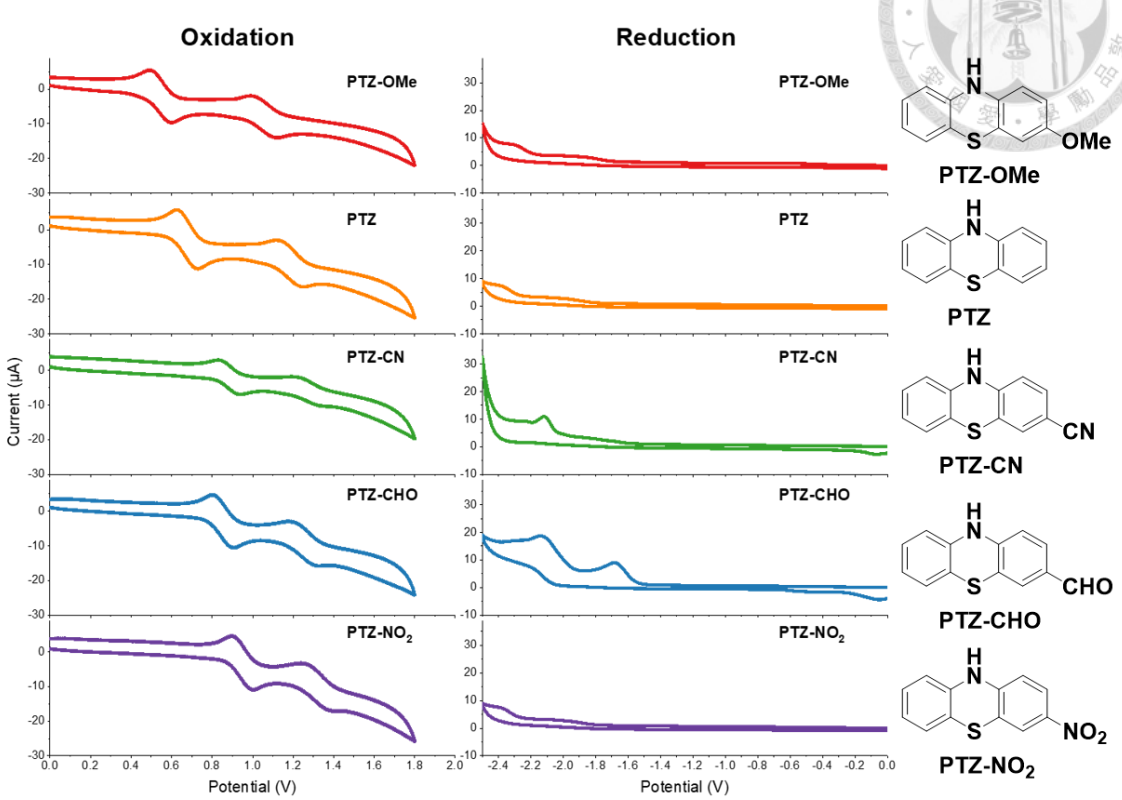

Figure 1- 8 Cyclic voltammograms of five titled molecules. Reduction curves of **PTZ** derivatives were irreversible since they were easily oxidized.

Table 1- 4 Electrochemical properties

	E_{ox}^{D} (V)	E_{re}^{A} (V)	HOMO (eV)	LUMO (eV)
PTZ-OMe	0.54	-2.12	-4.80	-2.08
PTZ	0.68	-2.02	-4.94	-2.18
PTZ-CN	0.89	-1.72	-5.14	-2.48
PTZ-CHO	0.86	-1.68	-5.12	-2.52
PTZ-NO_2	0.95	-0.86	-5.16	-3.34

E_{ox}^{D} $and E_{re}^{A}$ are anodic and cathodic peak , potential using Fc+/Fc as reference
HOMO = - (4.80 + E_{ox}^{D} - E_{ox}^{Fc}), LUMO = - (4.80 + E_{re}^{A} - E_{re}^{Fc})

The intrinsic electronic properties of five target compounds were measured by cyclic voltammetry (CV) analysis in Figure 1-8 and detailed value in Table 1-4 In the CV

doi:10.6342/NTU202201631

experiment, the reference electrode was the Ag/Ag+ (0.01M $AgNO_3$) electrode. A platinum electrode and a glassy carbon electrode were chosen as the working electrode for measuring the oxidation and reduction potentials, respectively. Pure platinum wire was also used as counter electrode. All CV measurements were conducted in 0.1M $^nBu_4PF_6$ solution as electrolyte. At last, we used the ferrocenium/ferrocene (Fc+/Fc) couple as our refence potential. As shown in Table 1-4 and Figure 1-8, the HOMOs of five target compounds decreased to the more negative side in the order **PTZ-OMe** (-4.80 eV) > **PTZ** (-4.94 eV) > **PTZ-CN** (-5.14 eV) & **PTZ-CHO** (-5.12 eV) > **PTZ-NO$_2$** (-5.16 eV), which matched the overall trend of electron-donor capability (Electron donating group > parent **PTZ** > Electron withdrawing group). Besides, energy levels of the LUMOs of five target compounds, which were calculated by the energy gap of the photoluminescence onset to the HOMO in the absorption band, decreased in the order: **PTZ-OMe** (-2.08 eV) > **PTZ** (-2.18 eV) > **PTZ-CHO** (-2.48 eV) > **PTZ-CN** (-2.52 eV) > **PTZ-NO$_2$** (-3.34 eV), which was consistent well with energy level of HOMO and electron-donating capability. However, the energy levels of the LUMOs of five target compounds, which varied from -2.08 eV for **PTZ-OMe** to -3.34 eV for **PTZ-NO$_2$**, changed more significant than that of the HOMOs of five target compounds, which was also important clue in our deduction in excited state mixing of **PTZ** and **PTZ-OMe**.

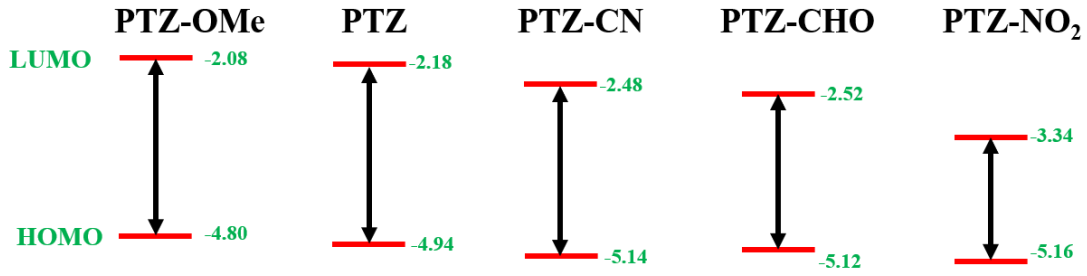

Figure 1- 9 HOMO/LUMO of five compounds in cyclic voltammetry

doi:10.6342/NTU202201631

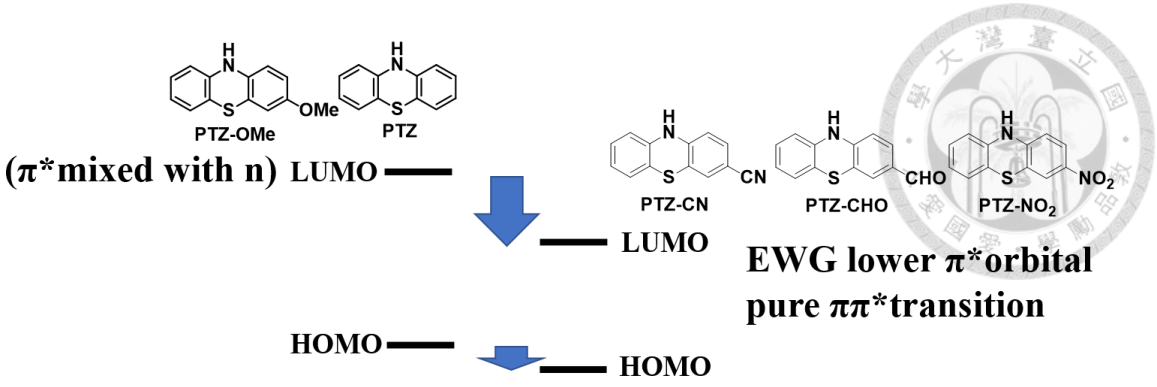

Figure 1- 10 Mechanism of five compounds

According to aforementioned data including theoretical calculation, photophysical spectrum and electrochemical analysis, we could derive the whole mechanism in Figure 1-9. The LUMO of **PTZ-OMe** and **PTZ** belonged to π* orbital mixed with nonbonding orbital, which decreased their fluorescence. In contrast, the EWGs could lower much more energy of LUMO than those of HOMO, so nonbonding orbital would not incorporate in the transition, which facilitates their radiative pathway. This was why the "dark" **PTZ** could enhance the fluorescent emission after coupling the EWGs, especially for the "dark" group, nitro.

doi:10.6342/NTU202201631

1.3 Conclusion

With an aim to enhanced fluorescent intensity of phenothiazine, a series of PTZ analogues have been well-designed, synthesized carefully, and systematically analyzed

Parent **PTZ** and electron-donating-substituted **PTZ-OMe** were found their weak fluorescent emission due to partial forbidden transitions from involvement of nonbonding orbital of sulfur atom. Moreover, in theoretical calculation, the twisting motion in the excited state of **PTZ** and **PTZ-OMe** increased nonradiative pathway. By contrast, electron-withdrawing substituted **PTZ-CN**, **PTZ-CHO** and **PTZ-NO_2** possessed enhanced fluorescent emission. electron-withdrawing groups could efficiently reduce the nonbonding orbitals of sulfur, which facilitated the radiative relaxation of three compounds. Furthermore, in the theoretical calculation of **PTZ-CN**, **PTZ-CHO** and **PTZ-NO_2**, electron-withdrawing group inducing CT transition prevent the twisting motion and nonradiative relaxation from lowering their fluorescent emission. Among all of three electron-withdrawing substituted compounds **PTZ-CN**, **PTZ-CHO** and **PTZ-NO_2**, **PTZ-NO_2** displayed 100% fluorescent quantum yield in the cyclohexane and obvious solvatochromism from 500nm to 700nm in cyclohexane, toluene and dichloromethane., which totally broke the conception nitro group was a strong fluorescent quencher.

doi:10.6342/NTU202201631

1.4 Reference

[1] a) Z.-S. Huang, H. Meier, D. Cao, *J. Mater. Chem. C* **2016**, *4*, 2404-2426; b) H. Tian, X. Yang, R. Chen, Y. Pan, L. Li, A. Hagfeldt, L. Sun, *Chem. Commun.* **2007**, 3741-3743; c) G. D. Blanco, A. J. Hiltunen, G. N. Lim, C. B. Kc, K. M. Kaunisto, T. K. Vuorinen, V. N. Nesterov, H. J. Lemmetyinen, F. D'Souza, *ACS Appl. Mater. Interfaces* **2016**, *8*, 8481-8490; d) J. V. Vaghasiya, K. K. Sonigara, J. Prasad, T. Beuvier, A. Gibaud, S. S. Soni, *J. Mater. Chem. A* **2017**, *5*, 5373-5382.

[2] a) M. Okazaki, Y. Takeda, P. Data, P. Pander, H. Higginbotham, A. P. Monkman, S. Minakata, *Chem. Sci.* **2017**, *8*, 2677-2686; b) H. Tanaka, K. Shizu, H. Nakanotani, C. Adachi, *J. Phys. Chem. C* **2014**, *118*, 15985-15994; c) I. Marghad, F. Bencheikh, C. Wang, S. Manolikakes, A. Rérat, C. Gosmini, D. hyeon Kim, J.-C. Ribierre, C. Adachi, *RSC Adv.* **2019**, *9*, 4336-4343; d) D.-G. Chen, T.-C. Lin, Y.-A. Chen, Y.-H. Chen, T.-C. Lin, Y.-T. Chen, P.-T. Chou, *J. Phys. Chem. C* **2018**, *122*, 12215-12221; e) O. Bezvikonnyi, D. Gudeika, D. Volyniuk, V. Mimaite, B. R. Sebastine, J. V. Grazulevicius, *J. Lumin.* **2019**, *206*, 250-259.; f) R. S. Nobuyasu, Z. Ren, G. C. Griffiths, A. S. Batsanov, P. Data, S. Yan, A. P. Monkman, M. R. Bryce, F. B. Dias, *Adv. Opt. Mater.* **2016**, *4*, 597-607

[3] a) J. Burn, SAGE Publications, **1954**; b) J. P. Swazey, *Chlorpromazine in psychiatry: a study of therapeutic innovation*, The MIT Press, **1974**; c) V. V. Coşofreţ, R. P. Buck, *Analyst* **1984**, *109*, 1321-1325; d) C.-H. Wu, L.-Y. Bai, M.-H. Tsai, P.-C. Chu, C.-F. Chiu, M. Y. Chen, S.-J. Chiu, J.-H. Chiang, J.-R. Weng, *Sci. Rep.* **2016**, *6*, 1-11.

[4] a) Z. Zhou, C. E. Hauke, B. Song, X. Li, P. J. Stang, T. R. Cook, *J. Am. Chem. Soc.* **2019**, *141*, 3717-3722.; b) Y. Satoh, L. Catti, M. Akita, M. Yoshizawa, *J. Am. Chem. Soc.* **2019**, *141*, 12268-12273

doi:10.6342/NTU202201631

[5] a) J. K. Salunke, F. Wong, K. Feron, S. Manzhos, M. F. Lo, D. Shinde, A. Patil, C. Lee, V. Roy, P. Sonar, *J. Mater. Chem. C* **2016**, *4*, 1009-1018; b) G. B. Bodedla, K. J. Thomas, S. Kumar, J.-H. Jou, C.-J. Li, *RSC Adv.* **2015**, *5*, 87416-87428; c) A. Bejan, S. Shova, M.-D. Damaceanu, B. C. Simionescu, L. Marin, *Crystal Growth & Design* **2016**, *16*, 3716-3730.; d) X.-C. Zeng, J.-Y. Wang, L.-J. Xu, H.-M. Wen, Z.-N. Chen, *J. Mater. Chem. C* **2016**, *4*, 6096-6103

[6] Y. Im, M. Kim, Y. J. Cho, J.-A. Seo, K. S. Yook, J. Y. Lee, *Chem. Mater.* **2017**, *29*, 1946-1963.

[7] a) K. Upadhyay, A. Asthana, R. K. Tamrakar, *Res. Chem. Intermed.* **2015**, *41*, 7481-7495; b) T. Rodrigues, C. G. d. Santos, A. Riposati, L. R. Barbosa, P. Di Mascio, R. Itri, M. S. Baptista, O. R. Nascimento, I. L. Nantes, *The Journal of Physical Chemistry B* **2006**, *110*, 12257-12265

[8] M. Saucin, A. Van de Vorst, *Radiat. Environ. Biophys.* **1980**, *17*, 159-168.

[9] J. R. Huber, W. Mantulin, *J. Am. Chem. Soc.* **1972**, *94*, 3755-3760.

[10] M. Hosseinnezhad, K. Gharanjig, S. Moradian, S. Tafaghodi, *Arabian J. Chem.* **2019**, *12*, 2069-2076.

[11] K. Pothula, L. Tang, Z. Zha, Z. Wang, *RSC Adv.* **2015**, *5*, 83144-83148.

[12] V. Thottempudi, H. Gao, J. n. M. Shreeve, *J. Am. Chem. Soc.* **2011**, *133*, 6464-6471.

[13] a) R. Rai, M. Rajput, M. Agrawal, S. Agrawal, *Journal of Scientific Research* **2011**, *55*, 1; b) K. Nepali, H.-Y. Lee, J.-P. Liou, *J. Med. Chem.* **2018**, *62*, 2851-2893

[14] a) L. Keyser, S. Levine, F. Kaufman, *J. Chem. Phys.* **1971**, *54*, 355-363.; b) V. Donnelly, D. Keil, F. Kaufman, *J. Chem. Phys.* **1979**, *71*, 659-673

[15] a) J. P. Zobel, J. J. Nogueira, L. González, *Chem. Eur. J.* **2018**, *24*, 5379-5387.;

doi:10.6342/NTU202201631

b) R. Hurley, A. Testa, *J. Am. Chem. Soc.* **1966**, *88*, 4330-4332; c) B. Valeur, *Digital Encyclopedia of Applied Physics* **2003**, 477-531

[16] a) H.-C. Huang, K.-L. Wang, S.-T. Huang, H.-Y. Lin, C.-M. Lin, *Biosens. Bioelectron.* **2011**, *26*, 3511-3516.; b) S. K. Panja, N. Dwivedi, S. Saha, *RSC Adv.* **2016**, *6*, 105786-105794

[17] O. S. Khalil, H. Bach, S. McGlynn, *J. Mol. Spectrosc.* **1970**, *35*, 455-460.

[18] J. V. Caspar, T. J. Meyer, *The Journal of Physical Chemistry* **1983**, *87*, 952-957.

[19] K. Skonieczny, I. Papadopoulos, D. Thiel, K. Gutkowski, P. Haines, P. M. McCosker, A. D. Laurent, P. A. Keller, T. Clark, D. Jacquemin, *Angew. Chem. Int. Ed.* **2020**, *59*, 16104-16113.

[20] M. Kuss-Petermann, O. S. Wenger, *J. Am. Chem. Soc.* **2016**, *138*, 1349-1358.

[21] J. S. Ward, R. S. Nobuyasu, A. S. Batsanov, P. Data, A. P. Monkman, F. B. Dias, M. R. Bryce, *Chem. Commun.* **2016**, *52*, 2612-2615.

[22] S. Kumar, M. Singh, J.-H. Jou, S. Ghosh, *J. Mater. Chem. C* **2016**, *4*, 6769-6777.

[23] B. V. Rokade, K. R. Prabhu, *J. Org. Chem.* **2012**, *77*, 5364-5370.

[24] H. J. Shine, J. J. Silber, R. J. Bussey, T. Okuyama, *J. Org. Chem.* **1972**, *37*, 2691-2697.

[25] L. Jensen, in *Journal of Polymer Science Part C: Polymer Symposia, Vol. 29*, Wiley Online Library, **1970**, pp. 47-63.

[26] a) S. Yang, J. Liu, P. Zhou, G. He, *The Journal of Physical Chemistry B* **2011**, *115*, 10692-10698; b) S. D. Cummings, R. Eisenberg, *J. Am. Chem. Soc.* **1996**, *118*, 1949-1960.; c) Y. Kawanishi, N. Kitamura, S. Tazuke, *The Journal of Physical Chemistry* **1986**, *90*, 2469-2475

doi:10.6342/NTU202201631

doi:10.6342/NTU202201631

1.5 Supporting Information

1.5.1 Photophysical Results

Absorption and Emission in high polar solvents

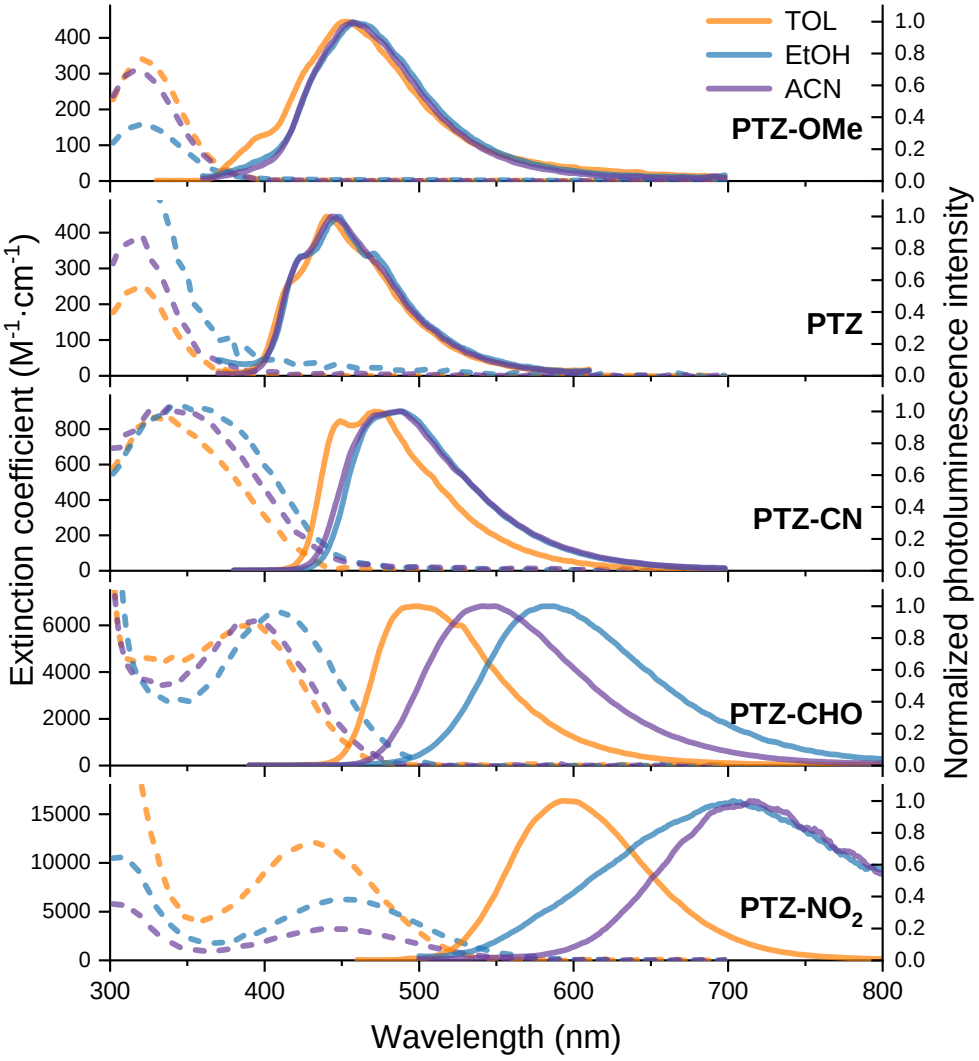

Figure S1-1. Steady-state absorption spectra in extinction coefficient (M^{-1} cm^{-1}) (dashed line) as well as photoluminescence (solid line) spectra of five titled molecules. Notes that orange, blue, and purple lines represent toluene (TOL), ethanol (EtOH), and acetonitrile (ACN), respectively.

doi:10.6342/NTU202201631

Experimental Stokes shift

Table S1-1. Stokes shifts calculated from the experimental peak wavelengths of absorbance and photoluminescence spectra of five titled molecules in five different solvents. [a]

Abs./PL (nm) Stokes shift (cm^{-1})	CYH [a]	TOL [a]	DCM [a]	EtOH [a]	ACN [a]
PTZ-OMe	314, 448 9526	322, 453 8981	317, 449 9274	318, 459 9660	317, 457 9664
PTZ	318, 433 8352	319, 441 8672	313, 441 9273	318, 448 9125	319, 445 8876
PTZ-CN	331, 457 8330	334, 472 8754	339, 471 8267	346, 489 8452	341, 487 8792
PTZ-CHO	376, 458 4762	390, 498 5561	388, 531 6941	409, 587 7414	394, 549 7166
PTZ-NO_2	408, 522 5353	430, 595 6449	440, 697 8380	449, 712 8227	444, 711 8458

[a] CYH = cyclohexane, TOL = toluene, DCM = dichloromethane (DCM), EtOH = ethanal (EtOH), and ACN = acetonitrile.

doi:10.6342/NTU202201631

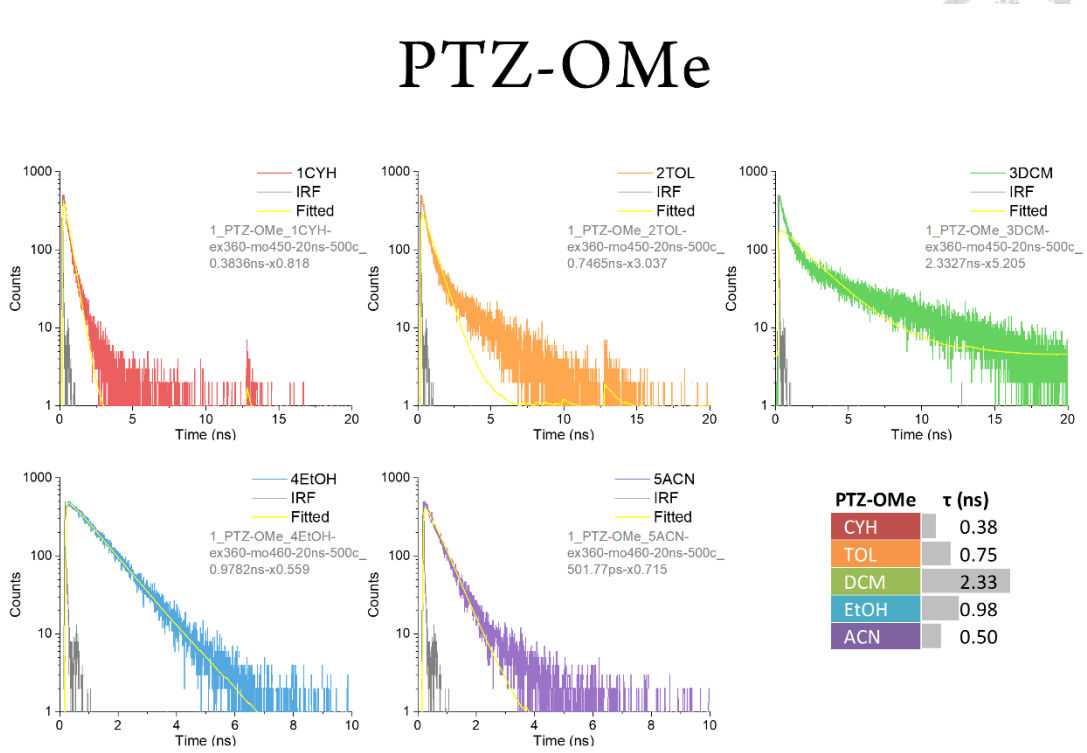

Figure S1-2. Fluorescence decay spectrum of **PTZ-OMe** in five different solvents.

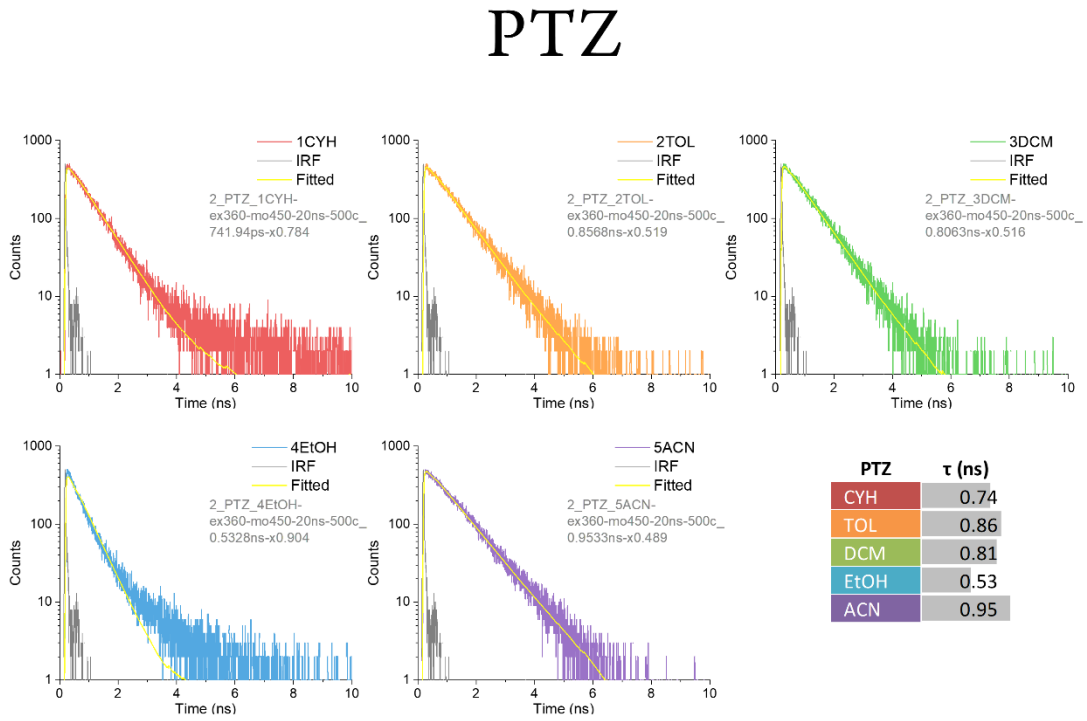

Figure S1-3. Fluorescence decay spectrum of **PTZ** in five different solvents.

doi:10.6342/NTU202201631

PTZ-CN

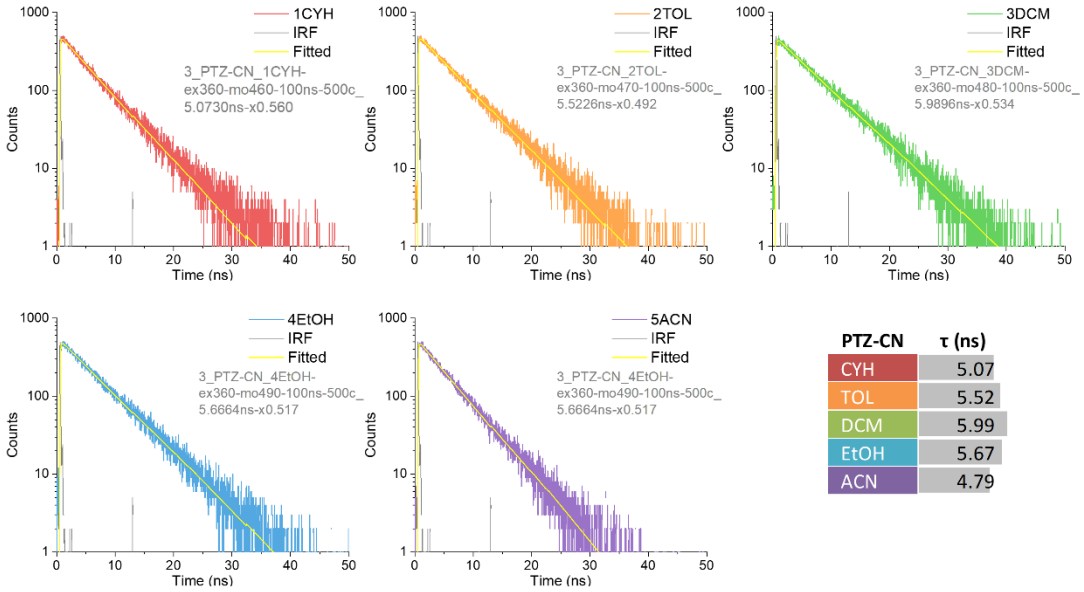

PTZ-CN	τ (ns)
CYH	5.07
TOL	5.52
DCM	5.99
EtOH	5.67
ACN	4.79

Figure S1-4. Fluorescence decay spectrum of **PTZ-CN** in five different solvents.

PTZ-CHO

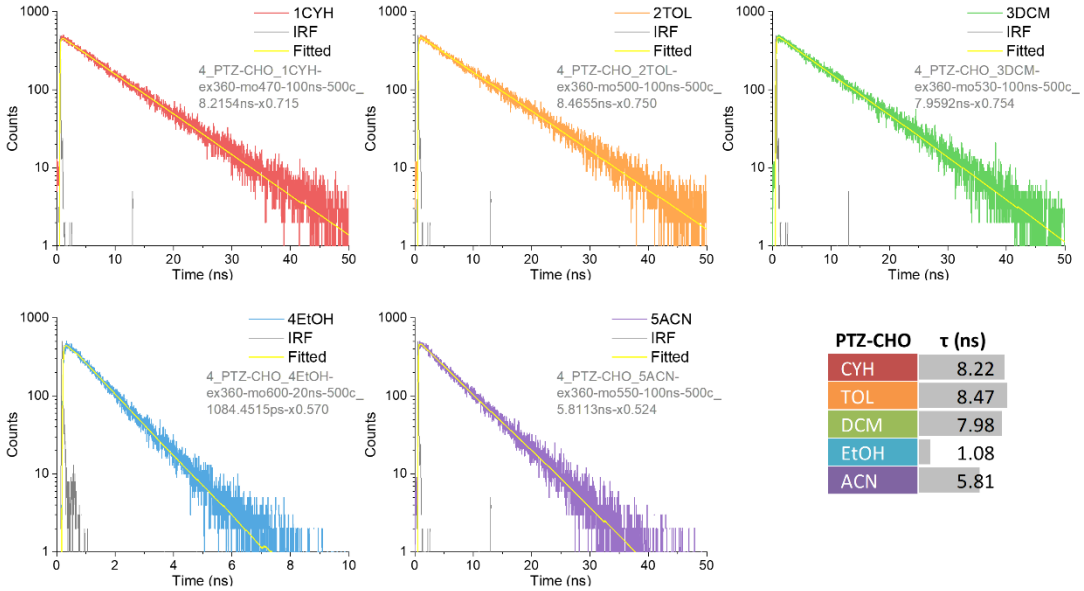

PTZ-CHO	τ (ns)
CYH	8.22
TOL	8.47
DCM	7.98
EtOH	1.08
ACN	5.81

Figure S1-5. Fluorescence decay spectrum of **PTZ-CHO** in five different solvents.

doi:10.6342/NTU202201631

PTZ-NO_2

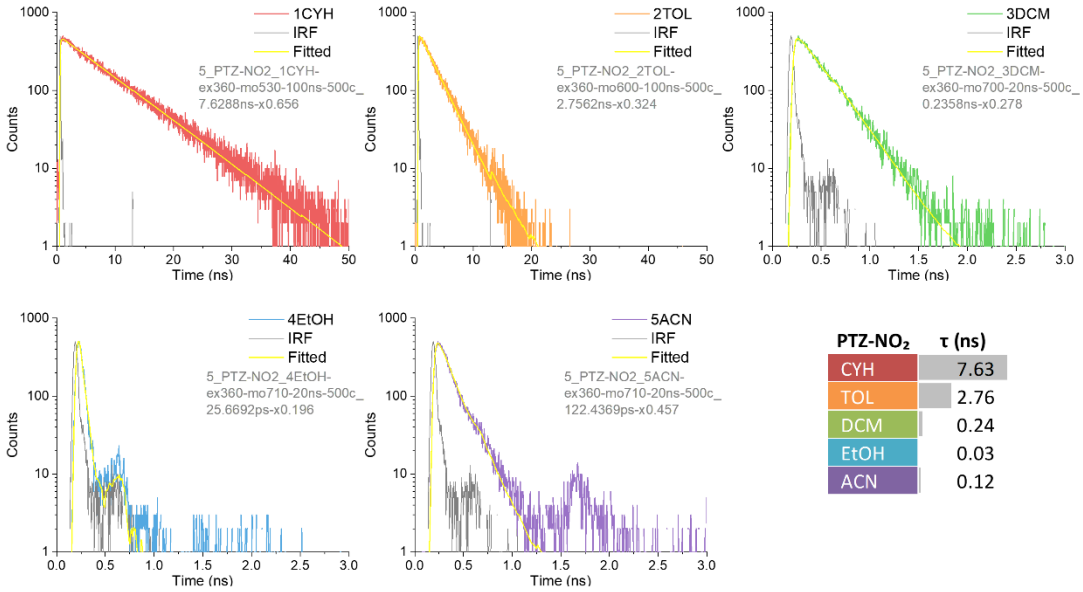

Figure S1-6. Fluorescence decay spectrum of **PTZ-NO_2** in five different solvents

doi:10.6342/NTU202201631

Table S1-2. Excitation, monitoring wavelength as well as quantum yields, lifetimes, and rate constants of the titled molecules.

Compound	Solvent [a]	Ex./Mon. [b] (nm)	Q.Y.[c] (%)	Lifetime [d] (ns)	$k_r\ (s^{-1})$ [e]	$k_{nr}\ (s^{-1})$ [f]
PTZ-OMe	CYH	320 / 450	0.29	0.38	7.56×10^6	2.60×10^9
	TOL	320 / 450	0.42	0.75	5.63×10^6	1.33×10^9
	DCM	320 / 450	0.56	2.33	2.40×10^6	4.26×10^8
	EtOH	320 / 460	0.26	0.98	2.66×10^6	1.02×10^9
	ACN	320 / 460	0.27	0.50	5.38×10^6	1.99×10^9
PTZ	CYH	320 / 450	0.16	0.74	5.63×10^6	1.33×10^9
	TOL	320 / 450	0.24	0.86	2.40×10^6	4.26×10^8
	DCM	320 / 450	0.22	0.81	2.66×10^6	1.02×10^9
	EtOH	320 / 450	0.51	0.53	5.38×10^6	1.99×10^9
	ACN	320 / 450	0.48	0.95	2.16×10^6	1.35×10^9
PTZ-CN	CYH	320 / 460	6.64	5.07	2.40×10^6	4.26×10^8
	TOL	320 / 470	11.78	5.52	2.66×10^6	1.02×10^9
	DCM	320 / 480	10.86	5.99	5.38×10^6	1.99×10^9
	EtOH	320 / 490	14.97	5.67	2.16×10^6	1.35×10^9
	ACN	320 / 490	11.64	4.79	2.80×10^6	1.16×10^9
PTZ-CHO	CYH	380 / 470	43.52	8.22	2.66×10^6	1.02×10^9
	TOL	380 / 500	46.14	8.47	5.38×10^6	1.99×10^9
	DCM	380 / 530	40.96	7.98	2.16×10^6	1.35×10^9
	EtOH	380 / 600	6.48	1.08	2.80×10^6	1.16×10^9
	ACN	380 / 550	35.42	5.81	2.73×10^6	1.24×10^9

doi:10.6342/NTU202201631

	CYH	430 / 530	100	7.63	5.38×10^6	1.99×10^9
	TOL	430 / 600	29.08	2.76	2.16×10^6	1.35×10^9
PTZ-NO₂	DCM	430 / 700	0.54	0.24	2.80×10^6	1.16×10^9
	EtOH	430 / 710	0.14	0.03	2.73×10^6	1.24×10^9
	ACN	430 / 710	0.35	0.12	9.57×10^6	1.87×10^9

[a] CYH = cyclohexane, TOL = toluene, DCM = dichloromethane, EtOH = ethanol, and ACN = acetonitrile. [b] Ex. was the excitation wavelength for measuring quantum yield. Mon. was the monitoring wavelength when measuring lifetime. [c] Q.Y. was the quantum yield measured comparatively with POPOP, C480, and DCM as standard dye. [d] Lifetime were measured with TCSPC and excited at 360 nm for all five compounds. [e] k_r was radiative decay rate constant. [f] k_{nr} was non-radiative decay rate constant.

1.5.2 Computational Approach

The density functional theory method (DFT) were applied in the optimization of geometries of the ground-state for five target molecules. Time-dependent density functional theory method (TD-DFT) were applied in the electronically excited-state structures with relevant photophysical properties by m062x and b3lyp hybrid function in combination with a polarizable continuum model (PCM) in cyclohexane, and 6-31+G(d,p) basis set for all atoms. The absorbance and emission wavelength from m062x method showed less deviation from experimental data. All theoretical calculations were performed using the Gaussian 09 program. Detail of the supplementary were elaborated below.

doi:10.6342/NTU202201631

Table S1-3. Calculated wavelength (λ), oscillator strength (f) and orbital transition for five titled molecules with m062x.

Molecule	Absorption Energy gap, O.S., and transition		Fluorescence Energy gap, O.S., and transition		
PTZ-OMe	4.11 eV, 301.7 nm. f = 0.0041		3.01 eV, 412.32 nm. f = 0.0061		
	HOMO → LUMO	18.81%	HOMO	← LUMO	95.97%
	HOMO → LUMO+1	68.03%			
	HOMO → LUMO+2	3.25%			
PTZ	4.09 eV, 302.92 nm. f = 0.0007		2.95 eV, 420.15 nm. f = 0.008		
	HOMO → LUMO	91.99%	HOMO	← LUMO	97.44%
PTZ-CN	3.84 eV, 323.28 nm. f = 0.0741		2.80 eV, 443.01 nm. f = 0.0559		
	HOMO → LUMO	84.90%	HOMO	← LUMO	94.82%
	HOMO → LUMO+1	4.41%			
	HOMO → LUMO+2	2.00%			
PTZ-CHO	3.64 eV, 340.2 nm. f = 0.1248		2.68 eV, 462.76 nm. f = 0.1067		
	HOMO → LUMO	83.44%	HOMO	← LUMO	92.05%
	HOMO → LUMO+2	2.95%	HOMO	← LUMO+3	2.52%
	HOMO → LUMO+4	3.35%			
	HOMO-4 → LUMO	4.13%			
PTZ-NO_2	3.43 eV, 361.92 nm. f = 0.1873		2.50 eV, 496.11 nm. f = 0.1694		
	HOMO → LUMO	89.26%	HOMO	← LUMO	92.38%
	HOMO → LUMO+2	2.99%	HOMO	← LUMO+2	2.86%
	HOMO → LUMO+4	2.83%			

doi:10.6342/NTU202201631

Table S1-4. Calculated wavelength (λ), oscillator strength (f) and orbital transition for five titled molecules with b3lyp.

Molecule	Absorption Energy gap, O.S., and transition		Fluorescence Energy gap, O.S., and transition		
PTZ-OMe	3.6428 eV, 340.36 nm. f = 0.0012		2.6956 eV, 459.96 nm. f = 0.0058		
	HOMO → LUMO	58.03%	HOMO	← LUMO	98.19%
	HOMO → LUMO+1	38.77%			
PTZ	3.6452 eV, 340.13 nm. f = 0.0014		2.7474 eV, 451.28 nm. f = 0.0042		
	HOMO → LUMO	98.02%	LUMO → HOMO		99.22%
PTZ-CN	3.3094 eV, 374.64 nm. f = 0.0879		2.5272 eV, 490.6 nm. f = 0.0636		
	HOMO → LUMO	94.11%	HOMO	← LUMO	97.48%
	HOMO → LUMO+1	2.20%			
PTZ-CHO	3.001 eV, 413.14 nm. f = 0.1292		2.3138 eV, 535.84 nm. f = 0.1004		
	HOMO → LUMO	95.96%	HOMO	← LUMO	97.43%
PTZ-NO_2	2.5222 eV, 491.58 nm. f = 0.1675		1.8999 eV, 652.57 nm. f = 0.1407		
	HOMO → LUMO	97.76%	HOMO	← LUMO	98.36%

doi:10.6342/NTU202201631

1.5.3 Synthetic Procedure

All reagents were commercially available from Acros, Sigma Aldrich and Merck, which were used as supplied without further purification. Deuterated solvents were purchased from Cambridge Isotope Laboratory (Andover, MA). Column chromatography was carried out using silica gel from Merck (230-400 mesh). ^{1}H NMR, ^{13}C NMR spectra were recorded on a Varian Inova 400 MHz spectrometer. ^{1}H and ^{13}C NMR chemical shifts were reported relative to residual solvent signals. Mass spectra were recorded on a micrOTOF-Q 228888.10 183 mass spectrometer using electrospray ionization with Bruker microTOF-Q II. The cyclic voltammetry data were measured by CH Instruments CHI 1405.

doi:10.6342/NTU202201631

1.5.3.1 Synthesis of **PTZ-NO_2**

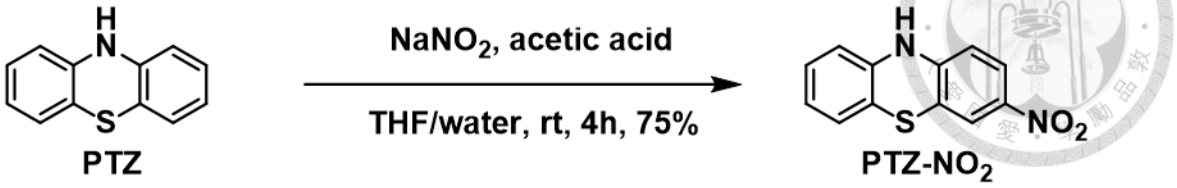

To the solution of phenothiazine (1 g, 5.02 mmole, 1 equiv.) in the THF (5 ml) and acetic acid (1.5 ml) in the ice bath was added a concentrated solution of sodium nitrite (1.08 g, 15.06 mmole, 3 equiv.) in water (2 ml) dropwise and stirred in the room temperature overnight. After completion of reaction, the reactant was extracted by ethyl acetate and brine. The organic layer was separated, dried over $MgSO_4$ and concentrated by rotavapor. The crude product could be purified by silica column (ethyl acetate: hexane = 1: 3 with 1% TEA, R_f = 0.37). The pure product **PTZ-NO_2** was black powder (3.75 mmole, 0.915 g, 75 %) m.p. = 182°C, FT-IR (cm^{-1}): 3475, 3318, 1567, 1537, 1326, 734. ^{1}H NMR (400 MHz, DMSO) δ 9.51 (s, 1H), 7.85 (d, J = 11.4 Hz, 1H), 7.73 (s, 1H), 7.02 (t, J = 7.6 Hz, 1H), 6.93 (d, J = 7.7 Hz, 1H), 6.84 (t, J = 8.0 Hz, 1H), 6.69 (d, J = 8.9 Hz, 2H). ^{13}C NMR (101 MHz, DMSO) δ 147.8, 141.0, 138.8, 128.2, 126.3, 124.7, 123.7, 121.6, 117.0, 115.4, 115.3, 113.4. HRMS (ESI-TOF) m/z: $[M+H]^+$ Calc'd for $C_{12}H_8N_2O_2S$ [245.0306]; Found 245.0306.

doi:10.6342/NTU202201631

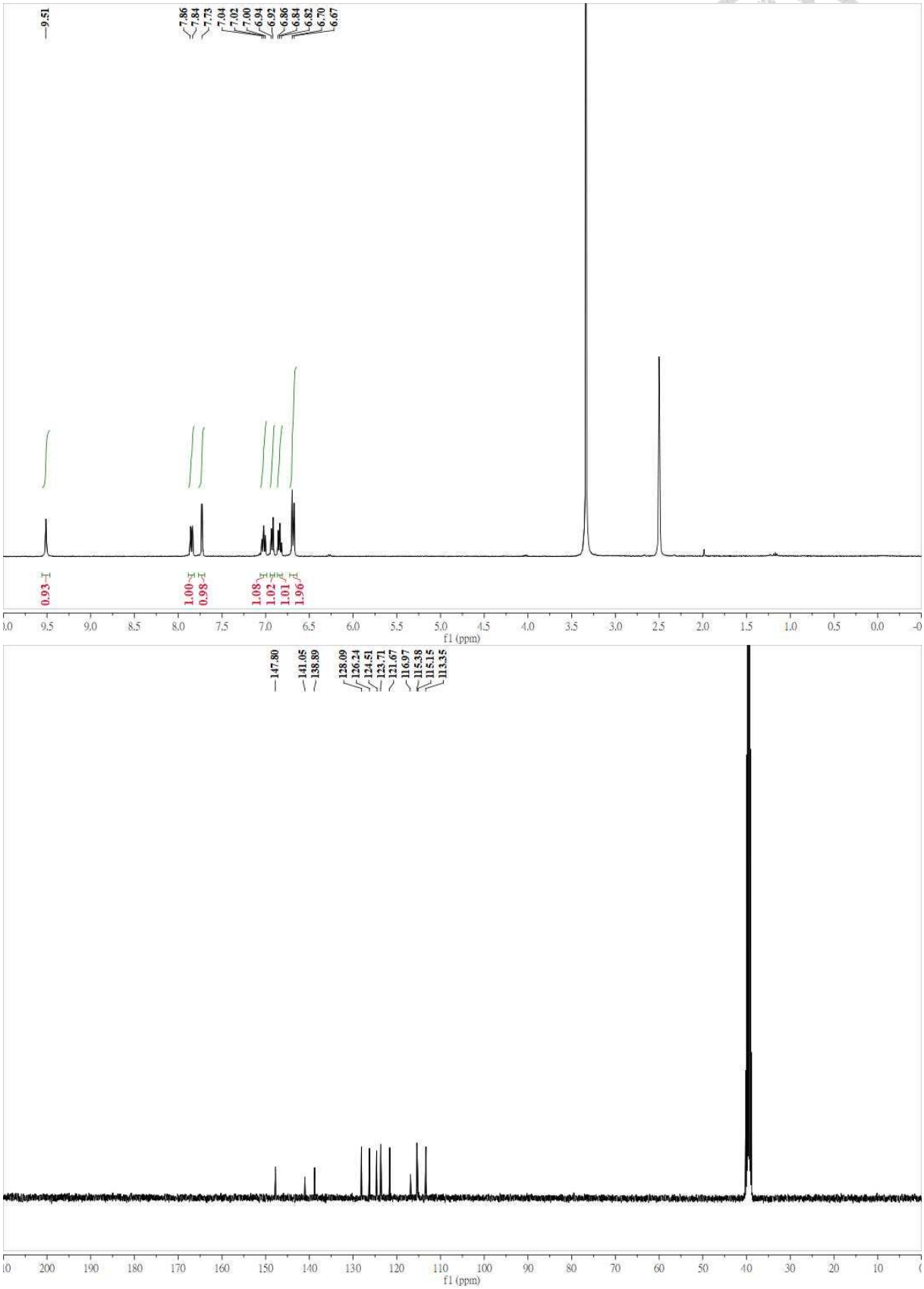

Figure S1-7. ^{1}H &^{13}C NMR of **PTZ-NO_2**.

doi:10.6342/NTU202201631

1.5.3.2 Synthesis of **PTZ-CHO**

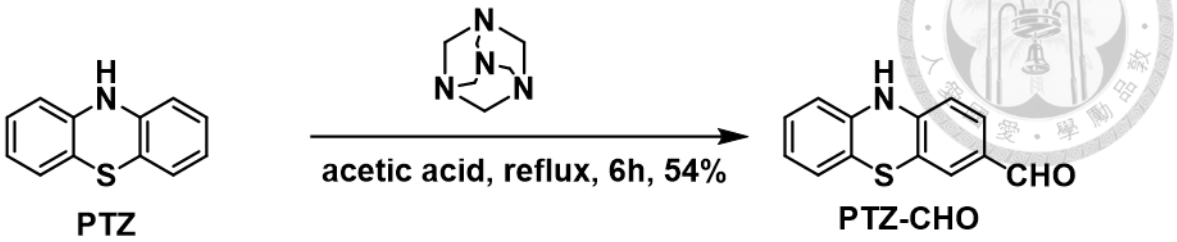

To the solution of phenothiazine (1 g, 5.02 mmole, 1 equiv.) and 1, 3, 5, 7-Tetraazatricyclo [3.3.1.13,7] decane (0.774 g, 5.52 mmole, 1.1 equiv.) in the acetic acid (10 ml) was refluxed overnight. After completion of reaction, the reactant was cooled to room temperature and then poured in the saturated sodium bicarbonate in the ice bath. After that, the reactant was extracted with ethyl acetate and brine. The organic layer was separated, dried over $MgSO_4$ and concentrated by rotavapor. The crude product could be purified by silica column (ethyl acetate: hexane = 1:4 with 1% TEA, R_f = 0.43). The pure product **PTZ-CHO** was light yellow powder (2.71 mmole, 0.615 g, 54.3%). m.p. = 176°C, FT-IR (cm^{-1}): 3339, 2838,2749, 1659, 1556, 1469, 1199, 805. ^{1}H NMR (400 MHz, DMSO) δ 9.64 (s, 1H), 9.25 (s, 1H), 7.49 (d, *J* = 8.1 Hz, 1H), 7.36 (s, 1H), 7.00 (t, *J* = 6.9 Hz, 1H), 6.91 (d, *J* = 7.4 Hz, 1H), 6.81 (t, *J* = 7.3 Hz, 1H), 6.71 (dd, *J* = 7.9 Hz, 2H).^{13}C NMR (101 MHz, DMSO) δ 189.9, 147.1, 139.9, 139.6, 130.5, 127.9, 127.4, 126.3, 123.1, 116.6, 115.8, 115.2, 113.8. HRMS (ESI-TOF) m/z: $[M+H]^+$ Calc'd for $C_{13}H_9NOS$ [228.0405]; Found 228.0405.

doi:10.6342/NTU202201631

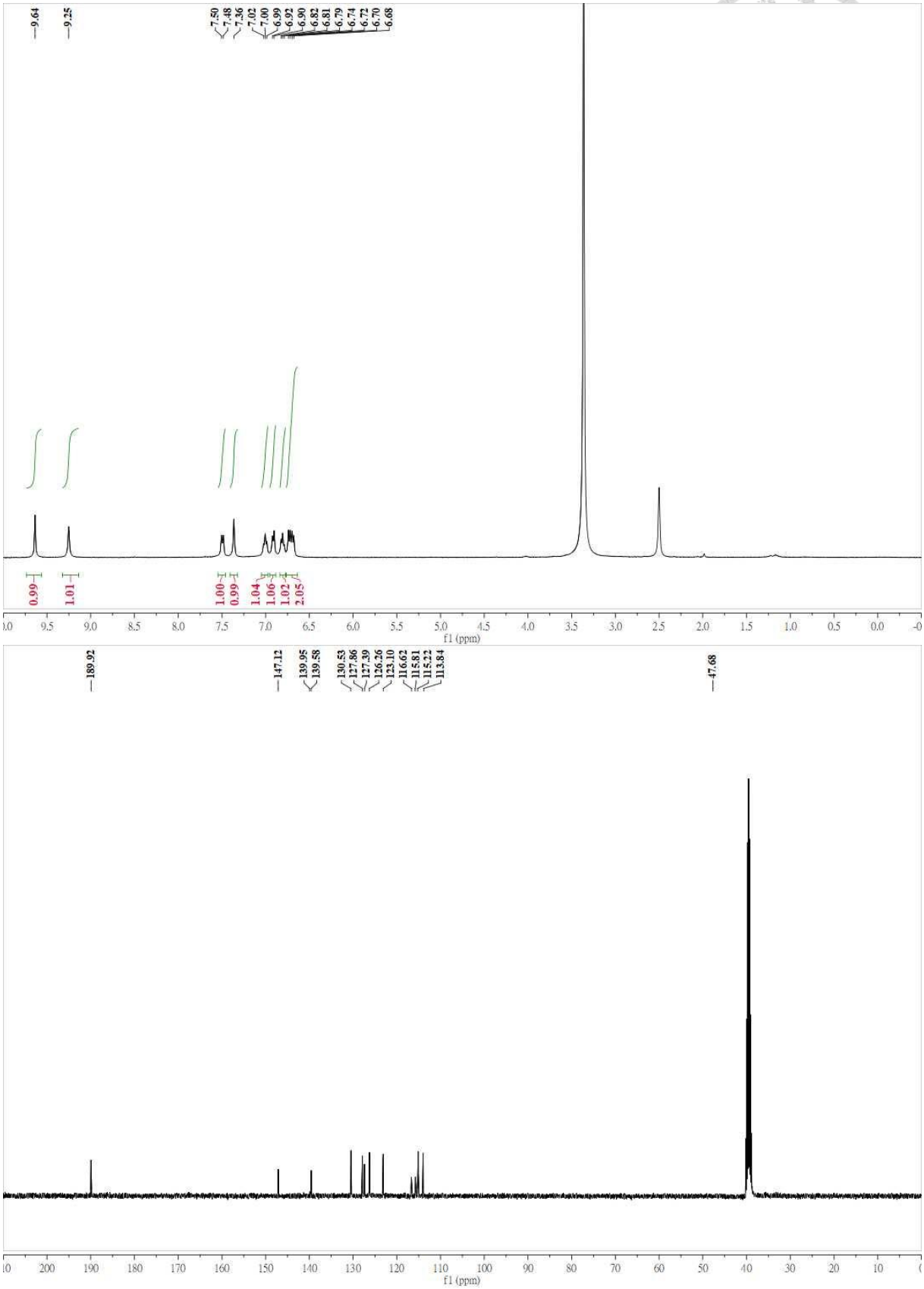

Figure S1-8. ^{1}H &^{13}C NMR of **PTZ-CHO**.

doi:10.6342/NTU202201631

1.5.3.3 Synthesis of **PTZ-CN**

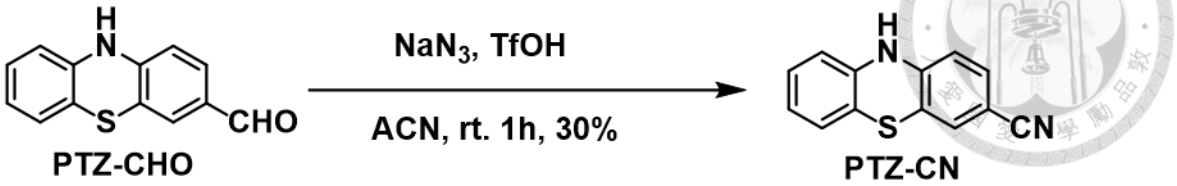

To the solution of **PTZ-CHO** (0.3 g, 1.32 mmole, 1 equiv.) and sodium azide (0.258 g, 3.96 mmole, 3 equiv.) in the acetonitrile (10 ml) was fast stirred and added by triflic acid (0.70 ml, 7.93 mmole, 6 equiv.) in the room temperature for one hour. After completion of reaction, the reactant was extracted with ethyl acetate and brine. The organic layer was separated, dried over $MgSO_4$ and then concentrated by rotavapor. The crude product was purified by silica column (ethyl acetate: hexane = 1:3, R_f = 0.45). The pure product **PTZ-CN was** green powder (0.089 g, 0.396 mmole, 30%). m.p. = 161°C, FT-IR (cm^{-1}): 3322, 3162, 3054, 2219, 1557, 1514, 1478, 814. ^{1}H NMR (400 MHz, DMSO) δ 9.18 (s, 1H), 7.37 (d, J = 7.4 Hz, 2H), 7.01 (t, J = 7.6 Hz, 1H), 6.91 (d, J = 7.6 Hz, 1H), 6.81 (t, J = 7.4 Hz, 1H), 6.75 – 6.64 (m, 2H).^{13}C NMR (101 MHz, DMSO) δ 145.9, 139.7, 132.1, 129.5, 128.0, 126.4, 123.2, 118.9, 117.2, 115.5, 115.1, 114.2, 102.9. HRMS (ESI-TOF) m/z: $[M+H]^+$ Calc'd for $C_{13}H_8N_2S$ [225.0408]; Found 225.0408.

doi:10.6342/NTU202201631

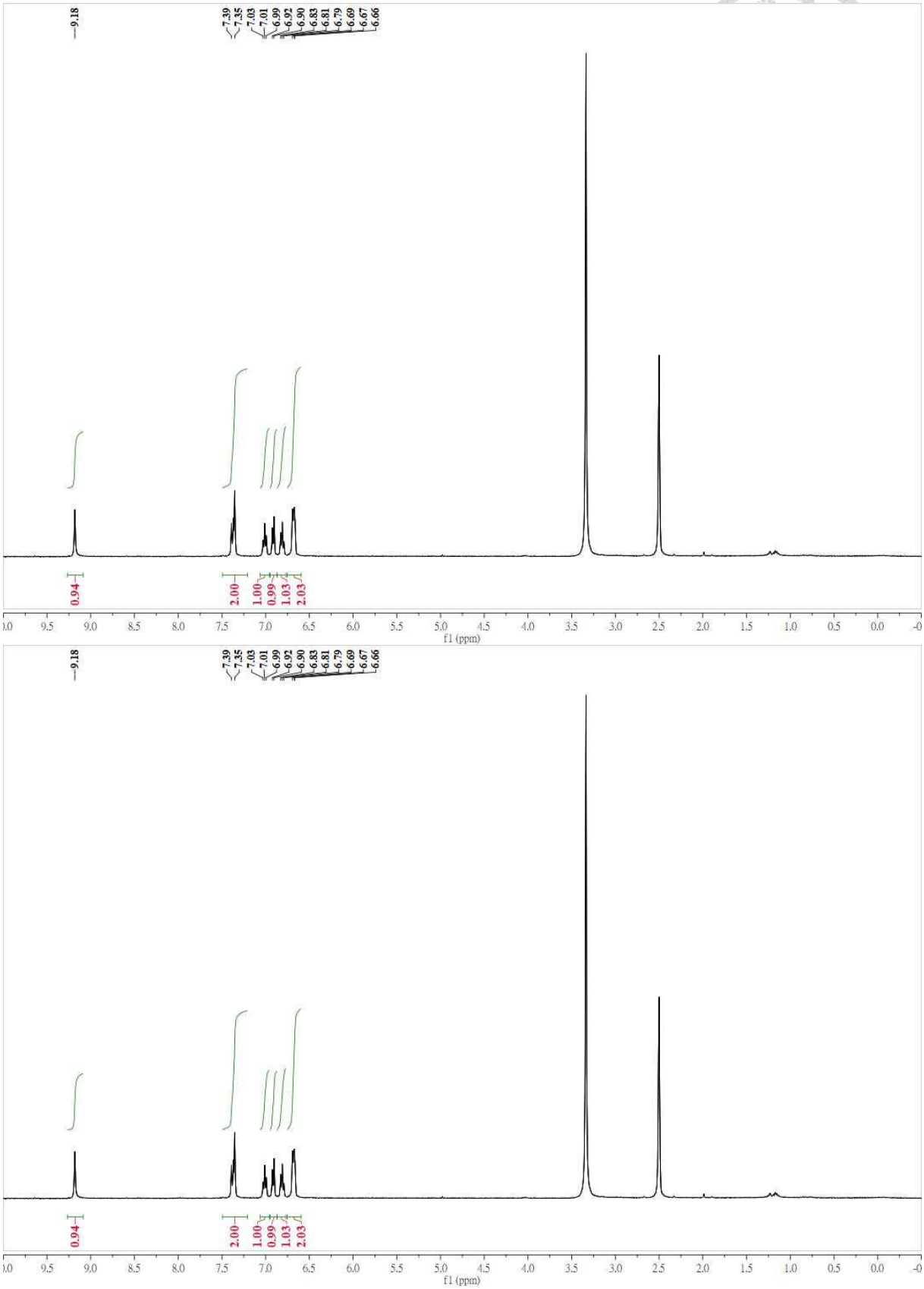

Figure S1-9. ^{1}H &^{13}C NMR of **PTZ-CN**.

doi:10.6342/NTU202201631

1.5.3.4 Synthesis of **DPA-OMe**

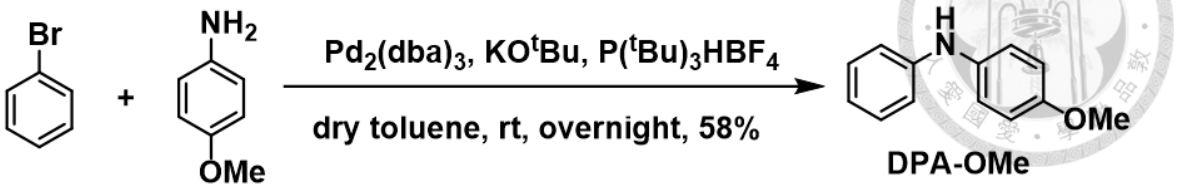

To the solution of 4-methoxylaniline (3.53 g, 28.7 mmole, 1.5 equiv.), bromobenzene (3.00 g, 19.1 mmole, 1.0 equiv.), potassium tert-butoxide (2.79 g, 24.8 mmole, 1.3 equiv.), Tri-tert-butylphosphonium tetrafluoroborate (330 mg, 1.15 mmole, 0.06 equiv.) and Tris(dibenzylideneacetone) dipalladium (0) (52.4 mg, 0.057 mmole, 0.03 equiv.) in dry toluene (50 ml) was degassed by nitrogen and stirred in the room temperature overnight. After completion of reaction, the reactant was extracted with ethyl acetate and brine. The organic layer was separated, dried over $MgSO_4$, and then concentrated by rotavapor. The crude product could be purified by silica column (ethyl acetate: hexane = 1:15, R_f = 0.30). The pure compound **DPA-OMe** was orange powder (2.12 g, 11.0 mmole, 57.9 %). m.p. = 96°C, FT-IR (cm^{-1}): 3387, 3008, 2959, 2931, 2837, 1596, 1502, 1317,1182, 1107, 881, 752. ^{1}H NMR (400 MHz, DMSO) δ 7.82 (s, 1H), 7.15 (t, *J* = 8.7 Hz, 2H), 7.03 (d, *J* = 8.7 Hz, 2H), 6.95 – 6.80 (m, 4H), 6.70 (t, 1H), 3.71 (s, 3H).^{13}C NMR (101 MHz, DMSO) δ 153.7, 145.1, 136.0, 129.6, 120.2, 118.4, 114.8, 114.4, 55.0. HRMS (ESI-TOF) m/z: $[M+H]^+$ Calc'd for $C_{13}H_{13}NO$ [200.0997]; Found 200.0997.

doi:10.6342/NTU202201631

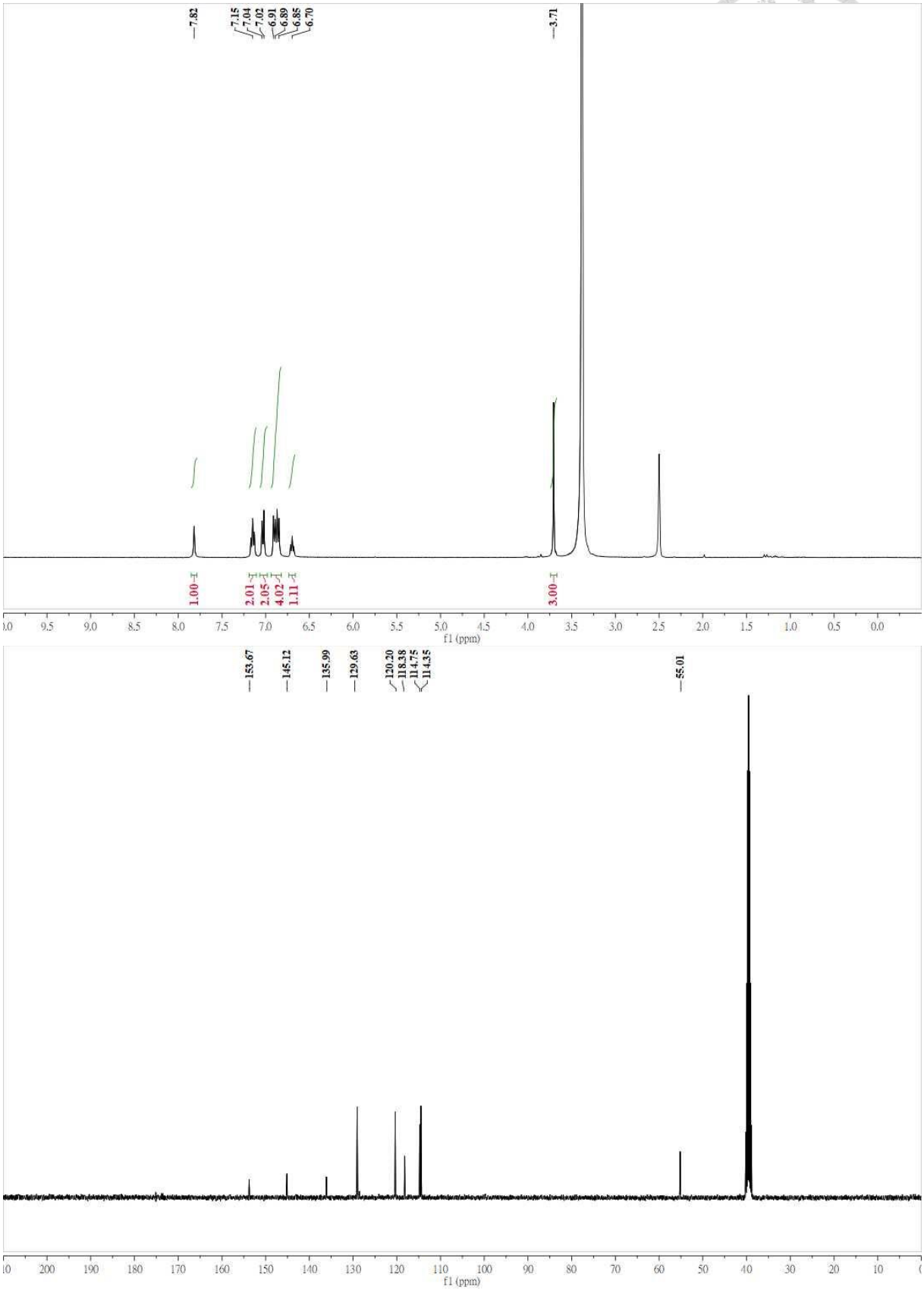

Figure S1-10. ^{1}H &^{13}C NMR of **DPA-OMe.**

doi:10.6342/NTU202201631

1.5.3.5 Synthesis of **PTZ-OMe**

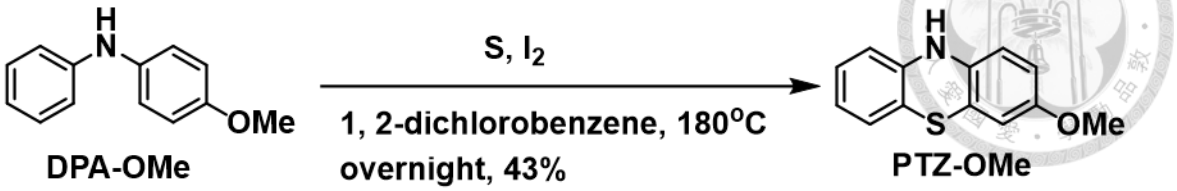

To the solution of **DPA-OMe** (1 g, 5.02 mmole, 1 equiv.), sulfur (320 mg, 10 mmole, 2 equiv.) and iodine (35.7 mg, 0.1406 mmole, 0.028 equiv.) in 1, 2-dichlorobenzene (10 ml) was degassed by nitrogen and refluxed overnight. After completion of reaction, the reactant was extracted by ethyl acetate and brine. The organic layer was separated, dried over $MgSO_4$ and then concentrated by rotavapor. The crude product could be purified by silica column (ethyl acetate: hexane = 1:8, R_f = 0.13). The pure compound **PTZ-OMe** was grey powder (0.50 g, 2.18 mmole, 43.4%). m.p. = 146°C, FT-IR (cm^{-1}): 3366, 3064, 2960, 1579, 1461, 1237, 1180, 816, 742. ^{1}H NMR (400 MHz, DMSO) δ 8.37 (s, 1H), 6.97 (s, 1H), 6.91 (s, 1H), 6.72 (s, 1H), 6.69 – 6.53 (m, 4H), 3.65 (s, 3H). ^{13}C NMR (101 MHz, DMSO) δ 154.6, 142.7, 135.7, 127.5, 126.0, 121.4, 117.4, 115.9, 115.0, 114.3, 113.2, 111.4, 55.6. HRMS (ESI-TOF) m/z: $[M+H]^+$ Calc'd for $C_{13}H_{11}NOS$ [230.0561]; Found 230.0561.

doi:10.6342/NTU202201631

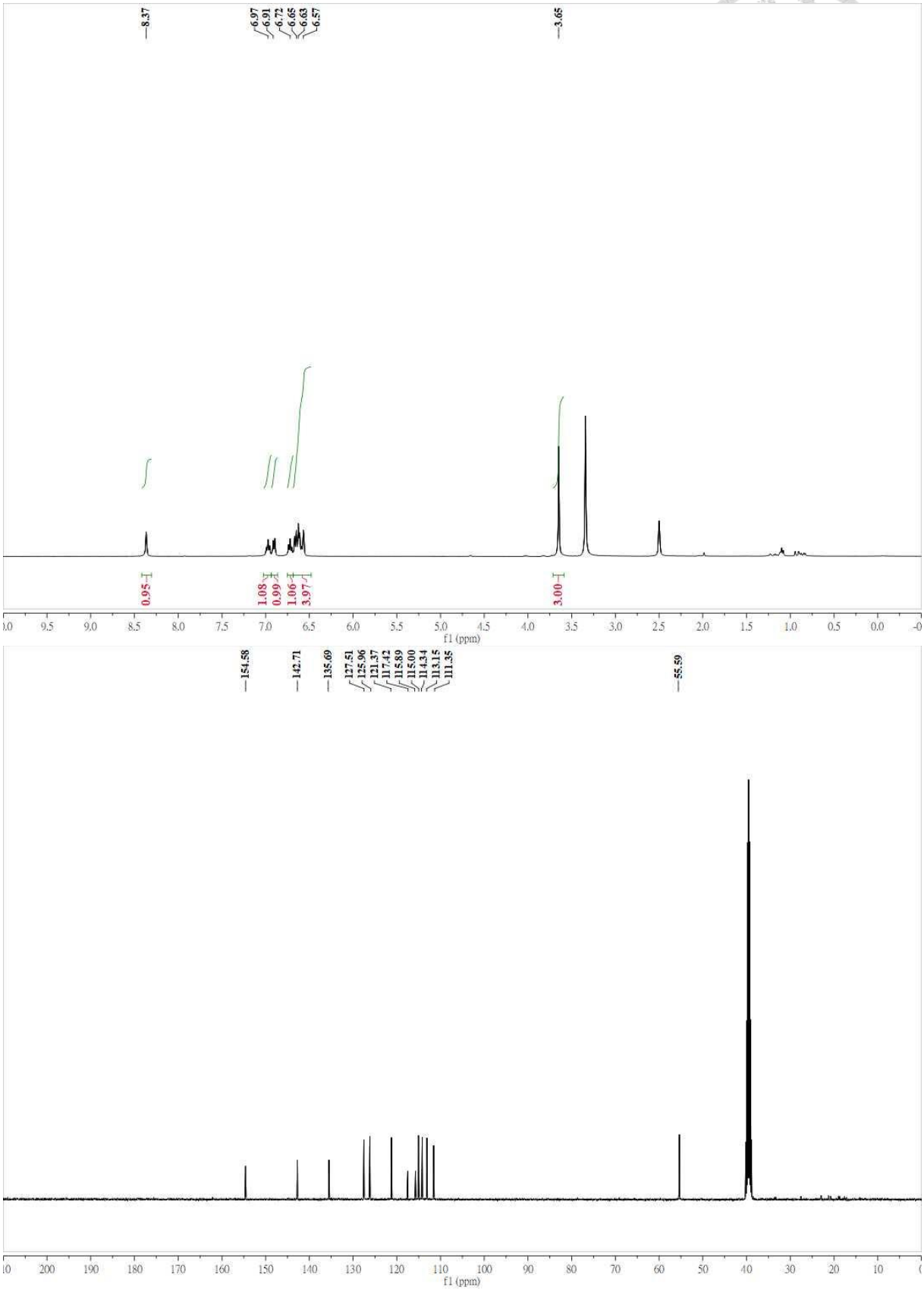

Figure S1-11. ^{1}H &^{13}C NMR of **PTZ-OMe**.

doi:10.6342/NTU202201631

1.5.4 Crystal Data and Structure

1.5.4.1 Crystal data and experimental details for **PTZ-NO_2**

Empirical formula	$C_{12}H_8N_2O_2S$
Formula weight	244.26
Crystal system	Orthorhombic
Space group	$Pna2_1$
Unit cell dimensions	a = 18.0720(19) Å b = 14.985(2) Å c = 3.7505(5) Å
Volume	1015.7(2) $Å^3$
Z	4
F(000)	504
Density (calculated)	1.597 Mg/m^3
Wavelength	0.71073 Å
Cell parameters reflections used	1125
Theta range for Cell parameters	3.5270 to 28.2310°.
Absorption coefficient	0.307 mm^{-1}
Temperature	100(2) K
Crystal size	0.20 x 0.10 x 0.10 mm^3
Diffractometer	Xcalibur, Atlas, Gemini
Absorption correction	Semi-empirical from equivalents
Max. and min. transmission	1.00000 and 0.87526
No. of measured reflections	3788
No. of independent reflections	3788 [R(int) = 0.0906]
No. of observed [I>2_igma(I)]	2681
Completeness to theta = 25.242°	99.5 %
Theta range for data collection	3.532 to 27.442°.
Final R indices [I>2sigma(I)]	R1 = 0.0680, wR2 = 0.1587
R indices (all data)	R1 = 0.1007, wR2 = 0.1744
Goodness-of-fit on F^2	1.021
No. of reflections	3788
No. of parameters	158
No. of restraints	1
Absolute structure parameter	0.38(14)
Largest diff. peak and hole	0.866 and -0.925 e.$Å^{-3}$

doi:10.6342/NTU202201631

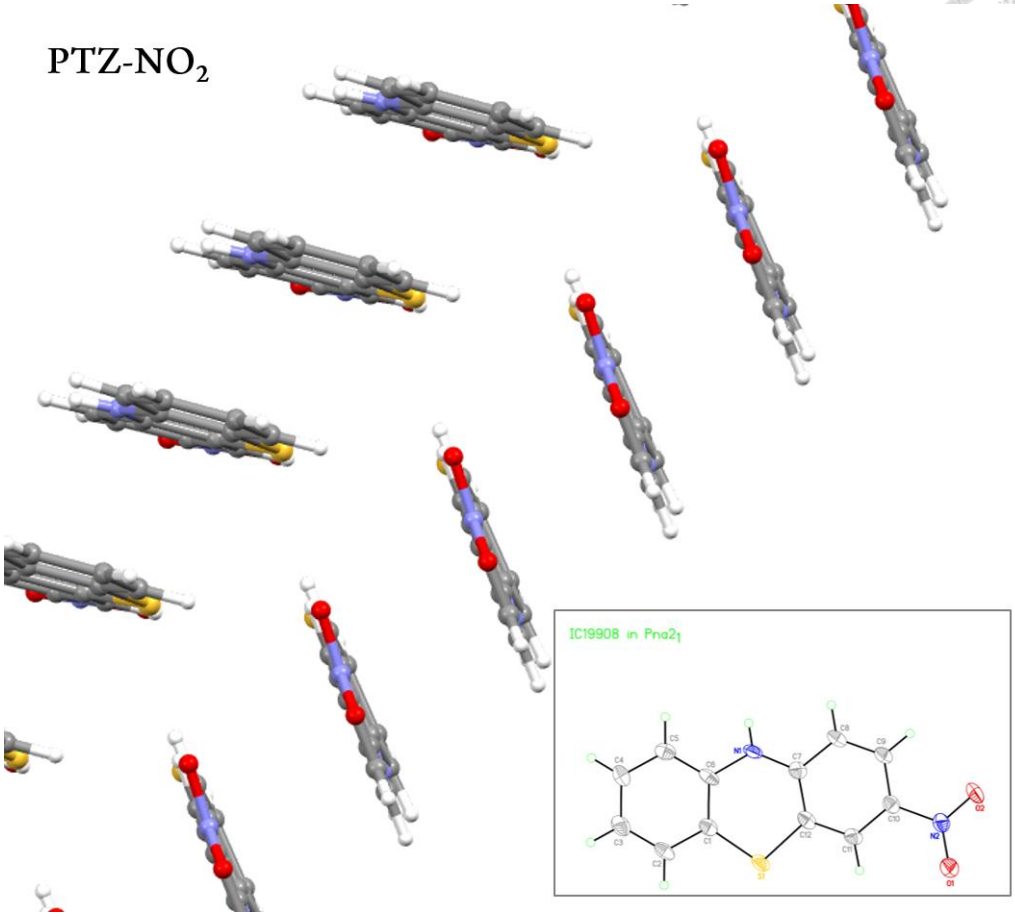

Figure S1-12. X-ray crystal structure of **PTZ-NO_2**.

doi:10.6342/NTU202201631

1.5.4.2 Crystal data and experimental details for **PTZ-CHO**

Empirical formula	$C_{13}H_9NOS$
Formula weight	227.27
Crystal system	Orthorhombic
Space group	$Pna2_1$
Unit cell dimensions	a = 7.5021(3) Å b = 23.0537(8) Å c = 5.9064(2) Å
Volume	1021.52(6) $Å^3$
Z	4
F(000)	472
Density (calculated)	1.478 Mg/m^3
Wavelength	0.71073 Å
Cell parameters reflections used	2469
Theta range for Cell parameters	3.5380 to 29.1410°.
Absorption coefficient	0.289 mm^{-1}
Temperature	100(2) K
Crystal size	0.20 x 0.20 x 0.15 mm^3
Diffractometer	Xcalibur, Atlas, Gemini
Absorption correction	Semi-empirical from equivalents
Max. and min. transmission	1.00000 and 0.52884
No. of measured reflections	4427
No. of independent reflections	1544 [R(int) = 0.0283]
No. of observed [I>2_igma(I)]	1431
Completeness to theta = 25.242°	99.9 %
Theta range for data collection	2.855 to 27.497°.
Final R indices [I>2sigma(I)]	R1 = 0.0323, wR2 = 0.0969
R indices (all data)	R1 = 0.0366, wR2 = 0.1068
Goodness-of-fit on F^2	0.871
No. of reflections	1544
No. of parameters	148
No. of restraints	1
Absolute structure parameter	0.00(8)
Largest diff. peak and hole	0.304 and -0.247 e.$Å^{-3}$

doi:10.6342/NTU202201631

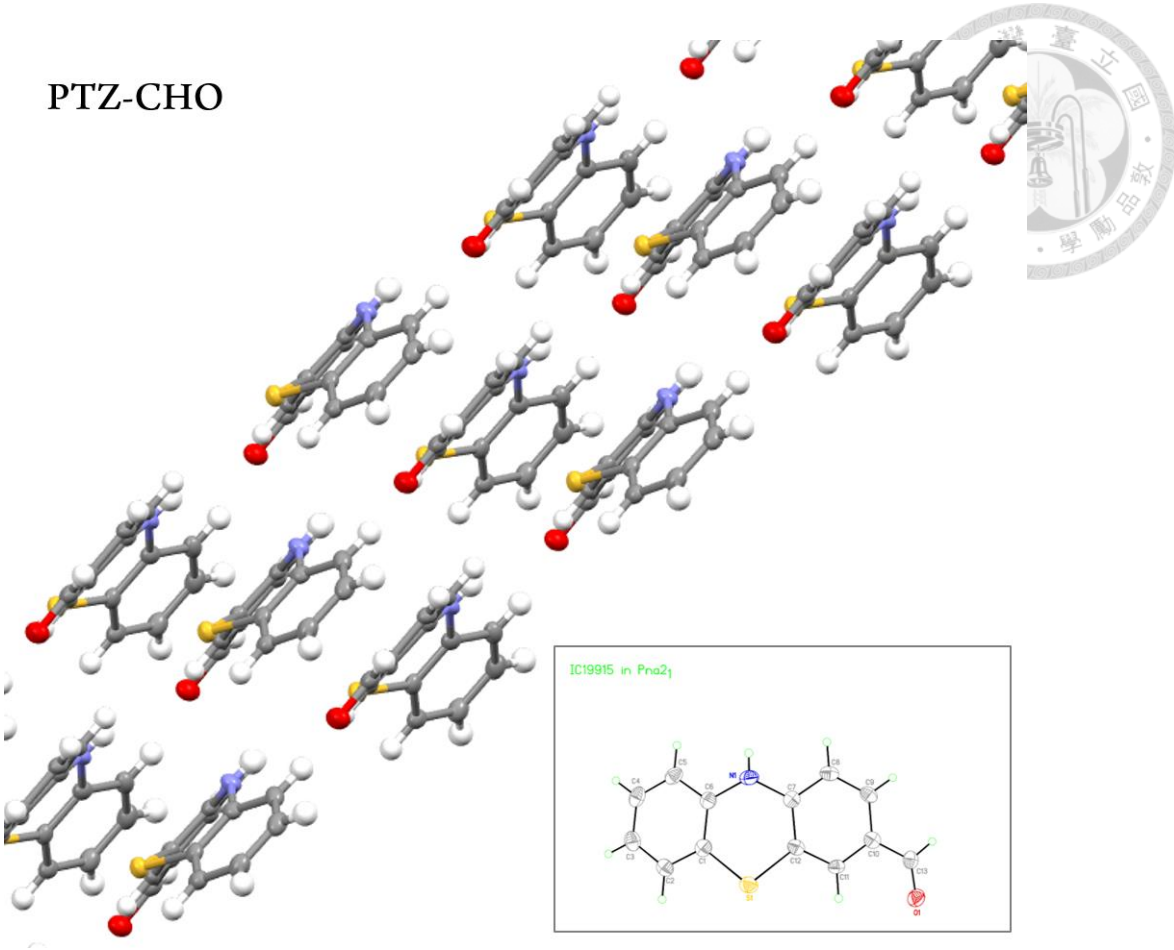

Figure S1-13. X-ray crystal structure of **PTZ-CHO.**

doi:10.6342/NTU202201631

1.5.4.3 Crystal data and experimental details for **PTZ**

Empirical formula	$C_{12}H_9NS$
Formula weight	199.26
Crystal system	Monoclinic
Space group	$P2_1/n$
Unit cell dimensions	a = 5.8205(3) Å
	b = 7.7778(4) Å
	c = 20.7569(17) Å
Volume	936.12(10) $Å^3$
Z	4
F(000)	416
Density (calculated)	1.414 Mg/m^3
Wavelength	0.71073 Å
Cell parameters reflections used	1506
Theta range for Cell parameters	3.5560 to 27.3880°.
Absorption coefficient	0.297 mm^{-1}
Temperature	100(2) K
Crystal size	0.20 x 0.15 x 0.10 mm^3
Diffractometer	Xcalibur, Atlas, Gemini
Absorption correction	Semi-empirical from equivalents
Max. and min. transmission	1.00000 and 0.67271
No. of measured reflections	4841
No. of independent reflections	2080 [R(int) = 0.0461]
No. of observed [I>2_igma(I)]	1483
Completeness to theta = 25.242°	99.9 %
Theta range for data collection	3.278 to 27.500°.
Final R indices [I>2sigma(I)]	R1 = 0.0681, wR2 = 0.2017
R indices (all data)	R1 = 0.1029, wR2 = 0.2225
Goodness-of-fit on F^2	1.298
No. of reflections	2080
No. of parameters	130
No. of restraints	0
Largest diff. peak and hole	0.623 and -0.432 $e.Å^{-3}$

doi:10.6342/NTU202201631

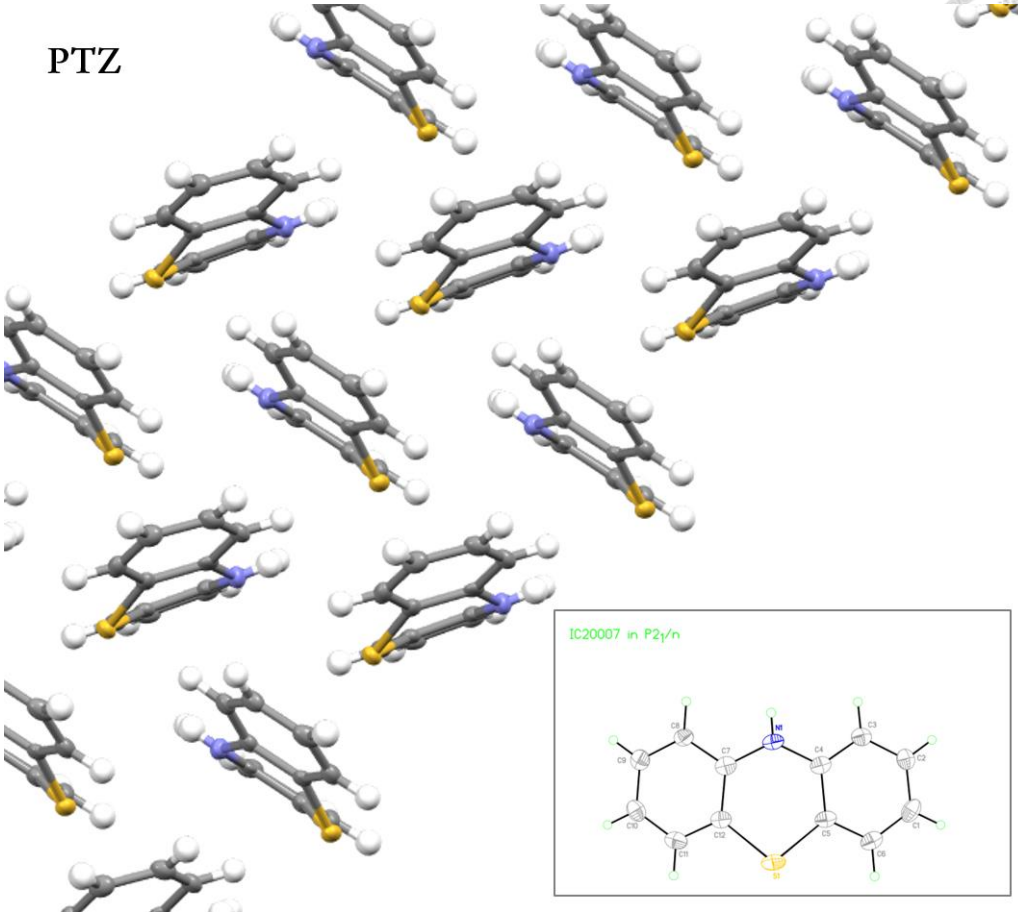

Figure S1-14. X-ray crystal structure of **PTZ.**

doi:10.6342/NTU202201631

1.5.4.4 Crystal data and experimental details for **PTZ-OMe**

Empirical formula	$C_{13}H_{10}NOS$
Formula weight	228.28
Crystal system	Monoclinic
Space group	$P2_1/c$
Unit cell dimensions	a = 5.7812(7) Å
	b = 7.7504(14) Å
	c = 23.437(5) Å
Volume	1050.0(3) Å3
Z	4
F(000)	476
Density (calculated)	1.444 Mg/m3
Wavelength	0.71073 Å
Cell parameters reflections used	321
Theta range for Cell parameters	3.5250 to 24.3760°.
Absorption coefficient	0.282 mm-1
Temperature	100(2) K
Crystal size	0.20 x 0.10 x 0.01 mm3
Diffractometer	Xcalibur, Atlas, Gemini
Absorption correction	Semi-empirical from equivalents
Max. and min. transmission	1.00000 and 0.91230
No. of measured reflections	2846
No. of independent reflections	2846 [R(int) = 0.1800]
No. of observed [I>2_igma(I)]	1390
Completeness to theta = 25.242°	99.8 %
Theta range for data collection	3.151 to 27.495°.
Final R indices [I>2sigma(I)]	R1 = 0.0711, wR2 = 0.0927
R indices (all data)	R1 = 0.1615, wR2 = 0.1090
Goodness-of-fit on F2	0.841
No. of reflections	2846
No. of parameters	146
No. of restraints	0
Largest diff. peak and hole	0.479 and -0.448 e.Å-3

doi:10.6342/NTU202201631

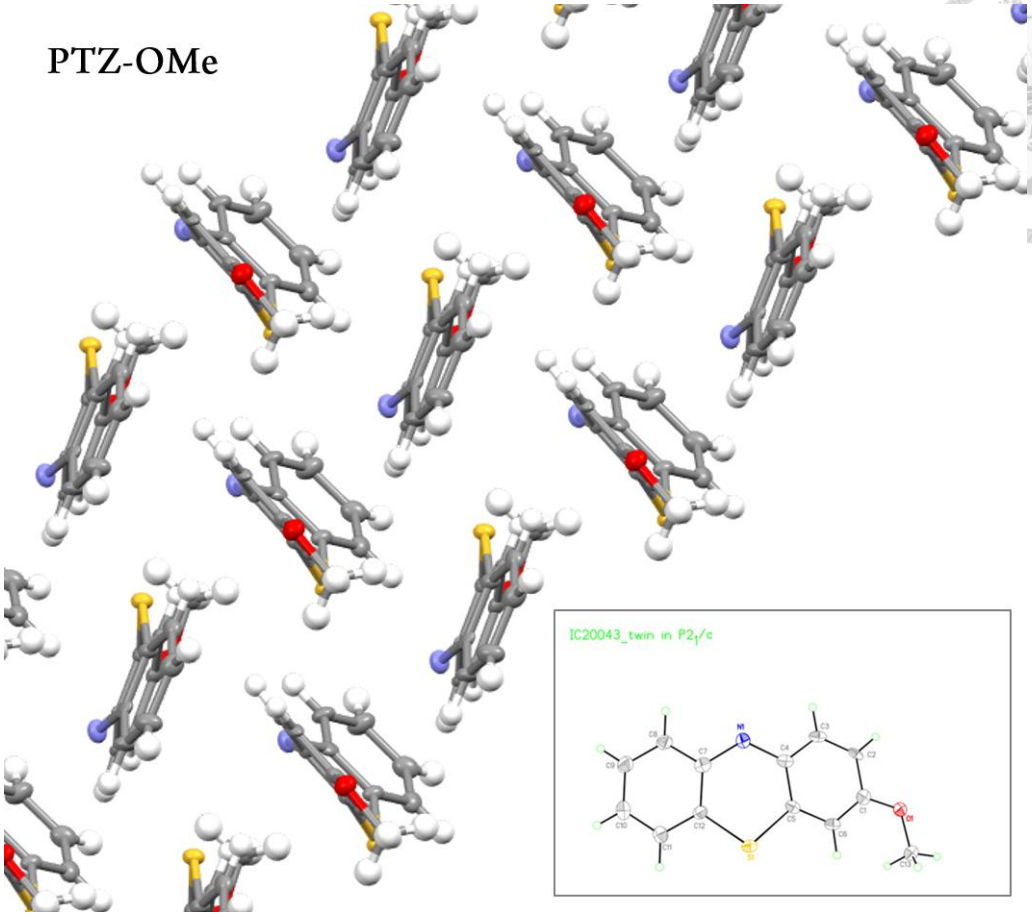

Figure S1-15. X-ray crystal structure of **PTZ-OMe**.

doi:10.6342/NTU202201631

doi:10.6342/NTU202201631

Part II. Comprehensive Thione Derived Perylene Diimides and Their Bio-Conjugation for Simultaneous Imaging Tracking and Targeted Photodynamic Therapy

2.1 Introduction

Photodynamic therapy (PDT) has long been receiving considerable interest in the cancer therapy.[1] Compared to traditional therapies such as surgery, radiotherapy and chemotherapy, PDT possesses obvious advantages such as non-invasive therapy, spatiotemporal selectivity and inexpensive treatment.[2] However, PDT encountered several challenges such as inadequate light penetration, insufficient oxygen dependence, lack of selectivity on cancer cells, which prevents PDT from further clinical applications.[3] To address these concerns, numerous researches have been reported. On the one hand, heavy metal-incorporated inorganic PDT materials are able to enhance ISC, yielding efficient triplet exciton for the production of reactive oxygen species (ROS) via type I and/or type II processes.[4] However, they may also increase dark toxicity and residues to threat human health.[5] On the other hand, metal-free organic materials could easily be digested by human body, but they seldom have sufficient ROS yield like those inorganic PDT materials.[5b, 6]

Among various organic PDT relevant works, special attention has been paid to thiol-based compounds due to their me- al ion-free property and potential biocompatibility.[7] The slightly heavier sulfur atom (cf. oxygen) and its lifted nonbonding (lone pair) electron, hence the nπ* configuration as the lowest lying excited state in the singlet manifold, greatly enhanced rate of intersystem crossing (ISC) to yield triplet excitons for ROS production. In this regard, Xiao's team has synthesized several thiol-based dyes applied

doi:10.6342/NTU202201631

for PDT.[8] They connected the photosensitizer to antibody for cancer-selectivity formed nanoparticles (NPs) and proved their effective PDT. Yoon's team reported the NPs formation of thiol-carbonyl naphthalimide derivatives in water,[9] where the as prepared NPs diimide nano-agents had been exploited for photodynamic and photothermal therapy,[10] and the results revealed that the position of sulfur did not affect the PDT efficacy. Among numerous potential PDT drugs, 3,4,9,10-perylenetetracarboxylic diimide (PDI) was an ideal choice of photosensitizer because PDI possessed not only two substituted sides for further modification of the functionalized groups but also special properties such as intense absorption, near 100% fluorescence quantum yield in diluted solutions, good stability and sufficient two photon absorption.[11] It was also worth noting that substitution on two imide positions may not affect PDI's optical properties but rather influenced the solubility and morphology in hydrophilic solvents.[12] In most of cases, PDI derivatives had poor solubility in common organic solvents; therefore, they were rarely used toward bio-applications such as fluorescence probes,[13] biomarkers[14] or photosensitizers.[15] From chemistry point of view, if one could find tailorable substitutions on the imide moiety of the PDI derivatives with high solubility, they would have been far-reaching for the PDT relevant materials.

Moreover, it was pivotal to design a heavy-metal free PDT drug that had multiple functionalities, including good two-photon absorption cross section, imaging ability and specific selectivity on cancer cells.[16] Two-photon excitation could help deeper tissue penetration to heal the tumor, overcoming, in part, the limitation of PDT on the shallow surface treatment.[17] Imaging PDT contributed to monitor both movement and location of drugs, which could help investigate its pharmacokinetics.[18] Also, importantly, the sensitized ROS would locate at the designated position in proximity of the cancer cells to destroy selectively the malignant cell.[19]

doi:10.6342/NTU202201631

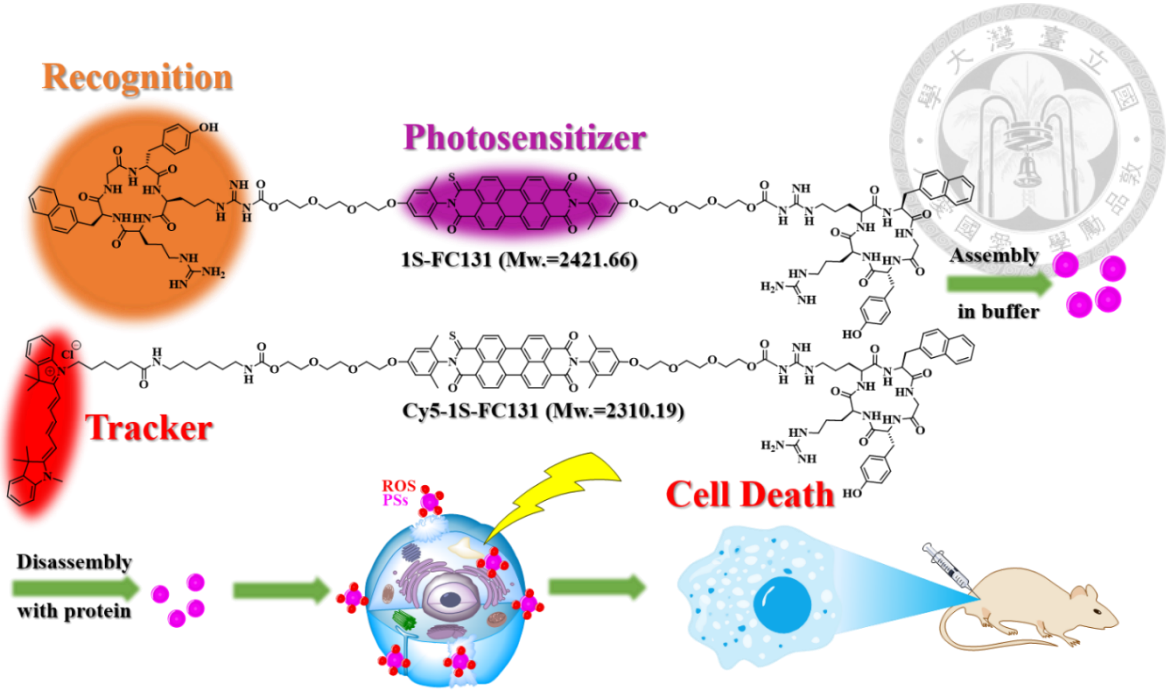

Figure 2- 1 Schematic illustration of the process from assembly (630-700 nm) and disassembly (5-15nm) of **1S-FC131** and **Cy5-1S-FC131** in buffer solution, causing cell apoptosis under irradiation.

In this study, via tailoring PDI with short-chain alkyl or phenyl substituents at the imide N- site, followed by delicate thionation, we have synthesized and characterized a series of thione derived PDI products named as **nS-PDIs** (**nS** denotes n number of thiol groups, see Figure 1a). Note that the long chain-alkyl anchored thione PDI derivatives have been studied regarding their photophysics in the organic solvents.[20] However, the sparse solubility of the long chain-alkyl anchored thione PDI derivatives in water prohibited further bio-conjugation, Alternatively, in this study, the **nS-PDI**s with nonplanar 2,6-dimethylphenyl substitution on the N-imide position, namely **1S-PDI-D**, **2S-*cis*-PDI-D** (or **2S-*trans*-PDI-D**), **3S-PDI-D** and **4S-PDI-D**, specifying n= 1, 2, 3 and 4 thione groups, respectively (see Figure 2-2a) were designed and synthesized. All **nS-PDI-D**s had good solubility due to the reduced π stacking via orthogonal configuration between 2,6-dimethylphenyl and PDI moieties, among which **1S-PDI-D** was then

doi:10.6342/NTU202201631

strategically linked specifically by a targeting peptide, FC131 (cyclo-[2-NaI-Gly-D-Tyr-Arg-Arg]), on both terminals using triethylene glycol as a bridge, yielding **1S-FC131** (Scheme 1) FC131 was an antagonist of CXCR4-ligand binding,[21] where CXCR4 served as a chemokine receptor in cell surface and had proved to overexpress in more than 23 human cancer cells including A549 cells applied in this study.[22] To endow more functionality, **1S-PDI-D** was further modified by linking FC131 on one side and a well-known biocompatible fluorescent dye Cyanine 5 on the other side, forming **Cy5-1S-FC131** (see Figure 2-1). Both **1S-FC131** and **Cy5-1S-FC131** were able to self-assemble to particles in buffer, followed by disassembly to small nanoparticles upon interacting with proteins. Therefore, they were able to selectively target the cancer cells and generate ROS upon excitation, causing cell apoptosis *in vitro* and *in vivo*. The imaging ability on **Cy5-1S-FC131** further helped confirm the location of drug in cell and the distribution in mouse's organs. Detail of results and discussion were elaborated as follows.

doi:10.6342/NTU202201631

2.2 Results and Discussions

2.2.1 Design Strategy

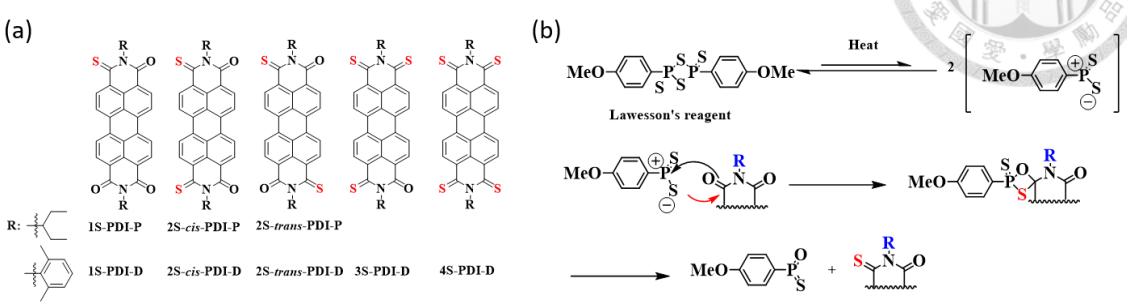

Figure 2- 2 (a) Various R substitutes and structure of R substituted n**S-PDI**s. Note that R=2,6-dimethylphenyl has good solubility. Therefore, the name of nS-PDIs is specifically for those R=2,6-dimethylphenyl. (b) The depiction of general mechanism of the Lawesson's reaction

While the choice of PDI as the core chromophore stems from its advantage in stability and versatility in derivatization, PDI was subject to sparse solubility and self-assembly, i.e. aggregation.[23] We realized that the obstacle of solubility can be overcome by using long chain alkyl group.[38] Unfortunately, this strategy hampered further bio-conjugation in the buffer solution. This was especially critical in the later bio-conjugation. Therefore, our first strategy was to synthesize PDIs with two different short side chain, 3-pentyl (**PDI-P**), and 2,6-dimethylphenyl groups (**PDI-D**) shown in Figure 2-2a and systematically investigate their solubility and reactivity. As a result, **PDI-P** and **PDI-D** had improved the solubility in most of common organic solvents due to their weak π-π stacking.[24] Compared to **PDI-D**, we also found that **PDI-P** was difficult to transform PDI to tri- or tetra-thiol-substituted compound via Lawesson reagent in our later experiments. This possibly resulted from the different inductive effect of hybrid orbitals C (sp_3) for 3-pentyl- versus C (sp_2) for 2,6-dimethylphenyl- substituents. The C (sp^2) orbital was stronger in electron-withdrawing than that of C (sp^3) orbital, making the

doi:10.6342/NTU202201631

carbonyl of **PDI-D** more electron-deficient (see Figure 2-2b). In other words, for **PDI-D**, the carbonyl group was more partially negative and had higher reactivity in a concerted cycloaddition to form a four-membered intermediate between the monomer of Lawesson reagent and the carbonyl group (Figure 2-21b).[25] As a result, **PDI-D** was able to generate comprehensive mono-, di-, tri-, tetra-thione-substituted compounds, **1S-PDI-D**, **2S-*cis*-PDI-D**, **2S-*trans*-PDI-D**, **3S-PDI-D**, and **4S-PDI-D** (see Figure 2-1a). Details of synthesis and characterization were elaborated in the supporting information

doi:10.6342/NTU202201631

2.2.2 Steady state spectra and assignment

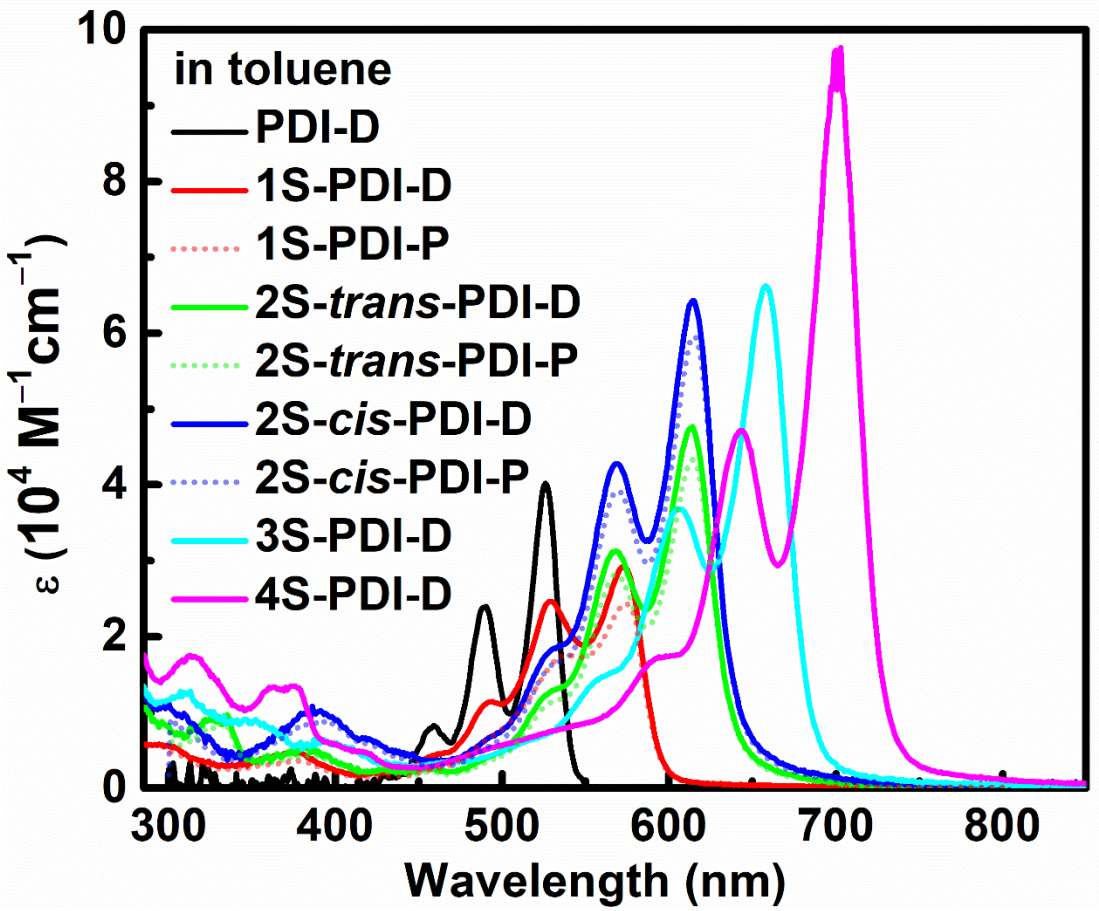

Figure 2- 3 Absorption spectra (in terms of ε values) of PDI, n**S-PDI-P**s (n=1 and 2) and n**S-PDI-D**s (n= 1-4) in toluene.

Figure 2-3 showed the absorption spectra of comprehensive **nS-PDI-D**s derivatives (n = 1-4) and the rest synthesized **nS-PDI**s such as those **nS-PDI-P**s (n =1 and 2) and the reference compound **PDI-D** in toluene. For all these compounds, the absorbance was found to be proportional to the concentration without changes of the spectral profile within 10^{-7} to 10^{-4} M, eliminating the possibility of the aggregation effect. Several remarks could be pointed out from the results. First, the absorption spectra spanning in the visible region all had large extinction coefficients of > 10^4 $M^{-1}cm^{-1}$ (see Table 2-1), inferring their ππ* transition character in nature. Second, the absorption peak wavelength,

doi:10.6342/NTU202201631

being independent of N-substitution, was varied by the number of thione groups and was largely red shifted upon increasing the number of thione groups. For example, the peak wavelength of **1S-PDI-D** and **1S-PDI-P** were nearly the same at 580 nm (cf. Figure 2-3), while it shifted to as long as 700 nm in **4S-PDI-D**. The results indicated that the N-substituted groups did not play a role while thione did in this $\pi \rightarrow \pi^*$ transition.

Despite the allowed transition of $\varepsilon > 10^4\ M^{-1}cm^{-1}$ at the peak wavelength (see Figure 2-3), all synthesized n**S-PDI**s were virtually non-emissive in toluene and other common organic solvents at room temperature. As for the long- chain alkyl substituted n**S-PDI**s, they mainly focused on the transient absorption study, like Tilley et al work. [38] They concluded that the fast rate of intersystem crossing predominantly quenched the emission. However, detailed correlations of state energy and configuration were not elaborated; especially the N-substituent effect played a key role for the difference of n**S-PDI**s in the triplet state properties (vide infra).

To gain further insight into the transition properties, relevant frontier molecular orbitals were analyzed in both optimized ground and excited states with the energy difference computed by Time-Dependent Density Functional Theory (TD-DFT) for various n**S-PDI**s. Special focus will be on the n**S-PDI-D**s series due to their comprehensive thione derivation. For all n**S-PDI-D**s the lowest transition in the singlet manifold was ascribed to HOMO−1 → LUMO, in which HOMO-1 contained a great portion of thione lone pair electron density (see Figure 2-4 for **1S-PDI-D**, Table S2-1 to S2-4 for the rest n**S-PDI-D**s). The calculated relevant energy for each state was listed in Table 2-1. Clearly, the lowest lying S_1 state possessed an $n\pi^*$ character. In sharp contrast, the higher singlet excitation was ascribed to HOMO → LUMO transition, which was manifested by a $\pi\pi^*$ configuration with a large oscillator strength ($f \sim 1$). The results supported the observed visible absorption to be the $S_0 \rightarrow S_2$ $\pi\pi^*$ transition with large

doi:10.6342/NTU202201631

molar extinction coefficients. Moreover, the lowest triplet state was endowed with a ππ* configuration (T_1(ππ*), see Figure 2-4). The calculated S_2, S_1 and T_1 state energies all showed a spectral red-shifted trend upon increasing the number of thione (see Table 2-1 and Table S2-2), which was also independent of position such as *cis*- versus *trans*- for **2S-PDI-D**. For the optically allowed S_2 (ππ*) state, this red-shifting trend was experimentally verified by the absorption spectra (Figure 2-3). For comparison, Figure 2-4b depicted the state energy diagram and the associated frontier orbitals responsible for the transition for N-alkyl derivative **1S-PDI-P**. For the π (HOMO) → π* (LUMO) transition, the assignment of state configuration and the associated transition between **1S-PDI-D** and **1S-PDI-P** were the same, where N-substituents had negligible contribution to both HOMO and LUMO. The result rationalized the N-substituent independent S_2 (ππ*) energy and hence the $S_0 \rightarrow S_2$ absorption peak wavelength (cf. **1S-PDI-D** and **1S-PDI-P**, see Figure 2-3). Much difference lied in HOMO-1, which incorporated substantial N-phenyl electron density in **1S-PDI-D (**Figure 2-4a**)** but had negligible contribution from N-3-pentyl in **1S-PDI-P** (Figure 2-4b). This results in appreciable difference in the energy of both S_1 (nπ*) and T_2 (nπ*) states, which could not be measured experimentally.

doi:10.6342/NTU202201631

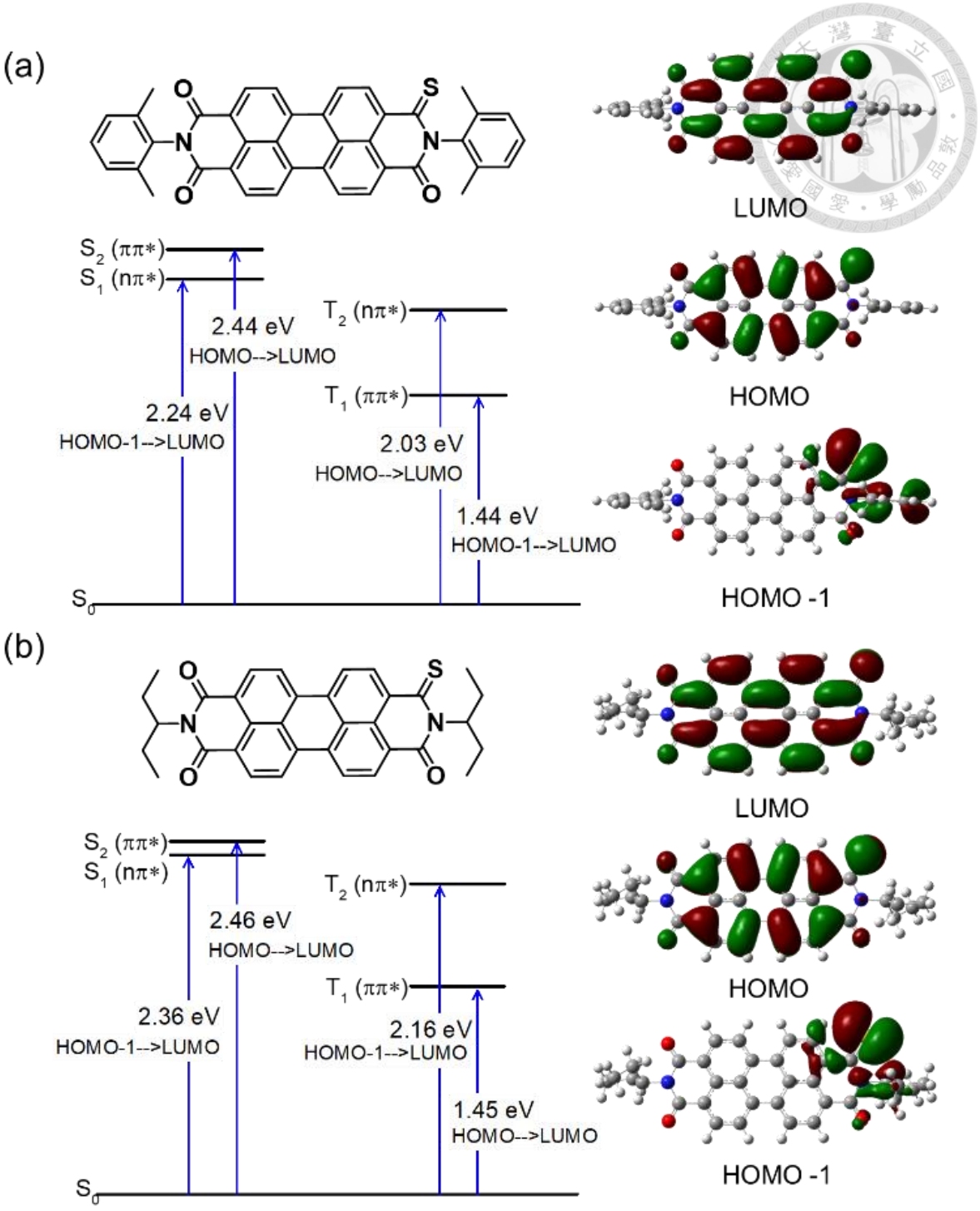

Figure 2- 4 The energy, electronic configuration and the associated frontier molecular orbitals for each state of (a) **1S-PDI-D** and (b) **1S-PDI-P** optimized at the ground state (S_0)

The above steady state and computation results have clearly resolved the configuration of various states and their associated energy is in the order of S_2 (ππ*) > S_1

doi:10.6342/NTU202201631

(nπ*) > T_2 (nπ*) > T_1 (ππ*) for all studied n**S-PDI**s. S_1 (nπ*) → T_1 (ππ*) rate of ISC should be fast due to the change of orbital configuration (n→π*) that assisted spin flipping along ISC, i.e., the operation of El-Sayed rule based on conservation of angular momentum.[26] For long N-alkyl chain substituted n**S-PDI**s, Tilley et al. has concluded that the rate of ISC, k_{isc}, was approximately 10^{12} s^{-1} and its correlation with number of anchored thiones was irregular.[20] In this study, we only focused on the transient absorption of n**S-PDI-D**s where the N-2,6-dimethylphenyl substituent directly involved in the corresponding frontier orbital (HOMO-1, vide supra Figure 2-5 presented the femtosecond temporal evolution and decay dynamics of **1S-PDI-D** while data for the rest n**S-PDI-D**s were depicted in Figure S2-21. For **1S-PDI-D**, the transient absorption was

Table 2- 1. Photophysical data of n**S-PDI-D**s in toluene obtained by either measurement or calculation.

PSs	S_2[a)] nm(eV)	ε[b)] $M^{-1}cm^{-1}$	Cal. S_1 eV[c)]	Cal. T_1 eV[c)]	Φ_Δ[d)]	σ[e)] GM
1S-PDI-D	575(2.16)	29200	1.67	1.10	1.00	976
2S-*cis*-PDI-D	610(2.03)	64300	1.61	0.98	0.39	866
2S-*trans*-PDI-D	610(2.03)	47700	1.61	0.98	0.55	812
3S-PDI-D	660(1.88)	66200	1.24	0.87	0.00	851
4S-PDI-D	700(1.77)	97700	1.19	0.77	0.00	872

[a)] The observed absorption maximum of the S_0 →S_2 transition [b)]extinction coefficient at S_2 peak wavelength measured in toluene; [c)] the calculated energy difference between S_1 (or T_1) and S_0 states in the optimized S_0 structure; [d)] denotes $^1O_2$ generation yield; [e)] two-photon absorption cross section measured in toluene.

doi:10.6342/NTU202201631

composed of an apparent positive absorption band at > 600 nm, a negative, mainly ground-state bleaching signal around 550-600 nm. All plots of the time dependent absorbance at > 720 nm, e.g. 760 nm (see Figure 2-5), revealed a similar pattern, consisting of an instant rise limited by instrument response (120 fs), an ultrafast decay of 600 fs and a nearly time-independent constant absorbance lasting to the limit of fluorescence up-conversion acquisition window of ~1 ns. The 575 nm bleaching signal was nearly constant throughout the 1 ns acquisition window. Upon monitoring at 660 nm, a rise component of ~600 fs was resolved, accompanied by a time-independent constant absorbance. In a brief summary, the > 720 nm absorbance was ascribed to a combination of $S_1 \rightarrow S_n$ and $T_1 \rightarrow T_m$ transient absorption, where the 600 fs decay component should dominated by the rate of S_1 ($n\pi^*$) $\rightarrow T_1$ ($\pi\pi^*$) ISC and the constant absorbance can be unambiguously attributed to the absorption of the long-lived T_1 ($\pi\pi^*$) state. These assignments also rationalized the 575 nm transient that mainly originated from $T_1 \rightarrow T_m$ transient absorption. The bottleneck of the excited-state relaxation lied in the long-lived T_1 ($\pi\pi^*$), rationalizing the nearly constant bleaching signal throughout the acquisition window of ~1000 ps. Similar pattern and hence assignment were given to the rest n**S-PDI-D**s (see Figure S2-21). Assuming that the decay of S_1 was mainly attributed to the rate of ISC of n**S-PDI-D**s, k_{isc} value was then measured to be 1.67×10^{12} s^{-1}, 1.56×10^{12} s^{-1}, 1.85×10^{12} s^{-1}, 1.23×10^{12} s^{-1} and 2.33×10^{12} s^{-1} for **1S-PDI-D**, **2S-*cis*-PDI-D**, **2S-*trans*-PDI-D**, **3S-PDI-D** and **4S-PDI-D**, respectively in toluene (see Table 2-2). The results of ultrafast k_{isc}, together with the small radiative lifetime for the optically forbidden S_1 ($n\pi^*$) state, explained lack of observing any fluorescence for n**S-PDI-D**s. Intuitively, the fast S_1 ($n\pi^*$) $\rightarrow T_1$ ($\pi\pi^*$) ISC manifested the important role of thiones played in k_{isc}. However, similar to the N-alkyl n**S-PDI**s, [38] we noticed that the measured k_{isc} had an irregular trend with respect to e.g. number of thione anchored for the n**S-PDI-D**s series.

doi:10.6342/NTU202201631

For example, k_{isc} for **3S-PDI-D**, counting the experimental uncertainty of 10%, was smaller than that of **3S-PDI-D**. However, **4S-PDI-D** clearly gave the largest k_{isc} among n**S-PDI-D**s.

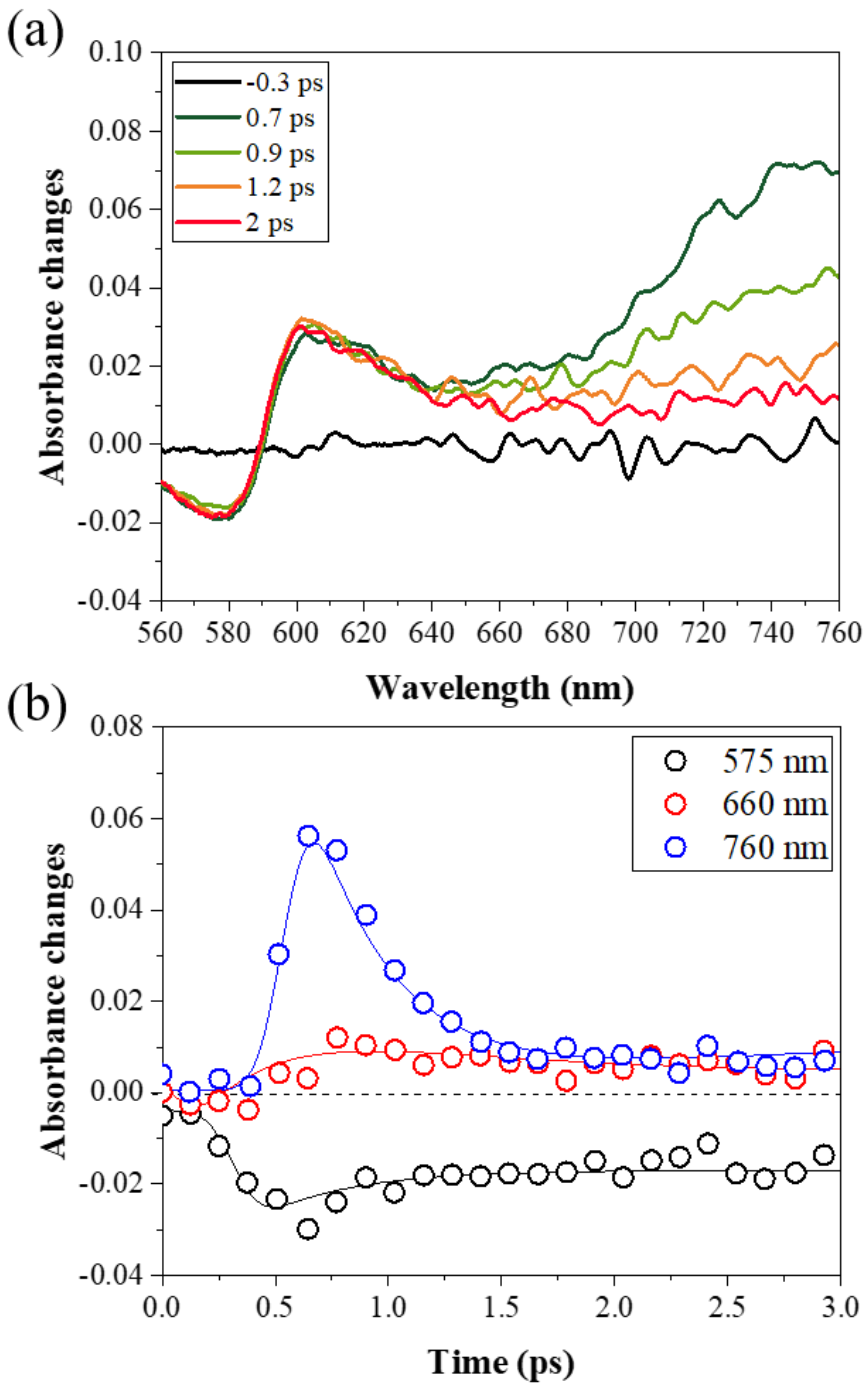

Figure 2- 5 (a) Temporal evolution of **1S-PDI-D** in toluene. (b) The relaxation dynamics of the transient absorption for 1S-PDI-D at various selected wavelengths. λ_{ex}: 575 nm.

doi:10.6342/NTU202201631

To gain in-depth insight into ISC, we then performed the computation of the spin-orbit coupling constant by ADF (Amsterdam Density Functional) version 2020. The results showed a trend of the spin-orbit coupling constant (SOC) of 86.48, 99.78, 113.9. 95.48 and 139.1 cm^{-1} for **1S-PDI-D**, **2S-** ***cis*****-PDI-D** (**2S-*trans*-PDI-D**), **3S-PDI-D** and **4S-PDI-D**, respectively (Table 2-2). The weak coupling (< 200 cm^{-1}) made feasible the calculation of k_{isc} based on eq. (1) expressed as[27]

$$k_{isc} = \frac{2\pi}{\hbar}\langle\phi_{T_1}|H_{SO}|\phi_{S_1}\rangle^2 \frac{1}{\sqrt{4\pi\lambda k_B T}} \sum_{n=0}^{\infty} \exp(-S)\frac{S^n}{n!} \exp\left[-\frac{(\Delta E_{ST} + n\hbar\omega + \lambda)^2}{4\lambda k_B T}\right] \quad (1)$$

where $\langle\phi_{T_1}|H_{SO}|\phi_{S_1}\rangle$ denoted the SOC term, λ was the reorganization energy between S_1 and T_1, S specifies Huang-Rhys factor and $\hbar\omega$ was the collected vibrational mode involved in ISC. In a simplified approach of S= 1 and small $\hbar\omega$ (cf. ΔE_{ST} and λ) with a quantum ladder of n =1, eq. (1) could be simplified to (2) written below[28]

$$k_{isc} = \frac{1}{\hbar}|SOC|^2 \sqrt{\frac{\pi}{\lambda k_B T}} \exp\left[-\frac{(\lambda + \Delta E_{ST})^2}{4\lambda k_B T}\right] \quad (2)$$

The reorganization energy was then calculated and listed in Table 2. Together with the calculated SOC (Table 2-2) and ΔE_{ST} (Table 2-1), Table 2-2 listed the deduced k_{isc} at 298 k based on eq. (2) for various n**S-PDI-D**s. The validity of the computational approach was supportive by the same magnitude comparing experimental and calculated k_{isc} value (see Table 2-2). Nevertheless, difference lied in that the calculated k_{isc} values showed a correlation where increasing thione number resulted in an increase of k_{isc}. We noted that the currently used M062X/6-311+G(d,p) level was insufficient to describe the wavefunction of the d orbital in heavy atom such as sulfur. It required more sophisticate level regarding diffuse and polarization functions, which was too expensive at current stage. Despite this, the ultrafast rate of ISC let us suspect that the discrepancy may lie in

doi:10.6342/NTU202201631

the involvement of the ultrafast rate S_2 ($\pi\pi^*$) $\rightarrow S_1$ ($n\pi^*$) internal conversion, which may interfere with the measured rate of S_1 ($n\pi^*$) $\rightarrow T_1$ ($\pi\pi^*$) ISC. Nevertheless, interestingly, the calculated SOC for **4S-PDI-D** were apparently larger than the rest n**S-PDI-D**s, explaining its largest k_{isc} in both experimental and theoretical approaches.

Table 2- 2 The measured k_{isc} and calculated SOC, λ and deduced k_{isc} of various n**S-PDI-D**s.

	k_{isc}[a] ($10^{12}s^{-1}$)	SOC (cm^{-1})	λ (cm^{-1})	k_{isc}[b] ($10^{12}s^{-1}$)
1S-PDI-D	1.67	86.48	4349.85	1.32
2S-*cis*-PDI-D	1.56	99.78	4990.27	1.57
2S-*trans*-PDI-D	1.85	113.9	4907.19	1.81
3S-PDI-D	1.23	95.48	3666.68	2.01
4S-PDI-D	2.33	139.1	4452.28	4.67

[a] Values obtained from transient absorption data. [b] Values deduced from eq. (2).

doi:10.6342/NTU202201631

2.2.3 Photosensitization

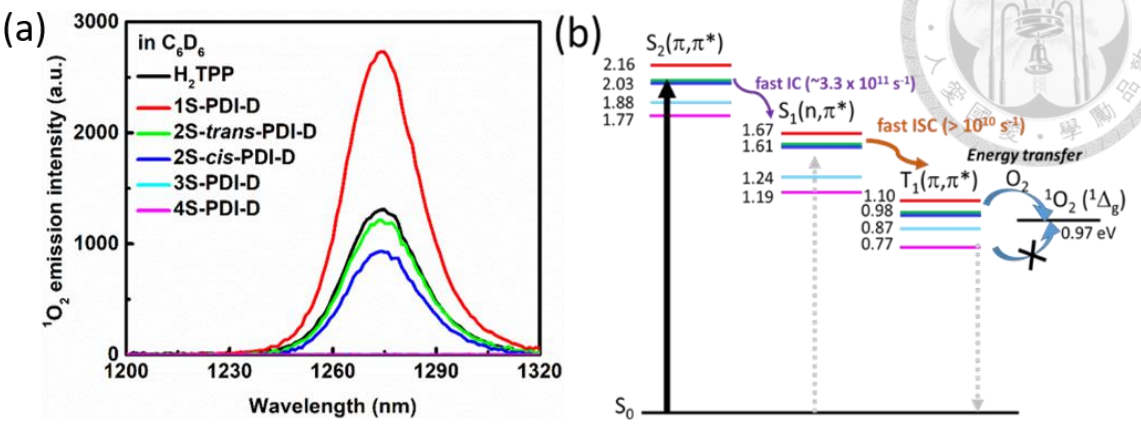

Figure 2- 6 (a) The $^1O_2$ $^1\Delta_g \rightarrow {}^3\Sigma_g^-$ (0,0) emission spectrum of n**S-PDI-D**s are currently available in the lab. (b) The energy and relaxation diagram of n**S-PDI**s and their corresponding O_2 sensitization process. Note: the x-axis was an arbitrary coordinate.

The fast ISC rate ensures ~100% population of the T_1 state, which encouraged us to probe the photosensitization potential of these n**S-PDI**s in the aerated solution, possibly yielding reactive oxygen species (ROS) such as singlet oxygen ($^1O_2$). ROS played a key role in PDT and was worthy for examination. We thus carried out the measurement of $^1O_2$ production efficiency (Φ_Δ) for n**S-PDI**s via triplet (n**S-PDI**s)-triplet (O_2) energy transfer. Φ_Δ could be quantified by comparing the intensity of the 1273 nm $^1O_2$ phosphorescence vibronic peak ($^1\Delta_g$(v'=0) $\rightarrow {}^3\Sigma_g^-$(v =0)) with that generated by a well-known $^1O_2$ sensitizer such as tetraphenylporphyrin, for which Φ_Δ was reported to be 0.60 in perdeuterated benzene (C_6D_6) with one-photon excitation at 590 nm.[29] The use of C_6D_6 was to reduce $^1O_2$ emission quenching from the electronic-vibrational (C-H) energy transfer.[30] Figure 2-6a shows $^1O_2$ emission generated by n**S-PDI**s and the standard tetraphenylporphyrin in C_6D_6 under identical condition. As a result, Φ_Δ of **1S-PDI-D**, **2S-*cis*-PDI-D**, **2S-*trans*-PDI-D**, **3S-PDI-D** and **4S-PDI-D** were calculated to be 1.00, 0.39, 0.55, 0.00 and 0.00, respectively. The drastically different $^1O_2$ yield might not be surprising, as the energy

doi:10.6342/NTU202201631

levels of the lowest triplet state of n**S-PDI-D**s were calculated to be 1.10 eV, 0.98 eV, 0.98 eV, 0.87 eV and 0.77 eV for **1S-PDI-D**, **2S *cis*-PDI-D**, **2S-*trans*-PDI-D**, **3S-PDI-D** and **4S-PDI-D**, respectively (Table 2-1). In theory, the lowest triple state energy of the photosensitizers must be higher than that of $^1O_2$ (0.97 eV) for a thermally allowed energy-transfer process shown in Figure 2-6b. These results surmised that **1S-PDI-D** could be an efficient PS, while $^1O_2$ generation from the triplet state of **3S-PDI-D** and **4S-PDI-D** was energetically forbidden. The < 100% $^1O_2$ generation for **2S-*cis*-PDI-D** and **2S-*trans*-PDI-D** were mainly due to its proximal energy (0.98 eV) with that of $^1O_2$ (0.97 eV); therefore, loss from the equilibrium type energy transfer was expected. The difference in $^1O_2$ efficiency between **2S-*cis*-PDI-D** and **2S-*trans*-PDI-D** may be due to the geometrical factor in forming the collisional complex statistically while actual mechanism was pending.

In summary, Figure 2-6b depicted an overall energy diagram of excited-state relaxation and O_2 sensitization for n**S-PDI-D**s. Upon an allowed $S_0 \rightarrow S_2$ ($\pi\pi^*$) allowed transition, followed by ultrafast rate of $S_2 \rightarrow S_1$ internal conversion, the S_1 ($n\pi^*$) $\rightarrow T_1$ ($\pi\pi^*$) rate of ISC then took place. The > 10^{12} s^{-1} ISC (vide supra), together with the small radiative lifetime for the optically forbidden S_1 ($n\pi^*$) state, resulting in ~100% population in the T_1 ($\pi\pi^*$) state. While **1S-PDI-D** could effectively generated singlet molecular oxygen, negligible $^1O_2$ production was observed in **3S-PDI-D** and **4S-PDI-D** (see Figure 2-6b) due to its thermally unfavorable energy transfer process

The highly π-conjugated properties for n**S-PDI-D**s and the cruciality for penetration depth of $^1O_2$ associated photodynamic therapy (PDT) further encouraged us to carry out two-photon absorption cross sections (σ) measurement for n**S-PDI**s by the Z-scan method at selected wavelengths of 1150 to 1400 nm. As a result, σ was determined to be 976, 812, 866, 851, and 872 GM for n = 1, 2, 3 and 4 n**S-PDI-D**s, respectively, at 1400 nm in

doi:10.6342/NTU202201631

toluene (Table 2-1 and Figure S2-20). The results indicated that n**S-PDI-D**s acted as a good two-photon absorber in the near-infrared range, suitable for further bio-imaging applications elaborated below.

2.2.4 Synthesis Methods

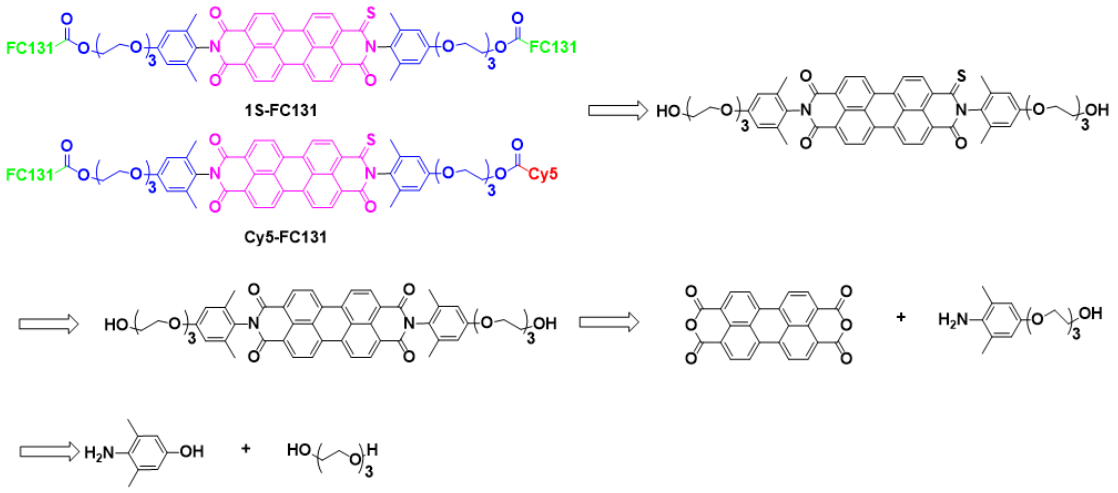

Figure 2- 7 Retrosynthesis of **1S-FC131** and **Cy5-1S-FC131**

In order to synthesize our target compound **1S-FC131** and **Cy5-1S-FC131**, we needed to plan the retrosynthesis in Figure 2-7. **1S-FC131** and **Cy5-1S-FC131**, a perylene diimide backbone, could be coupled with peptide FC131 or Cy5-NH_2 in the latest step. Perylene diimide with active end, hydroxyl group, could link to FC131 via nucleophilic substitution with proper leaving group. The replacement from carbonyl to thiol-carbonyl could simply conduct Lawesson's reaction. Since mono-thiol-substituted compounds were apt to decompose in the room temperature, this step needed to arrange in the late part as possible. Perylene diimide moiety could consist of commercially available perylene tetracarboxylic dianhydride and 1^o amine linker. 1^o amine linker could comprise commercially available 3,5-dimethyl-4-aminophenol and triethylene glycol via nucleophilic substitution. In order to facilitate the couple of these two moieties,

doi:10.6342/NTU202201631

triethylene glycol needed to be tosylated first. The retrosynthesis of **1S-FC131** and **Cy5-1S-FC131** have been complete.

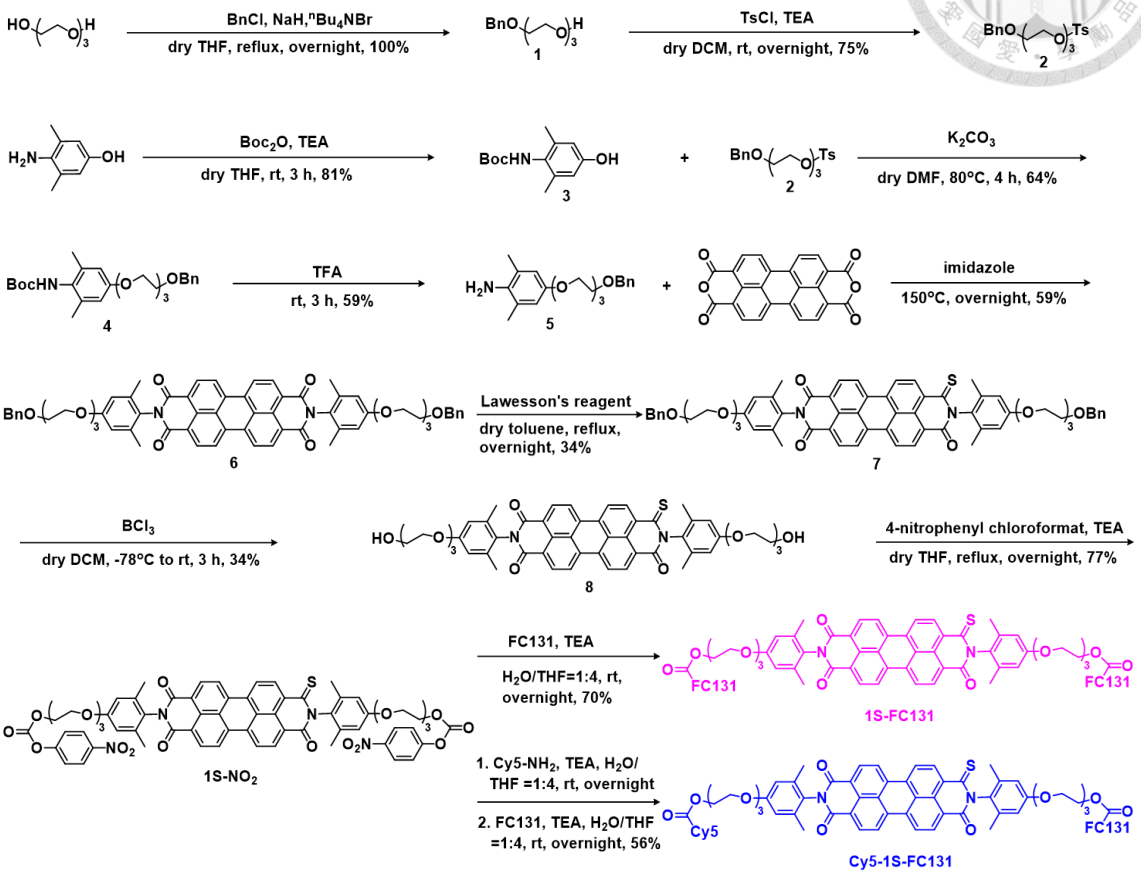

Figure 2- 8 Synthesis of **1S-FC131** and **Cy5-1S-FC131**

The synthetic route for **1S-FC131** and **Cy5-1S-FC131** was depicted in Figure 2-8. Detailed synthesis procedures and characterizations regarding ^{1}H NMR and ^{13}C NMR, FTIR, HRMS were elaborated in the Supporting information S2-1 to S2-19. In brief, shown in Figure 2-8, mono-protection of triethylene glycol followed by tosylation yielded **2**. **2** was reacted with Boc-protected of 3, 5-dimethyl-4-aminophenol in the presence of K_2CO_3 in DMF to afford **4** via the nucleophilic substitution reaction. **6** was obtained by coupling of 3, 4, 9, 10-perylenetetracarboxylic dianhydride and **5**, followed by the removal of Boc-protection in trifluoroacetic acid. Preparation of mono-sulfur substituted **7** was from **6** treated with Lawesson's reagent. Deprotection of benzyl group from **7** by BCl_3 to yield **8** had higher reactivity than hydrogenation via Pd/C catalysis. To facilitate

doi:10.6342/NTU202201631

coupling 8 with FC131 and Cy5 dye, a good leaving group, 4-nitrophenyl chloroformate, was installed to afford **1S-NO$_2$** prior to the conjugation. **1S-NO$_2$** was coupling with 2 equiv. FC131 to afford **1S-FC131.** On the other hand, **1S-NO$_2$** was coupling with Cy5-NH_2 first, and then reacted with 1 equiv.FC131 to afford the final product, **Cy5-1S-FC131**.

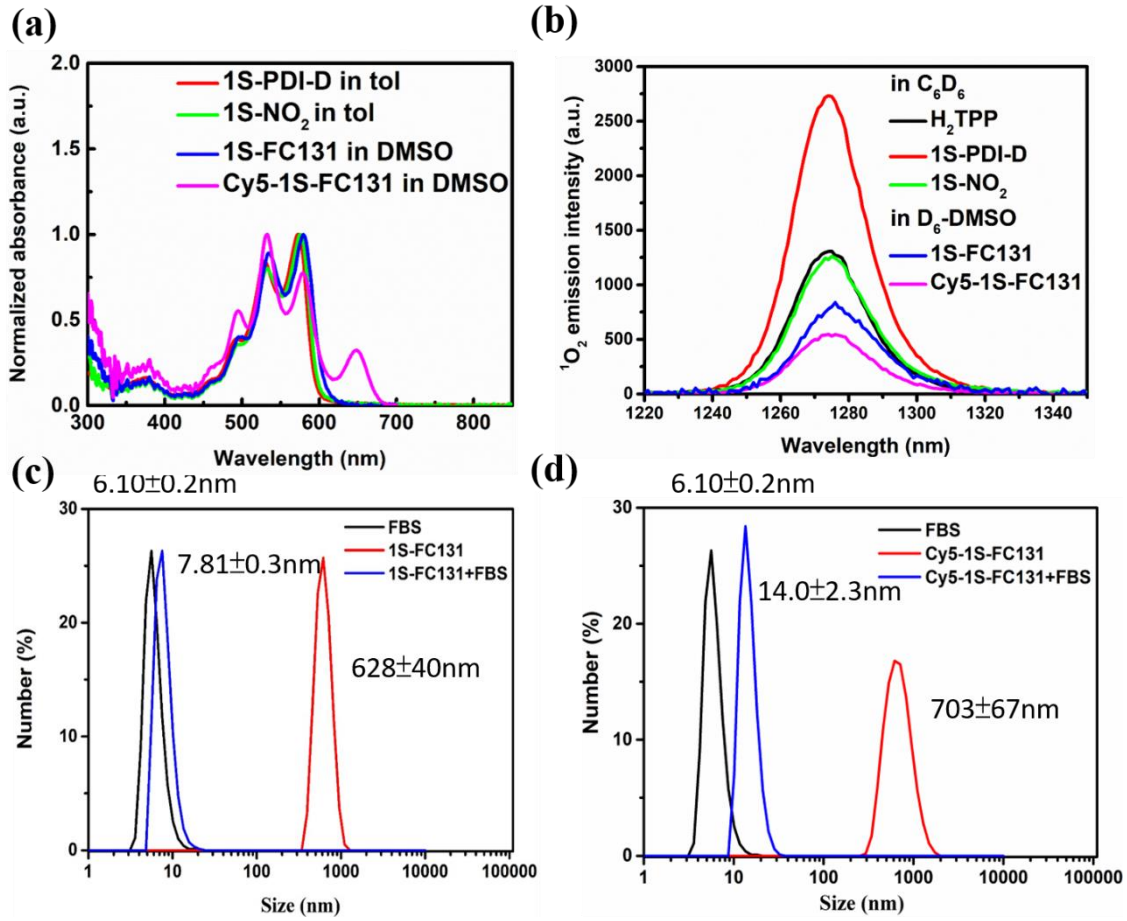

Figure 2- 9 (a)Absorbance spectrum of **1S-PDI-D** and **1S-NO$_2$** in toluene and **1S-FC131** and **Cy5-1S-FC131** in DMSO (b) $^1O_2$ emission spectrum of **1S-PDI-D** and **1S-NO$_2$** in deuterated benzene and **1S-FC131** and **Cy5-1S-FC131** in deuterated DMSO (c) Size distributions of **1S-FC131** (8 μM) in DMSO or PBS buffer detected by DLS.(d) Size distribution of **Cy5-1S-FC131** (24 μM) in water before and after FBS protein (1/5 volume ratio) by DLS.

doi:10.6342/NTU202201631

The absorption spectral profiles for **1S-FC131** and **Cy5-1S-FC131** and reference compound **1S-NO_2** and **1S-PDI-D** were shown in Figure 2-9a. The structural peak of **1S-FC131** and **Cy5-1S-FC131** was almost similar with **1S-NO_2** and **1S-PDI-D**. A peak at 648 nm of **Cy5-1S-FC131** was belong to cyanine 5 dye. On the other hand, the singlet oxygen production yield Φ_Δ of **1S-PDI-D, 1S-NO_2**, **1S-FC131** and **Cy5-1S-FC131** were determined to be 0.99, 0.60, 0.26 and 0.14, respectively in Figure 2-9b and Table 2-3. The decrease of Φ_Δ plausibly arose from the sterically hindered long side chains that caused invalid collision with molecular oxygen statistically. Therefore, the longer side chain molecules were (**Cy5-1S-FC131** > **1S-FC131** > **1S-NO_2** > **1S-PDI-D**), the lower Φ_Δ molecules were. (**Cy5-1S-FC131 < 1S-FC131** < **1S-NO_2 < 1S-PDI-D**). To explore the morphology of **1S-FC131** in different environment, we then studied its aggregation effect in PBS buffer by Dynamic Light Scattering (DLS). As depicted in Figure 2-9c, the size of **1S-FC131** in PBS buffer were measured to have an average molecular size of 628±40 nm. When we added FBS protein (a material of cell culture) in PBS buffer, disaggregation would happen that particle reduced to 7.81±0.3 nm. Identically, in Figure 2-9d, the same phenomenon would also be observed in **Cy5-1S-FC131** whose particles were 703±67 nm and 14.0±2.3 nm before and after addition of FBS protein in PBS buffer. These results meant that FBS protein could disassemble the particle, which could help our drugs, **1S-FC131** and **Cy5-1S-FC131,** easily enter the cell.

doi:10.6342/NTU202201631

Table 2- 3 Photophysical data of **1S-PDI**, **1S-NO$_2$**, **1S-FC131** and **Cy5-1S-FC131.**

PSs	λ_{abs} (nm)	Φ_{Δ}
1S-PDI	494, 529, 572	0.99
1S-NO$_2$	497, 533, 575	0.60
1S-FC131	500, 534, 580	0.26
Cy5-1S-FC131	495, 532, 579, 648	0.14

doi:10.6342/NTU202201631

2.2.5 Cell Viability and Cell Apoptosis

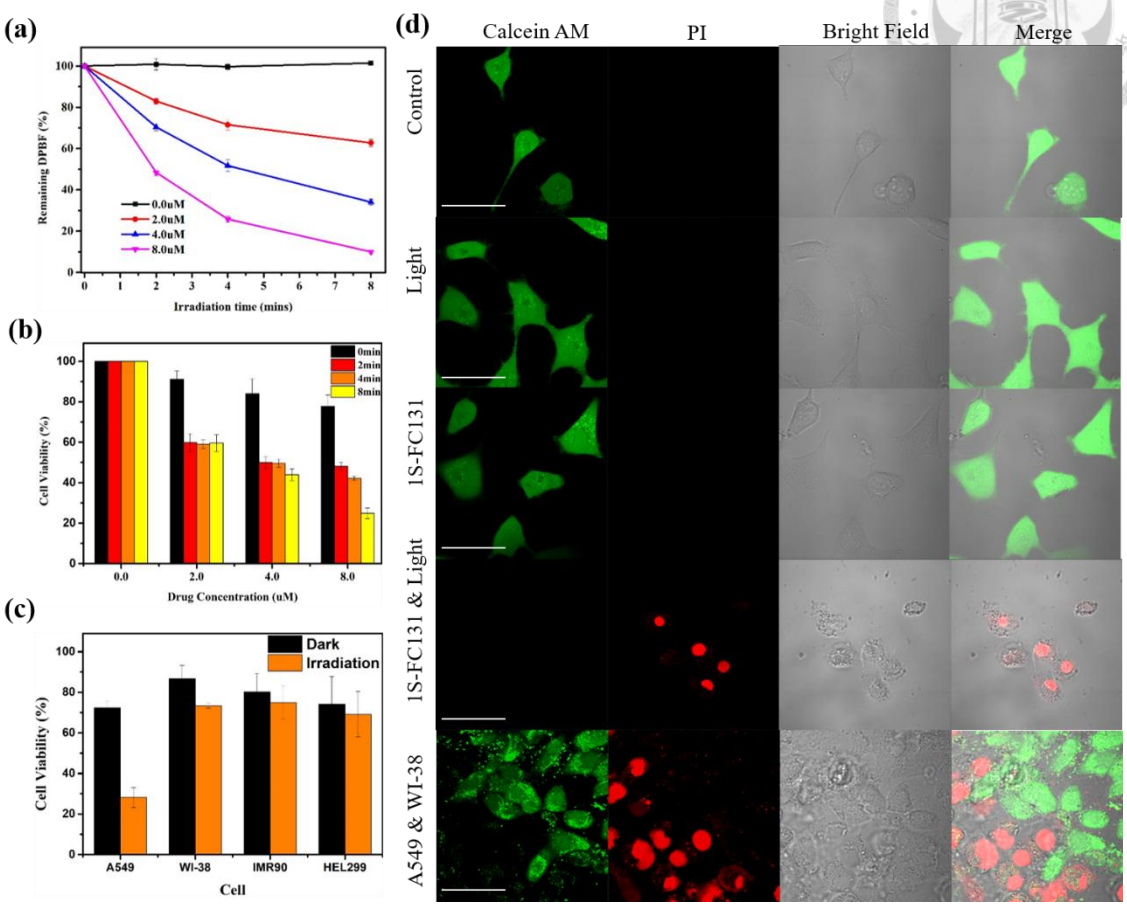

Figure 2- 10 (a)Change of DPBF at 415nm under different concentration of **1S-FC131** and irradiation time (b)Cell viability of A549 cell after treatment with 8 μM **1S-FC131**and irradiation in 8 minutes (c)Cell viability of different cell lines after treatment of 8μM **1S-FC131** and irradiation with 8 minutes (d) Confocal imaging of A549 cells stained with Calcein AM(2 μM) (500-530 nm) and PI (2 μM) (620-650 nm). (Scar bar:50 μm)

Based on the excellent photophysical properties of **1S-FC131**, we would like to further probe its potential as a PDT drug via in vitro test. Initially, we tested the $^1O_2$ yield of **1S-FC131** in dose-dependent and time-dependent manner by 1,3-diphenylisobenzofuran (DPBF: a $^1O_2$ indicator)[31] assay in PBS buffer. As shown in Figure 2-10a, the remaining DPBF% decreased linearly with the increasing irradiation time. Moreover, the decreasing

doi:10.6342/NTU202201631

degree was dose-dependent manner in the various concentrations. The lowest DPBF remaining point about 10% appeared at the condition of 8 μM **1S-FC131** and 8 minutes irradiation. In the DPBF assay, we could know that **1S-FC131** had sufficient $^1O_2$ production in 8 μM under 8 minutes irradiation. Following the DPBF results, the anticancer effect of **1S-FC131** was demonstrated by MTT assay in A549 cells. As shown in Figure 2-10b, the optimized condition in DPBF assay was used in the MTT assay. Different doses (0.0, 2.0, 4.0, 8.0 μM) of **1S-FC131** were incubated in A549 cells and treated with various irradiation times. The obvious photocytotoxicity and negligible dark toxicity could be observed in the Figure 2-10b. The cell viability of **1S-FC131** was 25 % in 8μM and 8 minutes irradiation. Compared to the half maximal inhibitory concentration (IC_{50}) of methylene blue (MB) (more than 10 μM),[28] **1S-PDI** possessed the superior PDT efficacy about 3.11 μM, 3-fold lower than that of MB. Moreover, the excellent PDT efficacy in A549 cells meant that the nanoparticle of **1S-FC131** could efficiently bind on cell surface due to high affinity of our specific peptide in the physiological environment. To assess the selectivity of **1S-FC131**, three normal human lung cell lines were chosen: WI-38, IMR90 and HEL299 cells. In Figure 2-10c, in contrast to the ignorable change of cell viability on the normal cell lines with or without irradiation, we observed that A549 cells had significantly decrease of cell viability from 72% (dark) to 28% (irradiation) by incubation of **1S-FC131** (8 μM), indicating that **1S-FC131** was indeed able to selectively bind on the A549 cells due to the high affinity between FC131 moiety and CXCR4 in cancer cells as our design. As last, the photocytotoxicity of **1S-FC131** toward A549 cells was proved in cell apoptosis experiment by confocal imaging microscopy. In this experiment, Calcein AM (2 μM) and Propidium Iodide (PI) (2 μM) were applied to label live and death cells, respectively. As depicted in Figure 2-10d, A549 cells with the incubation of 8 μM **1S-FC131** under 8 minutes irradiation displayed strong red

doi:10.6342/NTU202201631

fluorescence, suggesting that A549 cells were mostly apoptosis. In contrast, other three conditions: control (A549 cells without treatment), A549 cells treated with only light or only **1S-FC131** showed strong green fluorescence, indicating that A549 cells were intact. In the last group, cancer cells (A549) and normal cells (WI-38) were co-cultured in the same dish with the 8μM **1S-FC131** under 8mins irradiation. The obvious boundary could be found in the merge field, indicating that our drug could selectively poison the cancer cells. Through these experiments, we could finally conclude that **1S-FC131** not only had significant photocytotoxicity after photoactivation but also selectively bound on the cancer cells.

doi:10.6342/NTU202201631

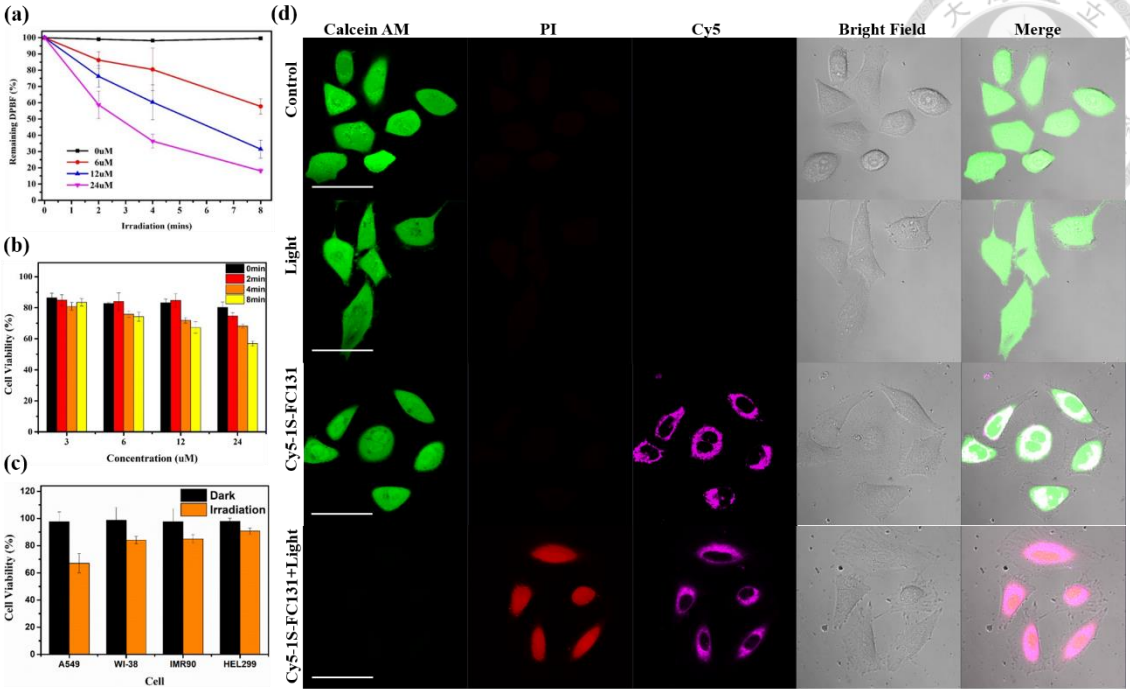

Figure 2- 11 (a)Changes of DPBF at 415 nm under different concentration of **Cy5-1S-FC131** and irradiation time (λ_{ex}: 590 nm). (b)Cell viability of A549 cell after 24-hr treatment with 24 μM **Cy5-1S-FC131** and irradiation for 8 minutes. (c)Cell viability of different cell lines after 24-hr treatment of 24 μM **Cy5-1S-FC131** and irradiation for 8 minutes.(d)Confocal imaging of A549 cells stained with Calcein AM (2 μM) (500-530 nm), PI (2 μM) (620-650 nm) and Cy5 (650-700nm)(scale bar: 50 μm).

Similiar *in vitro* experiments of **Cy5-1S-FC131** were conducted and presented in Figure 2-11a-d. In the DPBF test, remaining DPBF reached 18% under 24 μM with 8mins irradiation in Figure 2-11a. In the MTT assay, the cell viability was 57% under 24 μM with 8mins irradiation in Figure 2-11b. The higher dose or longer irradiaiton could not increase the PDT effect, which was harmony with lower singlet oxygen quantum yield of **Cy5-1S-FC131** than that of **1S-FC131**. In the selective experiment, there were not obvious difference between A549 and other normal cells in Figure 2-11c. In the confocal microscopy results, the four conditions (Control, Light, **Cy5-1S-FC131** and **Cy5-FC131**+Light) were separated in Figure 2-11d. Only **Cy5-1S-FC131**+Light condition

doi:10.6342/NTU202201631

showed the signal of death cells, and moreover, both **Cy5-1S-FC131** and **Cy5-1S-FC131**+Light condition presented the Cy5 fluorescence, meaning that **Cy5-1S-FC131** could successfuly enter and be trackable *in vitro*. In addition, it was worth mentioning that no obvious fluorescence in Figure S2-22 was observed in **1S-FC131** or **Cy5-1S-FC131**-treated A549 cell groups, which subsequently underwent irradiation treatments and assays with DCFDA, an ROS indicator that was more sensitive on hydroxyl radical (•OH) and peroxynitrite (ONOO-) than singlet oxygen.[32] The results suggested singlet oxygen to be the major species of ROS induced by our drugs. Compared **1S-FC131** with **Cy5-1S-FC131**, **1S-FC131** had superior PDT and selectivity but **Cy5-1S-FC131** had modest PDT and outstanding imaging ability.

doi:10.6342/NTU202201631

2.2.6 *In Vivo* Antitumor Effect

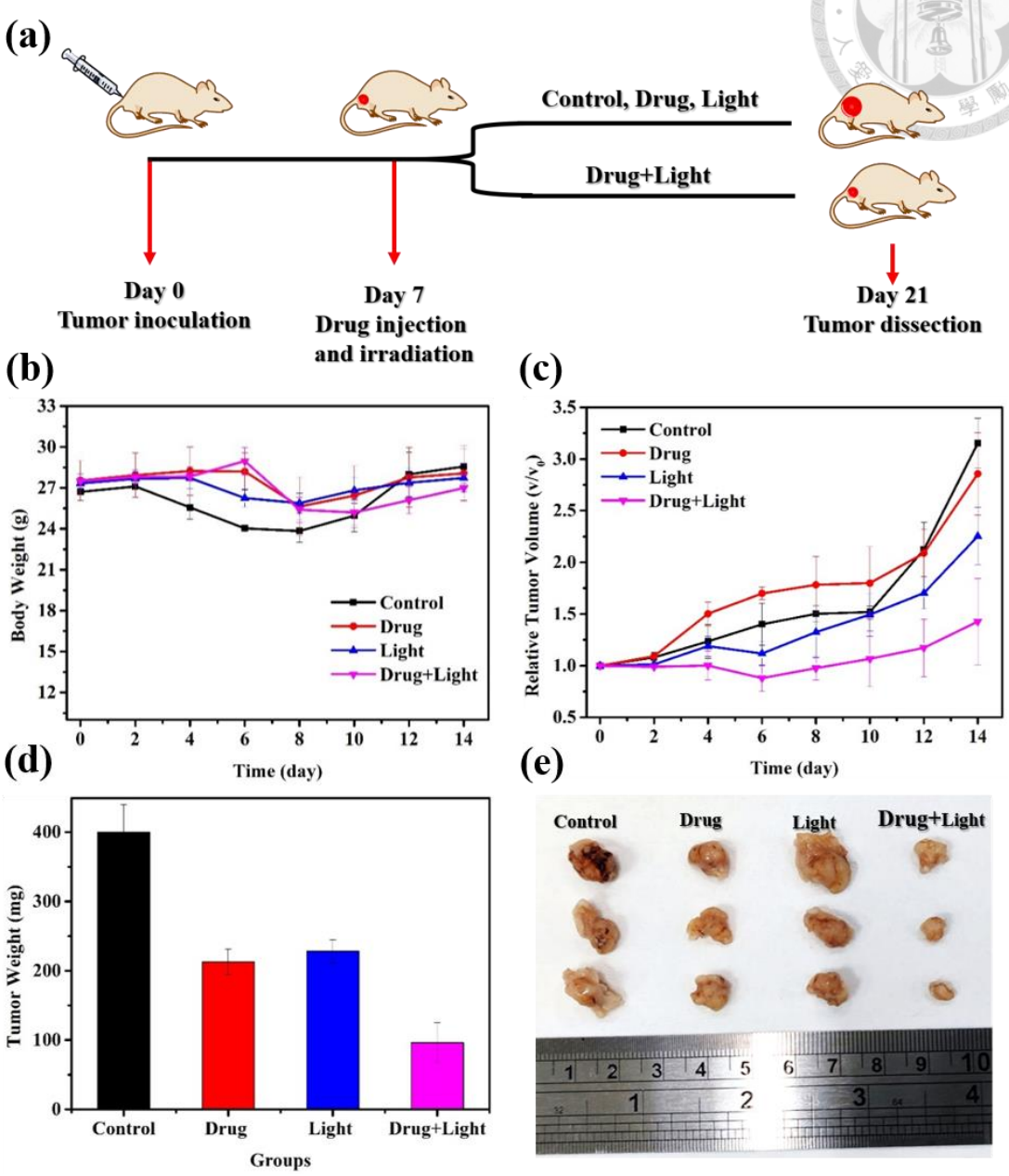

Figure 2- 12 (a) Schematic of experimental design to examine *in vivo* effectiveness of **1S-FC131** on the tumor shrinkage. (b) Body weight curves of 4 groups in 14 days after PDT treatment. (c) Curves for relative size of tumor in tumor-bearing mice of four groups in 14 days after PDT treatment. (d) Tumor weight of 4 groups removed from the sacrificed mice at the study endpoint day. (e) Tumors of 4 groups removed from the scarified mice at the study endpoint, day 14 (14 days after PDT treatment).

doi:10.6342/NTU202201631

Encouraged by the excellent anticancer effect of **1S-FC131** *in vitro*, *in vivo* experiments of **1S-FC131** were subsequently conducted to prove its practical antitumor performance. In this study, the PDT treatment was conducted on NU/NU male mice (4 weeks old) and shown in Figure 2-12a. Xenograft models were developed via subcutaneous injection of A549 cells in the back of mice. After tumor inoculation for 7 days, mice were separated into four groups (3 mice in each group): mice with PBS buffer (Control), mice with **1S-FC131** (100 μl, 2 $mgml^{-1}$) injection (Drug), mice with irradiation (λ_{ex}: 590 nm) in 20 mins (Light) and mice with **1S-FC131** (100 μl, 2 $mgml^{-1}$) injection and then irradiation in 20 mins (Drug + Light). A549 tumor-bearing nude mice were operated with corresponding treatment and then recorded their daily variety of their body weight and tumor volume in 14 days (see Figure 2-12b and 2-12c). As shown in Figure 2-12b, there were no obvious body weight loss in all four groups after treatment. In Figure 2-12c, Control, Drug and Light groups exhibited significant tumor growth over 2-3 times, while mice in Drug + Light groups presented no apparent tumor growth (lower than 1.3 times). The results clearly indicated that this treatment could successfully suppressed the tumor growth. Furthermore, the same results could also be supported by tumor weight and appearance after tumor dissection in Figure 2-12d and 2-12e. After PDT treatment for 14 days, tumor weight and appearance in Drug + Light groups kept lower tumor weight and smaller tumor size than that in other three groups, suggesting that **1S-FC131** after photoexcitation possessed remarkable PDT efficacy *in vitro* and *in vivo* experiments.

doi:10.6342/NTU202201631

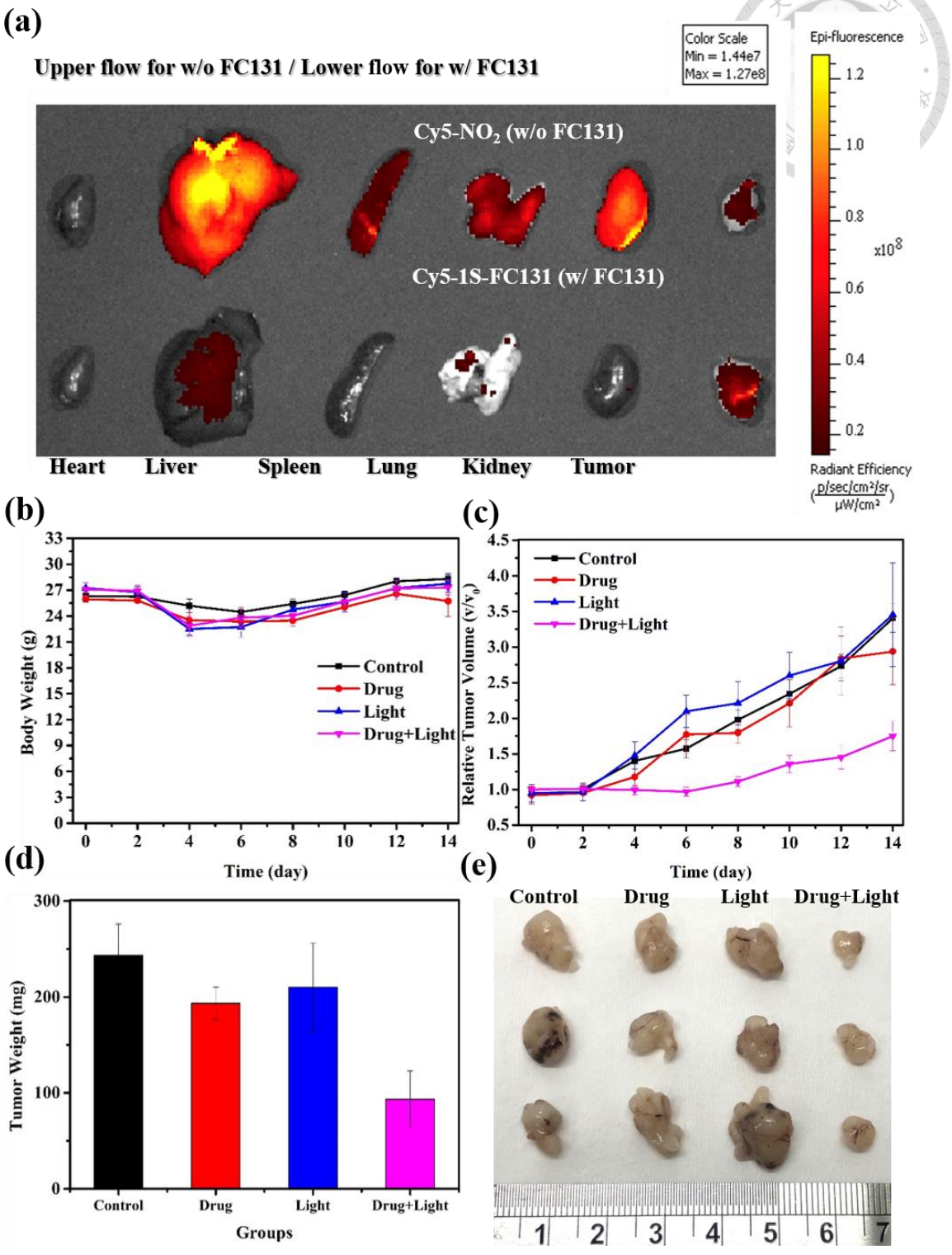

Figure 2- 13 (a)IVIS spectrum of **Cy5-1S-FC131** results after 14 days. (b)Body weight curves of 4 groups. (c)Curves for relative size of tumor in tumor-bearing mice of four groups. (d)Tumor weight of 4 groups removed from the sacrificed mice at 14th day. (e)Tumors appearance of 4 groups removed from the sacrificed mice at 14th day.

doi:10.6342/NTU202201631

On the other hand, *in vivo* tests of **Cy5-1S-FC131** were conducted under the same procedure in Figure 2-13. In Figure 2-13a, *in vivo* imaging system (IVIS) have measured the ability of targeting of **Cy5-1S-FC131**. Upper flow for **Cy5-NO_2** without FC131 moiety and lower flow for **Cy5-1S-FC131.** The organ were taken out after drug S-administration (6 hrs) including heart, liver, spleen, lung, kidney and A549 tumor. It was found that there were most of organs with Cy5 signals in upper flows and there were only liver and tumor with Cy5 signals in lower flow. These phenomenon proved that **Cy5-1S-FC131** had targeting and imaging ability on tumor in the same time. In Figure 2-13b, mice in four groups remained the stable body weight, suggesting that they kept relativly healthy during the treatment. In Figure 2-13c, the monitoring of tumor size every two days presented that tumors of **Cy5-1S-FC131**+Light group only grew from 1 to 1.7-fold during 14 days. After 14 days, mice have been sacrified and taken out their tumor. Their tumor weight and tumor status have reported in Figure 2-13d and 2-13e. Tumors in **Cy5-1S-FC131**+Light group were slighter and smaller than other three groups. Through *in vivo* experiments, the antitumor ability and imaging ability of **Cy5-1S-FC131** have been proved.

doi:10.6342/NTU202201631

2.3 Conclusion

In summary, we have developed a tailorable PDI by attachment of 2,6-dimethylphenyl amine on the imide position. Followed by treating the Lawesson's reagent, the synthetic route yielded a full class of thiol derived PDI, **nS-PDI-D**s **(n =1-4)**. n**S-PDI-D**s showed intriguing photophysical behavior where they all exhibited non-emissive properties due to the optical forbidden S_1 ($n\pi^*$) character and ultrafast S_1 ($n\pi^*$) → T_1 ($\pi\pi^*$) ISC. Among this class, **1S-PDI-D** showed 100% $^1O_2$ production due to efficient T_1 ($\pi\pi^*$) + $^3O_2 \rightarrow S_0 + {}^1O_2$ energy transfer and great two-photon absorption cross section. **1S-PDI-D** as a photosensitizer was further coupled with two targeting peptide FC131 as **1S-FC131** and one peptide and one Cy5 dye as **Cy5-1S-FC131**. **1S-FC131** presented its powerful and selective PDT capability *in vitro* and *in vivo*, where IC_{50} was three folds lower than that of clinical PDT methylene blue. On the other hand, **Cy5-1S-FC131** possessed modest selective PDT and imaging ability to track the position of drug in the cells and biodistribution in the mice. Conclusively, our *in vitro* and *in vivo* results confirmed that heavy metal free **1S-FC131** and **Cy5-1S-FC131** were selective PDT therapeutic materials with sufficient two-photon absorption and imaging capability. Particularly, **Cy5-1S-FC131** was an important breakthrough for current clinical PDT treatment, which was highly likely to gain credence in personalized and precision medicine.

2.4 Ethical Statement

All animals (4-5 weeks old nude mice) were obtained from National Laboratory Animal Center in Taiwan. The animal treatment followed the relevant laws and guidelines in National Taiwan University Institutional Animal Care and Use Committee. (NTU-110-EL-00069)

doi:10.6342/NTU202201631

2.5 Reference

[1] a)T. J. Dougherty, C. J. Gomer, B. W. Henderson, G. Jori, D. Kessel, M. Korbelik, J. Moan, Q. Peng, *J. Natl. Cancer Inst.* **1998**, *90*, 889-905; b)T. J. Dougherty, S. L. Marcus, *Eur. J. Cancer* **1992**, *28*, 1734-1742; c)D. E. Dolmans, D. Fukumura, R. K. Jain, *Nat. Rev. Cancer* **2003**, *3*, 380-387.

[2] a)L. B. Josefsen, R. W. Boyle, *Theranostics* **2012**, *2*, 916; b)W. Fan, P. Huang, X. Chen, *Chem. Soc. Rev.* **2016**, *45*, 6488-6519; c)A. P. Castano, P. Mroz, M. R. Hamblin, *Nat. Rev. Cancer* **2006**, *6*, 535-545; d)Á. Juarranz, P. Jaén, F. Sanz-Rodríguez, J. Cuevas, S. González, *Clin. Transl. Oncol.* **2008**, *10*, 148-154.

[3] X. Zhao, J. Liu, J. Fan, H. Chao, X. Peng, *Chem. Soc. Rev.* **2021**, *50*, 4185-4219.

[4] a)C. S. Foote, *Photochem. Photobiol.* **1991**, *54*, 659; b)B. Sauerwein, G. B. Schuster, *J. Phys. Chem.* **1991**, *95*, 1903-1906.

[5] a)Y. Cakmak, S. Kolemen, S. Duman, Y. Dede, Y. Dolen, B. Kilic, Z. Kostereli, L. T. Yildirim, A. L. Dogan, D. Guc, *Angew. Chem. Int. Ed.* **2011**, *50*, 11937-11941; b)J. R. Darwent, P. Douglas, A. Harriman, G. Porter, M.-C. Richoux, *Coord. Chem. Rev.;(Netherlands)* **1982**, *44*.

[6] N. J. Patel, Y. Chen, P. Joshi, P. Pera, H. Baumann, J. R. Missert, K. Ohkubo, S. Fukuzumi, R. R. Nani, M. J. Schnermann, *Bioconjugate Chem.* **2016**, *27*, 667-680.

[7] a)O. Fakayode, C. Kruger, S. Songca, H. Abrahamse, O. Oluwafemi, *Mater. Sci. Eng. C* **2018**, *92*, 737-744; b)O. J. Fakayode, S. P. Songca, O. S. Oluwafemi, *Mater. Lett.* **2017**, *199*, 37-40; c)M. Pollum, S. Jockusch, C. E. Crespo-Hernandez, *J. Am. Chem. Soc.* **2014**, *136*, 17930-17933.

[8] J. Tang, L. Wang, A. Loredo, C. Cole, H. Xiao, *Chem. Sci.* **2020**, *11*, 6701-6708.

[9] V.-N. Nguyen, S. Qi, S. Kim, N. Kwon, G. Kim, Y. Yim, S. Park, J. Yoon, *J. Am. Chem. Soc.* **2019**, *141*, 16243-16248.

doi:10.6342/NTU202201631

[10] Z. Liu, Y. Gao, X. Jin, Q. Deng, Z. Yin, S. Tong, W. Qing, Y. Huang, *J. Mater. Chem. B* **2020**, *8*, 5535-5544.

[11] a)C. Huang, S. Barlow, S. R. Marder, *J. Org. Chem.* **2011**, *76*, 2386-2407; b)F. Zhang, Y. Ma, Y. Chi, H. Yu, Y. Li, T. Jiang, X. Wei, J. Shi, *Sci. Rep.* **2018**, *8*, 1-11; c)G. Li, Y. Zhao, J. Li, J. Cao, J. Zhu, X. W. Sun, Q. Zhang, *J. Org. Chem.* **2015**, *80*, 196-203.

[12] a)K. Balakrishnan, A. Datar, T. Naddo, J. Huang, R. Oitker, M. Yen, J. Zhao, L. Zang, *J. Am. Chem. Soc.* **2006**, *128*, 7390-7398; b)H. Dinçalp, Z. Aşkar, C. Zafer, S. İçli, *Dyes Pigm.* **2011**, *91*, 182-191.

[13] a)P. Singh, L. S. Mittal, V. Vanita, K. Kumar, A. Walia, G. Bhargava, S. Kumar, *J. Mater. Chem. B* **2016**, *4*, 3750-3759; b)N. I. Georgiev, A. R. Sakr, V. B. Bojinov, *Dyes Pigm.* **2011**, *91*, 332-339; c)X. Feng, Y. An, Z. Yao, C. Li, G. Shi, *ACS Appl. Mater. Interfaces* **2012**, *4*, 614-618.

[14] a)B. Muthuraj, S. Mukherjee, S. R. Chowdhury, C. R. Patra, P. K. Iyer, *Biosens. Bioelectron.* **2017**, *89*, 636-644; b)R. Roy, N. R. Sajeev, V. Sharma, A. L. Koner, *ACS Appl. Mater. Interfaces* **2019**, *11*, 47207-47217.

[15] a)F. Yukruk, A. L. Dogan, H. Canpinar, D. Guc, E. U. Akkaya, *Org. Lett.* **2005**, *7*, 2885-2887; b)F. Deng, J. R. Sommer, M. Myahkostupov, K. S. Schanze, F. N. Castellano, *Chem. Commun.* **2013**, *49*, 7406-7408.

[16] Z. Zheng, H. Liu, S. Zhai, H. Zhang, G. Shan, R. T. Kwok, C. Ma, H. H. Sung, I. D. Williams, J. W. Lam, *Chem. Sci.* **2020**, *11*, 2494-2503.

[17] J. Bhawalkar, N. Kumar, C.-F. Zhao, P. Prasad, *J. Clin. Laser. Med. Surg.* **1997**, *15*, 201-204.

[18] a)Q. Zang, J. Yu, W. Yu, J. Qian, R. Hu, B. Z. Tang, *Chem. Sci.* **2018**, *9*, 5165-5171; b)Y. Yuan, G. Feng, W. Qin, B. Z. Tang, B. Liu, *Chem. Commun.* **2014**, *50*,

doi:10.6342/NTU202201631

8757-8760; c)J. P. Celli, B. Q. Spring, I. Rizvi, C. L. Evans, K. S. Samkoe, S. Verma, B. W. Pogue, T. Hasan, *Chem. Rev.* **2010**, *110*, 2795-2838.

[19] T. Zhang, R. Lan, C.-F. Chan, G.-L. Law, W.-K. Wong, K.-L. Wong, *Proc. Natl. Acad. Sci. U.S.A.* **2014**, *111*, E5492-E5497.

[20] A. J. Tilley, R. D. Pensack, T. S. Lee, B. Djukic, G. D. Scholes, D. S. Seferos, *J. Phys. Chem. C* **2014**, *118*, 9996-10004.

[21] a)S. Thiele, J. Mungalpara, A. Steen, M. M. Rosenkilde, J. Våbenø, *Br. J. Pharmacol.* **2014**, *171*, 5313-5329; b)H. Tamamura, K. Hiramatsu, S. Ueda, Z. Wang, S. Kusano, S. Terakubo, J. O. Trent, S. C. Peiper, N. Yamamoto, H. Nakashima, *J. Med. Chem.* **2005**, *48*, 380-391; c)Y. Yoshikawa, K. Kobayashi, S. Oishi, N. Fujii, T. Furuya, *Bioorg. Med. Chem. Lett.* **2012**, *22*, 2146-2150; d)K. Kobayashi, S. Oishi, R. Hayashi, K. Tomita, T. Kubo, N. Tanahara, H. Ohno, Y. Yoshikawa, T. Furuya, M. Hoshino, *J. Med. Chem.* **2012**, *55*, 2746-2757.

[22] a)M. Jung, J. Rho, Y. Kim, J. Jung, Y. Jin, Y.-G. Ko, J. Lee, S. Lee, J. Lee, M. Park, *Oncogene* **2013**, *32*, 209-221; b)M. C. Smith, K. E. Luker, J. R. Garbow, J. L. Prior, E. Jackson, D. Piwnica-Worms, G. D. Luker, *Cancer Res.* **2004**, *64*, 8604-8612; c)B. Furusato, J. S. Rhim, *Chemokine Receptors in Cancer* **2009**, 31-45.

[23] J.-P. Sun, A. D. Hendsbee, A. J. Dobson, G. C. Welch, I. G. Hill, *Org. Electron.* **2016**, *35*, 151-157.

[24] G. Klebe, F. Graser, E. Hädicke, J. Berndt, *Acta Crystallogr., Sect. B: Struct. Sci* **1989**, *45*, 69-77.

[25] a)T. Ozturk, E. Ertas, O. Mert, *Chem. Rev.* **2007**, *107*, 5210-5278; b)L. Legnani, L. Toma, P. Caramella, M. A. Chiacchio, S. Giofre, I. Delso, T. Tejero, P. Merino, *J. Org. Chem.* **2016**, *81*, 7733-7740.

doi:10.6342/NTU202201631

[26] M. El-Sayed, *J. Chem. Phys.* **1963**, *38*, 2834-2838.

[27] K. Schmidt, S. Brovelli, V. Coropceanu, D. Beljonne, J. Cornil, C. Bazzini, T. Caronna, R. Tubino, F. Meinardi, Z. Shuai, *J. Phys. Chem.A* **2007**, *111*, 10490-10499.

[28] a)R. A. Marcus, N. Sutin, *Biochim. Biophys. Acta BBA - Rev. Bioenerg.* **1985**, *811*, 265-322; b)T. J. Penfold, E. Gindensperger, C. Daniel, C. M. Marian, *Chem. Rev.* **2018**, *118*, 6975-7025.

[29] a)R. Bonnett, D. McGarvey, A. Harriman, E. J. Land, T. Truscott, U. J. Winfield, *Photochem. Photobiol.* **1988**, *48*, 271-276; b)J. F. Lovell, T. W. Liu, J. Chen, G. Zheng, *Chem. Rev.* **2010**, *110*, 2839-2857; c)E. D. Sternberg, D. Dolphin, C. Brückner, *Tetrahedron* **1998**, *54*, 4151-4202.

[30] D. R. Kearns, *Chem. Rev.* **1971**, *71*, 395-427.

[31] M. Wozniak, F. Tanfani, E. Bertoli, G. Zolese, J. Antosiewicz, *Biochim. Biophys. Acta, Lipids Lipid Metab.* **1991**, *1082*, 94-100.

[32] a)P. Bilski, A. Belanger, C. Chignell, *Free Radical Biol. Med.* **2002**, *33*, 938-946; b)K.-i. Setsukinai, Y. Urano, K. Kakinuma, H. J. Majima, T. Nagano, *J. Biol. Chem.* **2003**, *278*, 3170-3175.

doi:10.6342/NTU202201631

2.6 Supporting Information

2.6.1 Synthetic Procedure

2.6.1.1 Materials and Methods

All reagents were commercially available from Acros, Sigma Aldrich, and Merck, which were used as supplied without further purification. Deuterated solvents were purchased from Cambridge Isotope Laboratory (Andover, MA). Column chromatography was carried out using silica gel from Merck (230-400 mesh). ^{1}H NMR, ^{13}C NMR spectra were recorded on a Varian Inova 400 MHz spectrometer. ^{1}H and ^{13}C NMR chemical shifts were reported relative to residual solvent signals. Mass spectra were recorded on a micrOTOF-Q 228888.10 183 mass spectrometer using electrospray ionization with Bruker microTOF-Q II. FTIR was recorded on Varian 640-IR spectrometer. Dynamic light scattering (DLS) was measured using a Nano-ZS (Malvern).Scanning electron microscopy (SEM) was detected by TM3000 (Hitachi). One-photon Laser was from MaiTai DeepSee (Spectrum-Physics)

doi:10.6342/NTU202201631

2.6.1.2 Synthesis of **PDI-P**

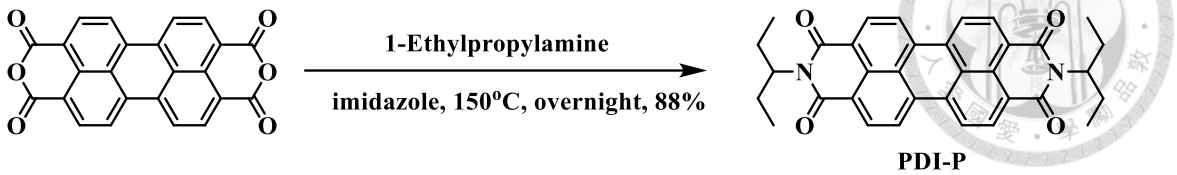

PDI-P

To the solution of 1-Ethylpropylamine (0.67 g, 7.65 mmole, 3.00 equiv.), 3,4,9,10-perylenetetracarboxylic dianhydride (1.00 g, 2.55 mmole, 1.00 equiv.) and imidazole (12.00 g, 176.25 mmole) was heated to 150℃ overnight. After completion of reaction, 1,4-dioxane was added. When the system was cooled down, the mixture concentrated by rotavapor. The crude product could be purified by silica column (pure dichloromethane, R_f = 0.70). The purified product **PDI-P** was red powder (1.19 g, 2.24 mmole, 88%). m.p. = over 400°C, FT-IR (cm^{-1}):2963, 2931, 2876, 1700, 1656, 1589, 1330, 1239, 810, 774, 750. ^{1}H NMR (400 MHz, $CDCl_3$) δ 8.59 (dd, *J* = 8.0 Hz, 8H), 5.20 – 4.96 (m, 2H), 2.40 – 2.12 (m, 4H), 2.00 – 1.85 (m, 4H), 0.93 (t, *J* = 7.5 Hz, 12H). ^{13}C NMR (101 MHz, $CDCl_3$) δ 164.2, 134.4, 131.4, 129.5, 126.3, 123.5, 122.9, 57.7, 25.0, 11.4. HRMS (ESI-TOF) m/z: $[M+H]^+$ Calc'd for $C_{40}H_{27}N_2O_4$ [531.2206]; Found 531.2206.

doi:10.6342/NTU202201631

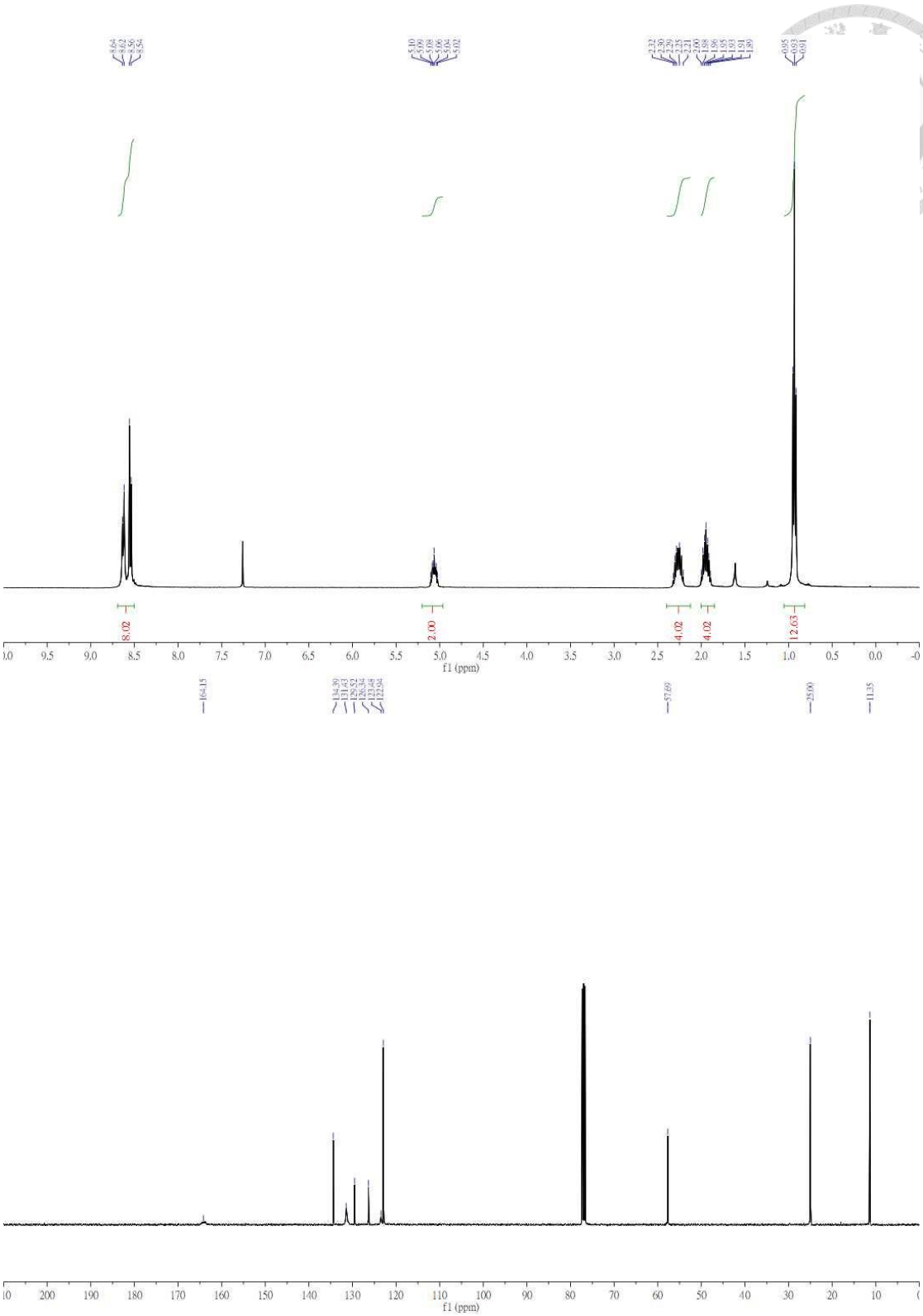

Figure S2-1. ^{1}H & ^{13}C-NMR of **PDI-P**

doi:10.6342/NTU202201631

2.6.1.3 Synthesis of **1S-PDI-P, 2S-*cis*-PDI-P, 2S-*trans*-PDI-P**

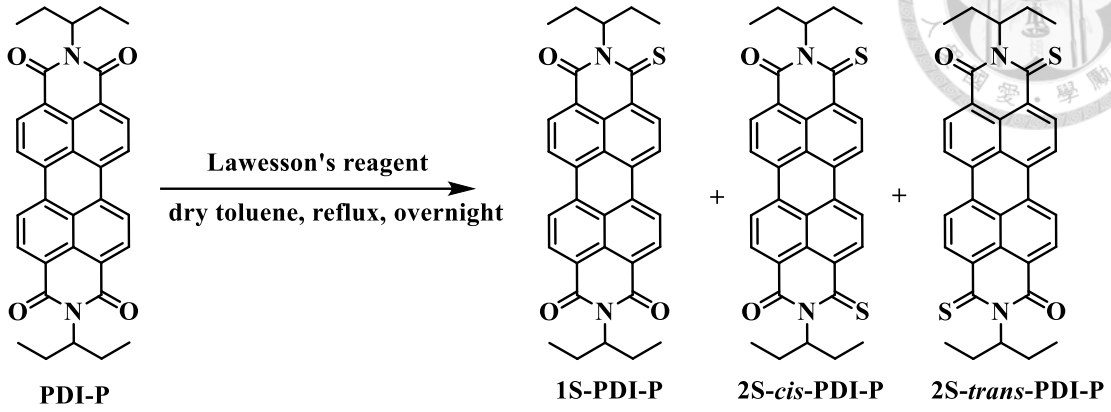

To the solution of **PDI-P** (0.3000 g, 0.5660 mmole, 1.00 equiv.), Lawesson's reagent (1.3740 g, 3.3960 mmole, 6.00 equiv.) in the dry toluene (40 ml) was heated to reflux overnight. After completion of reaction, the reactant was extracted with ethyl acetate and brine. The organic layer was separated, dried over $MgSO_4$ and concentrated by rotavapor. The crude product could be purified by gradient silica column (pure toluene). The pure product **1S-PDI-P** (0.1132 mmole, 0.0619 g, 20%)**, 2S-*cis*-PDI-P** (0.1698 mmole, 0.0956 g, 30%)**, 2S-*trans*-PDI-P** (0.19811 mmole, 0.1115 g, 35%)**.**

1S-PDI-P: FT-IR (cm^{-1}): 2970, 2935, 2883, 1700, 1652, 1589, 1322, 1231, 818, 786.^{1}H NMR (400 MHz, $CDCl_3$) δ 8.88 (d, *J* = 8.3 Hz, 1H), 8.62 – 8.48 (m, 3H), 8.46 – 8.32 (m, 3H), 8.24 (d, *J* = 8.4 Hz, 1H), 6.31 – 6.18 (m, 1H), 5.07 (dd, *J* = 9.5, 6.0 Hz, 1H), 2.39 – 2.20 (m, 4H), 2.11 – 1.92 (m, 4H), 0.96 (d, *J* = 7.4 Hz, 12H).^{13}C NMR (101 MHz, $CDCl_3$) δ 196.1, 160.5, 137., 134.2, 133.8, 133.1, 131.4, 129.4, 127.8, 127.3, 125.9, 124.1, 123.0, 122.9, 122.7, 65.5, 57.7, 25.3, 25.0, 11.4, 11.3. HRMS (ESI-TOF) m/z: $[M+H]^+$ Calc'd for $C_{34}H_{31}N_2O_3S$ [547.1977]; Found 547.1977

doi:10.6342/NTU202201631

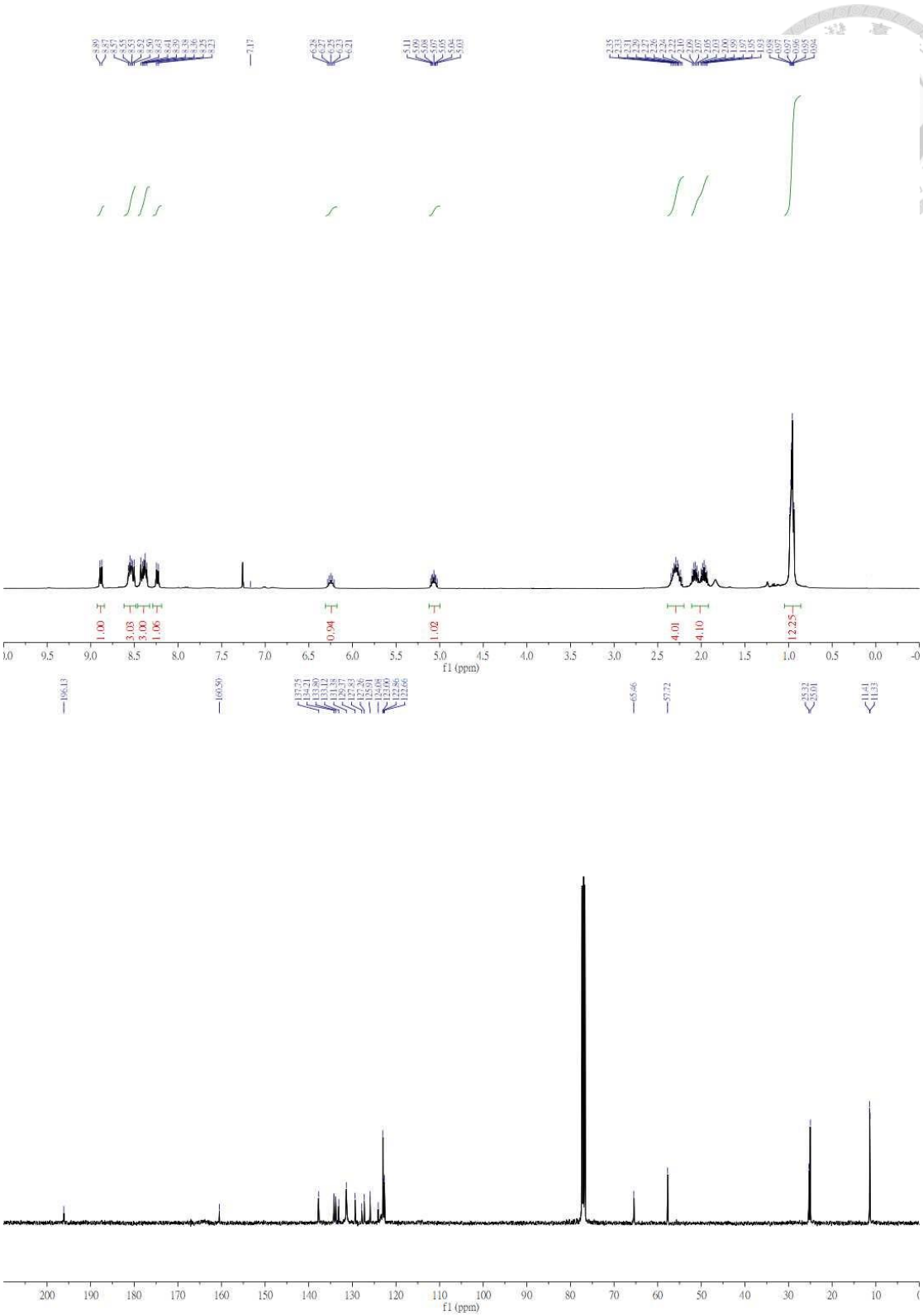

Figure S2-2. ^{1}H &^{13}C-NMR of **1S-PDI-P**

doi:10.6342/NTU202201631

2S-*cis*-PDI-P: FT-IR (cm^{-1}): 2967, 2931, 2868, 1700, 1660, 1593, 1314, 1243, 854, 810, 766.^{1}H NMR (400 MHz, $CDCl_3$) δ 8.95 (d, *J* = 8.4 Hz, 2H), 8.55 (d, *J* = 8.0 Hz, 2H), 8.45 (d, *J* = 8.1 Hz, 2H), 8.30 (d, *J* = 8.5 Hz, 2H), 6.33 – 6.17 (m, 2H), 2.35 – 2.26 (m, 4H), 2.05 (d, *J* = 6.9 Hz, 4H), 0.95 (t, *J* = 8.9 Hz, 12H).^{13}C NMR (101 MHz, $CDCl_3$) δ 196.2, 160.6, 138., 134.1, 133.3, 131.5, 127.9, 127.4, 125.9, 124.2, 123.3, 122.9, 65.5, 25.4, 11.3. HRMS (ESI-TOF) m/z: $[M+H]^+$ Calc'd for $C_{34}H_{31}N_2O_2S_2$ [563.1749]; Found 563.1749.

doi:10.6342/NTU202201631

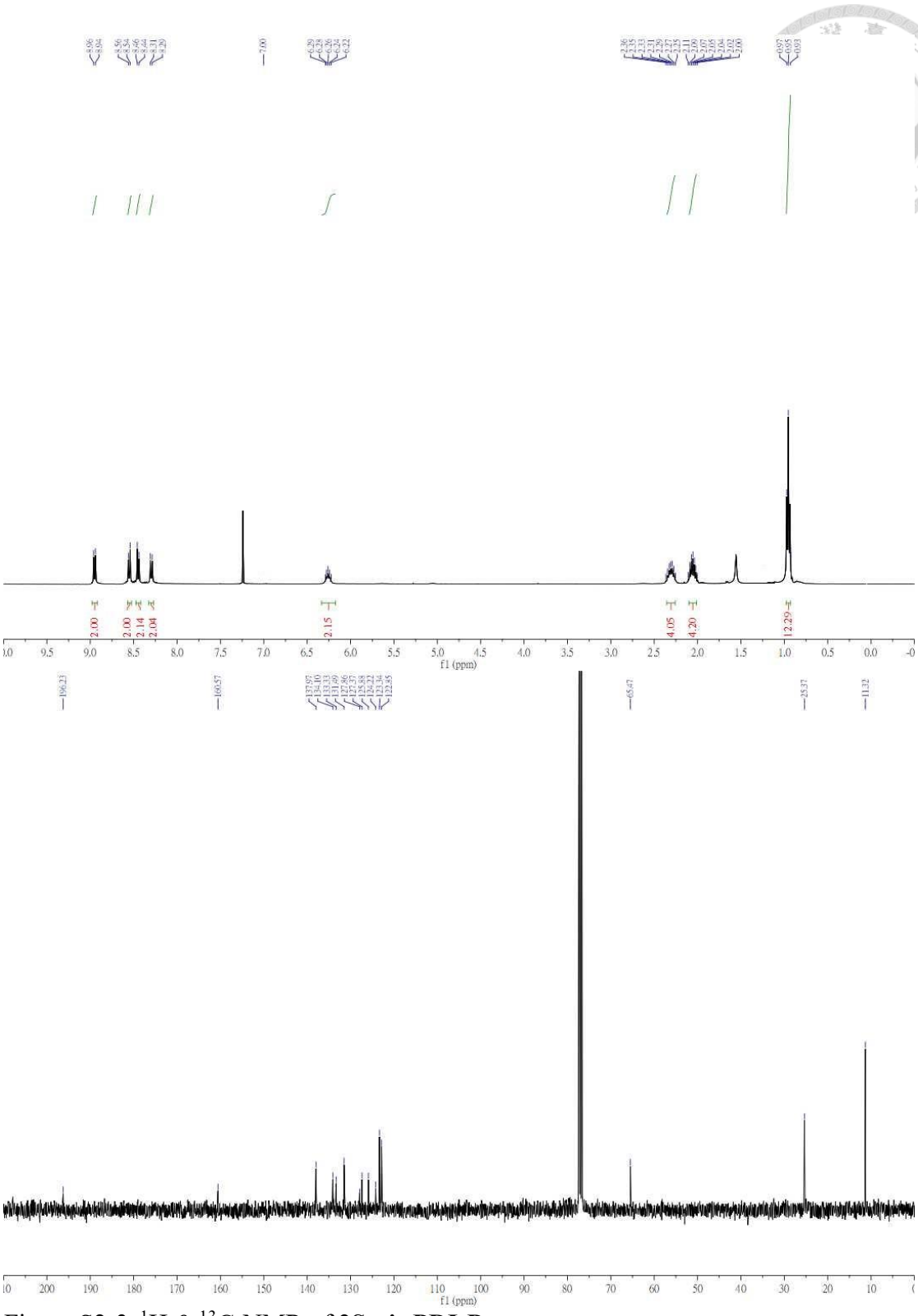

Figure S2-3. ^{1}H & ^{13}C-NMR of **2S-*cis*-PDI-P**

doi:10.6342/NTU202201631

2S-*trans*-PDI-P: FT-IR (cm^{-1}): 2967, 2943, 2864, 1692, 1668, 1318, 1223, 838, 778. ^{1}H NMR (400 MHz, $CDCl_3$) δ 9.06 (d, *J* = 8.6 Hz, 2H), 8.57 (d, *J* = 7.5 Hz, 4H), 8.09 (s, 2H), 6.35 – 6.26 (m, 2H), 2.36 – 2.27 (m, 4H), 2.09 – 2.01 (m, 4H), 0.96 (s, 12H). ^{13}C NMR (101 MHz, $CDCl_3$) δ 196.3, 160.7, 138.1, 134.3, 133.6, 131.7, 129.4, 128.0, 127.5, 126.1, 124.3, 123.3, 123.2, 65.4, 25.4, 11.3. HRMS (ESI-TOF) m/z: $[M+H]^+$ Calc'd for $C_{34}H_{31}N_2O_2S_2$ [563.1749]; Found 563.1749.

doi:10.6342/NTU202201631

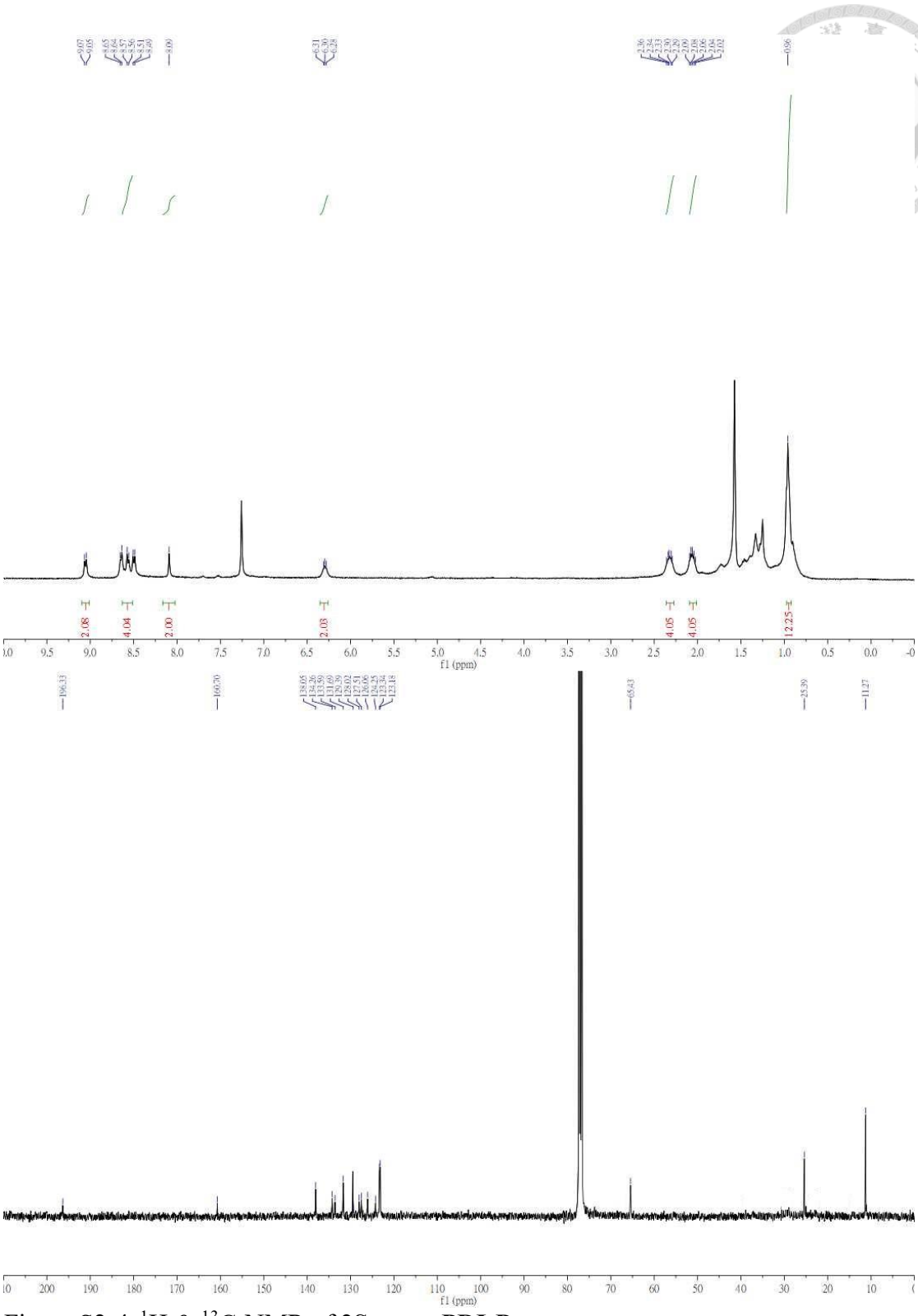

Figure S2-4. ^{1}H & ^{13}C-NMR of **2S-*trans*-PDI-P**

doi:10.6342/NTU202201631

2.6.1.4 Synthesis of **PDI-D**

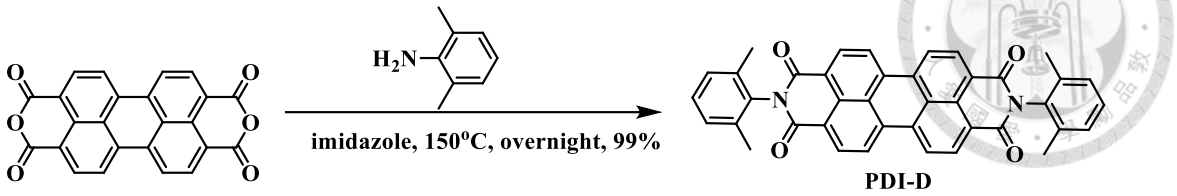

To the solution of 2,6-dimethylaniline (0.83 g, 6.85 mmole, 3.00 equiv.), 3,4,9,10-perylenetetracarboxylic dianhydride (0.90 g, 2.30 mmole, 1.00 equiv.) and imidazole (12.00 g, 176.25 mmole) was heated to 150℃ overnight. After completion of reaction, 1,4-dioxane was added. When the system was cooled down, the mixture concentrated by rotavapor. The crude product could be purified by silica column (pure dichloromethane, R_f = 0.7). The purified product **PDI-D** was red powder (1.13 g, 1.89 mmole, 82%). m.p. = over 400°C, FT-IR (cm^{-1}):2923, 2848, 1708, 1656, 1589, 1346, 1250, 817, 802. ^{1}H NMR (400 MHz, $CDCl_3$) δ 8.79 (d, *J* = 7.9 Hz, 4H), 8.73 (d, *J* = 8.1 Hz, 4H), 7.34 – 7.29 (m, 2H), 7.25 (d, *J* = 6.7 Hz, 4H), 2.19 (s, 12H).^{13}C NMR (101 MHz, $CDCl_3$) δ 162.7, 135.5, 135.0, 133.6, 132.0, 130.1, 129.0, 128.6, 126.8, 123.4, 17.9. HRMS (ESI-TOF) m/z: $[M+H]^+$ Calc'd for $C_{40}H_{27}N_2O_4$ [599.1893]; Found 599.1893.

doi:10.6342/NTU202201631

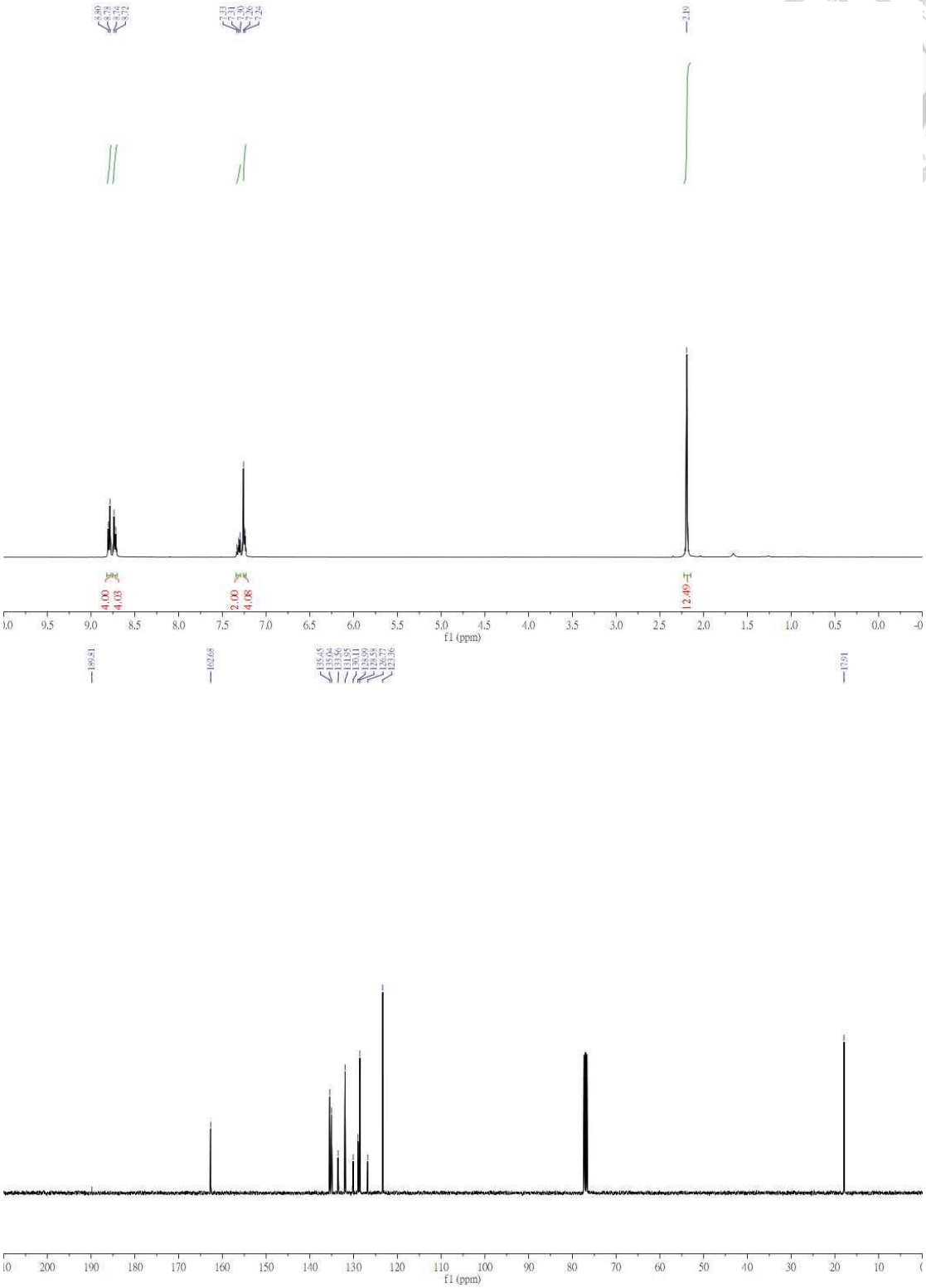

Figure S2-5. ^{1}H & ^{13}C-NMR of **PDI-D**

doi:10.6342/NTU202201631

2.6.1.5 Synthesis of **1S-PDI-D, 2S-*cis*-PDI-D, 2S-*trans*-PDI-D, 3S-PDI-D and 4S-PDI-D**

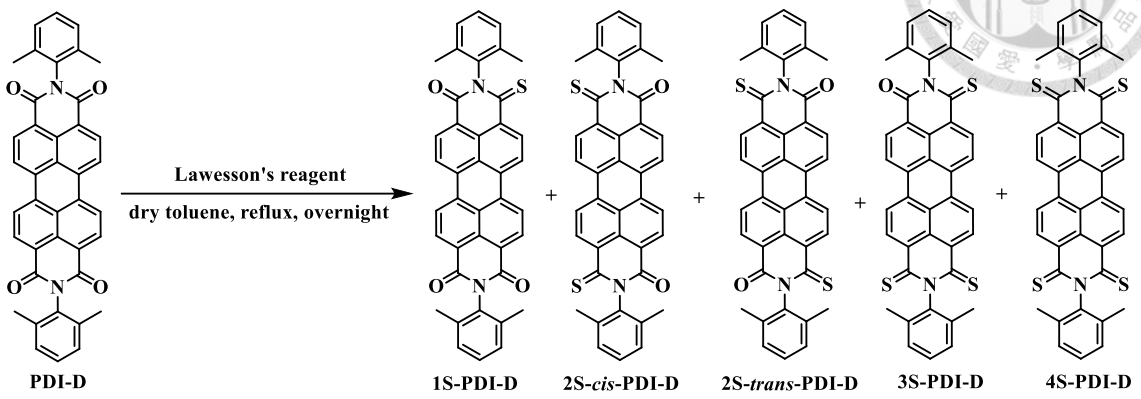

To the solution of **PDI-D** (0.20 g, 0.334 mmole, 1.00 equiv.), Lawesson's reagent (0.80 g, 2.01 mmole, 6 equiv.) in the dry toluene (40 ml) was heated to reflux overnight. After completion of reaction, the reactant was extracted with ethyl acetate and brine. The organic layer was separated, dried over $MgSO_4$ and concentrated by rotavapor. The crude product could be purified by gradient silica column (ethyl acetate: toluene = 1:50 to 1:15, R_f = 0.50). The pure product **1S-PDI-D** (0.0334 mmole, 0.0205 g, 10%)**, 2S-*cis*-PDI-D** (0.0601 mmole, 0.0379 g, 18%)**, 2S-*trans*-PDI-D** (0.0635 mmole, 0.0400 g, 19%)**, 3S-PDI-D** (0.0501 mmole, 0.0324 g, 15%)**,** and **4S-PDI-D** (0.0301 mmole, 0.0199 g, 9%) were black powder.

1S-PDI-D: FT-IR (cm^{-1}): 2921, 2850, 1710, 1661, 1591, 1334, 1242, 820, 804.^{1}H NMR (400 MHz, $CDCl_3$) δ 9.19 (d, *J* = 8.3 Hz, 1H), 8.80 – 8.74 (m, 6H), 8.66 (d, *J* = 8.3 Hz, 1H), 7.33 (dd, *J* = 11.4, 7.7 Hz, 4H), 7.24 (s, 2H), 2.17 (d, *J* = 13.1 Hz, 12H).^{13}C NMR (101 MHz, $CDCl_3$) δ 198.2, 192.0, 162.6, 160.2, 138.3, 136.6, 135.5, 135.2, 134.9, 134.8, 134.3, 133.6, 132.4, 132.1, 132.0, 130.2, 129.0, 128.8, 128.7, 128.6, 128.4, 127.8, 126.8, 126.7, 123.8, 123.7, 123.6, 123.4, 123.4, 17.9, 17.8. HRMS (ESI-TOF) m/z: $[M+H]^+$ Calc'd for $C_{40}H_{27}N_2O_3S$ [615.1664]; Found 615.1664.

doi:10.6342/NTU202201631

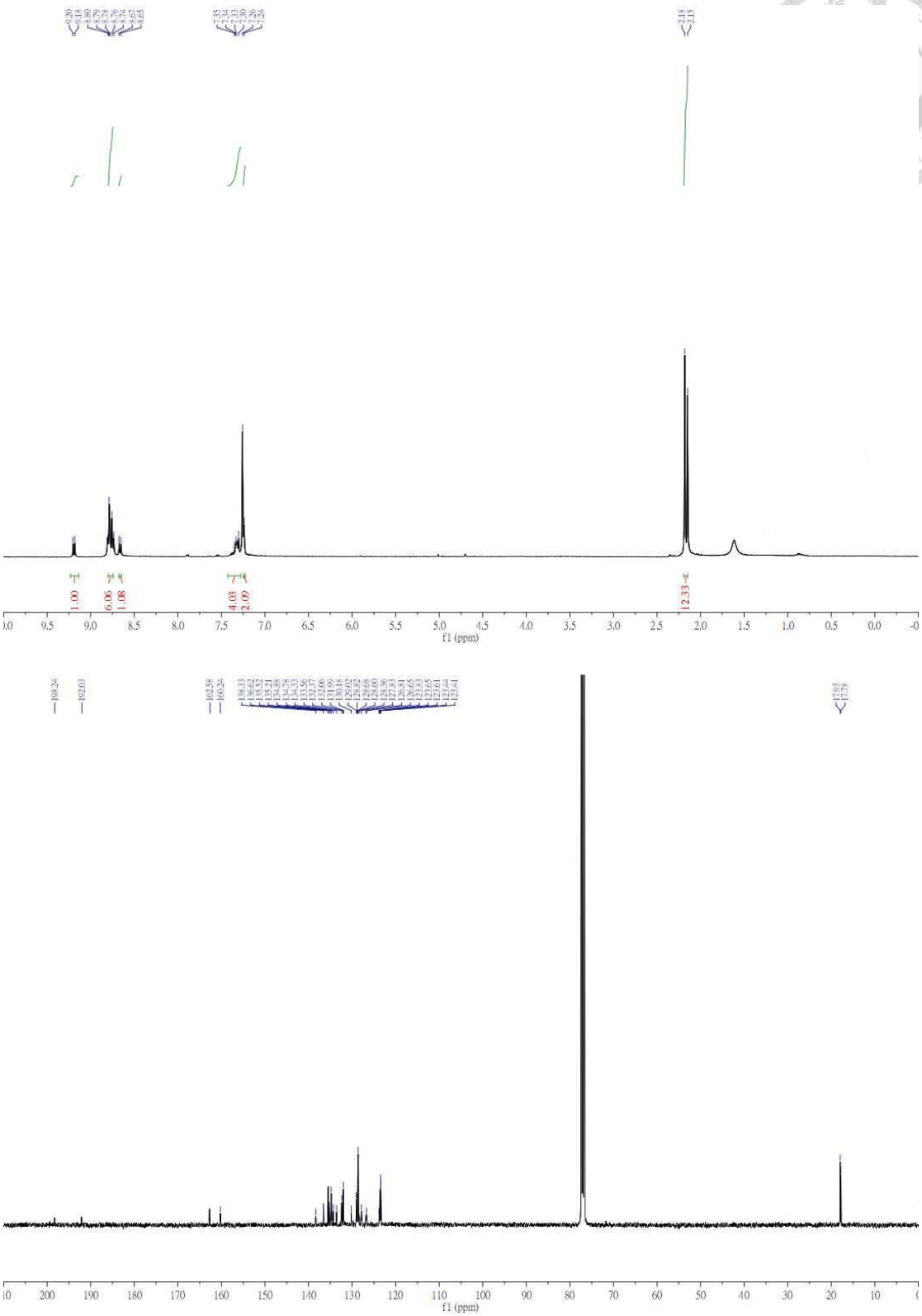

Figure S2-6. ^{1}H & ^{13}C-NMR of **1S-PDI-D**

doi:10.6342/NTU202201631

2S-*cis*-PDI-D: FT-IR (cm^{-1}):2923, 2860, 1699, 1660, 1593, 1358, 1321, 1119, 810, 801. ^{1}H NMR (400 MHz, $CDCl_3$) δ 9.17 (d, *J* = 8.3 Hz, 2H), 8.89 – 8.70 (m, 4H), 8.65 (d, *J* = 8.5 Hz, 2H), 7.43 – 7.28 (m, 4H), 7.22 (s, 2H), 2.13 (s, 12H). ^{13}C NMR (101 MHz, $CDCl_3$) δ 192.1, 160.2, 138.4, 136.6, 135.0, 134.8, 134.5, 132.3, 128.8, 128.7, 128.4, 127.8, 126.6, 123.9, 123.4, 29.7, 17.8. HRMS (ESI-TOF) m/z: $[M+H]^+$ Calc'd for $C_{40}H_{27}N_2O_2S_2$ [631.1436]; Found 631.1436.

doi:10.6342/NTU202201631

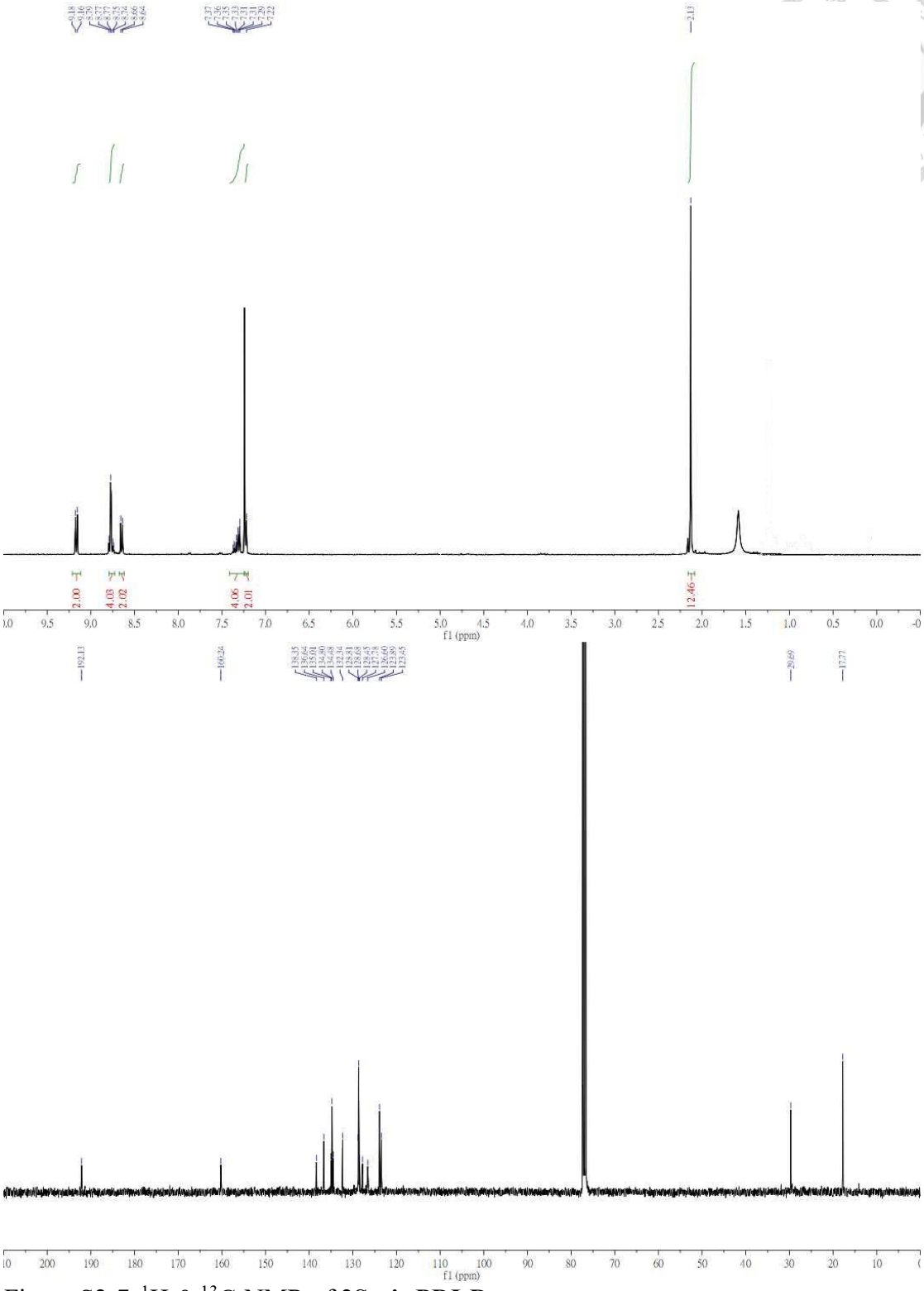

Figure S2-7. ^{1}H & ^{13}C-NMR of **2S-*cis*-PDI-D**

doi:10.6342/NTU202201631

2S-*trans*-PDI-D: FT-IR (cm^{-1}): 2963, 2922, 2851, 1682, 1587, 1466, 1332, 1238, ^{1}H NMR (400 MHz, $CDCl_3$) δ 9.15 (d, *J* = 8.4 Hz, 2H), 8.74 (dd, *J* = 6.1 Hz, 4H), 8.65 (d, *J* = 8.5 Hz, 2H), 7.30 (d, *J* = 7.8 Hz, 2H), 7.22 (d, *J* = 7.6 Hz, 4H), 2.12 (s, 12H).^{13}C NMR (101 MHz, $CDCl_3$) δ 192.1, 160.3, 138.3, 136.5, 135.0, 134.8, 134.4, 132.4, 128.8, 128.7, 128.4, 127.8, 126.6, 123.8, 123.7, 123.6, 18.1.HRMS (ESI-TOF) m/z: $[M+H]^+$ Calc'd for $C_{40}H_{27}N_2O_2S_2$ [631.1436]; Found 631.1436.

doi:10.6342/NTU202201631

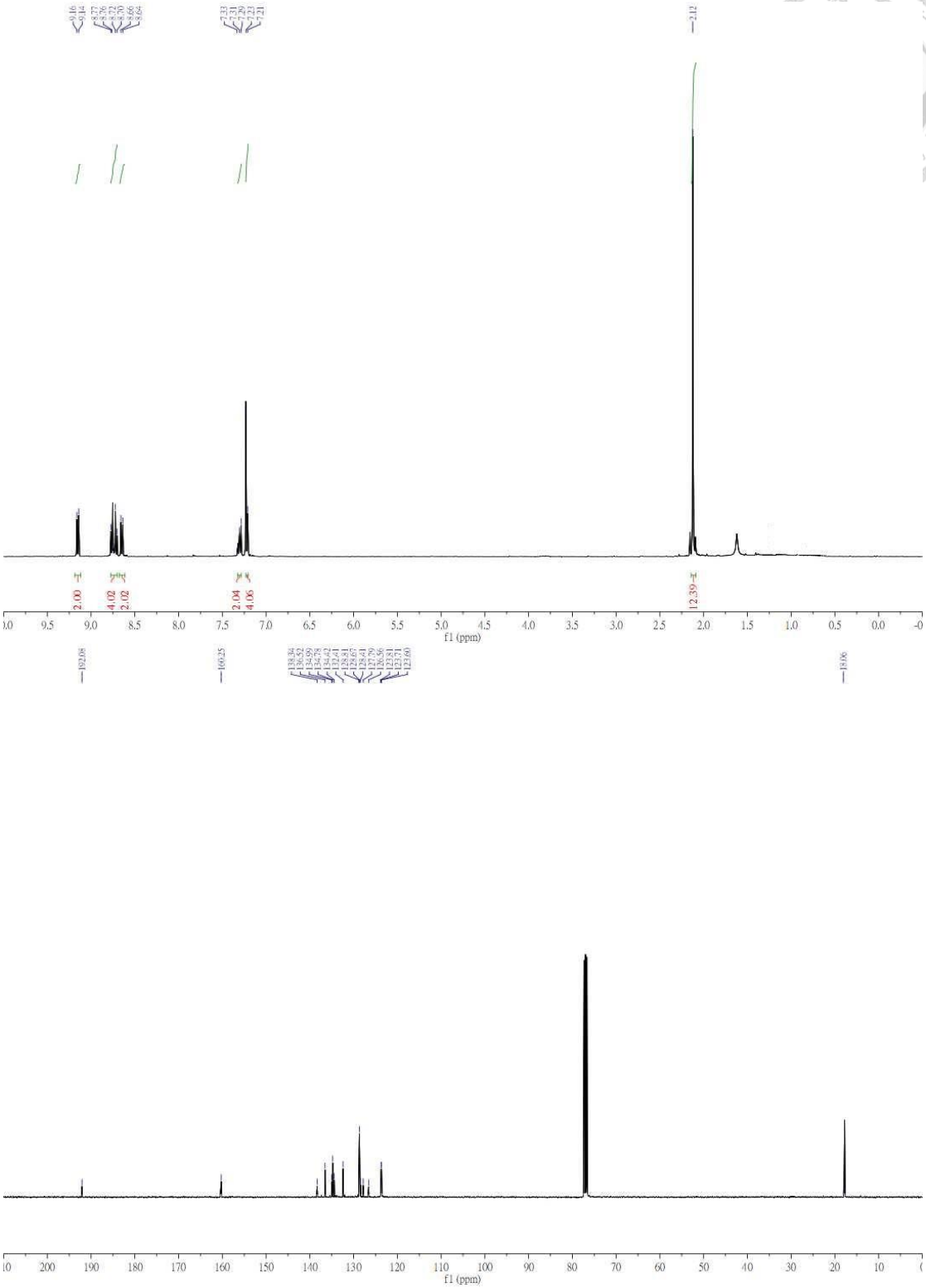

Figure S2-8. ^{1}H & ^{13}C-NMR of **2S-*trans*-PDI-D**

doi:10.6342/NTU202201631

3S-PDI-D: FT-IR (cm^{-1}): 2959, 2921, 2848, 1683, 1586, 1321, 1231, 1185. ^{1}H NMR (400 MHz, $CDCl_3$) δ 9.10 (d, *J* = 8.4 Hz, 1H), 9.01 (dd, *J* = 8.4 Hz, 2H), 8.71 (s, 2H), 8.65 – 8.54 (m, 3H), 7.26 (t, *J* = 7.4 Hz, 2H), 7.15 (d, *J* = 7.6 Hz, 4H), 2.06 (d, *J* = 11.7 Hz, 12H).^{13}C NMR (101 MHz, $CDCl_3$) δ 192.1, 187.9, 160.3, 143.5, 138.3, 137.5, 137.4, 136.6, 135.2, 134.8, 134.7, 134.2, 134.0, 134.0, 132.4, 129.6, 129.5, 128.8, 128.7, 128.7, 128.5, 127.7, 126.5, 126.4, 125.1, 124.0, 123.9, 123.8, 123.8, 123.6, 17.8. HRMS (ESI-TOF) m/z: $[M+H]^+$ Calc'd for $C_{40}H_{27}N_2OS_3$ [647.1207]; Found 647.1207.

doi:10.6342/NTU202201631

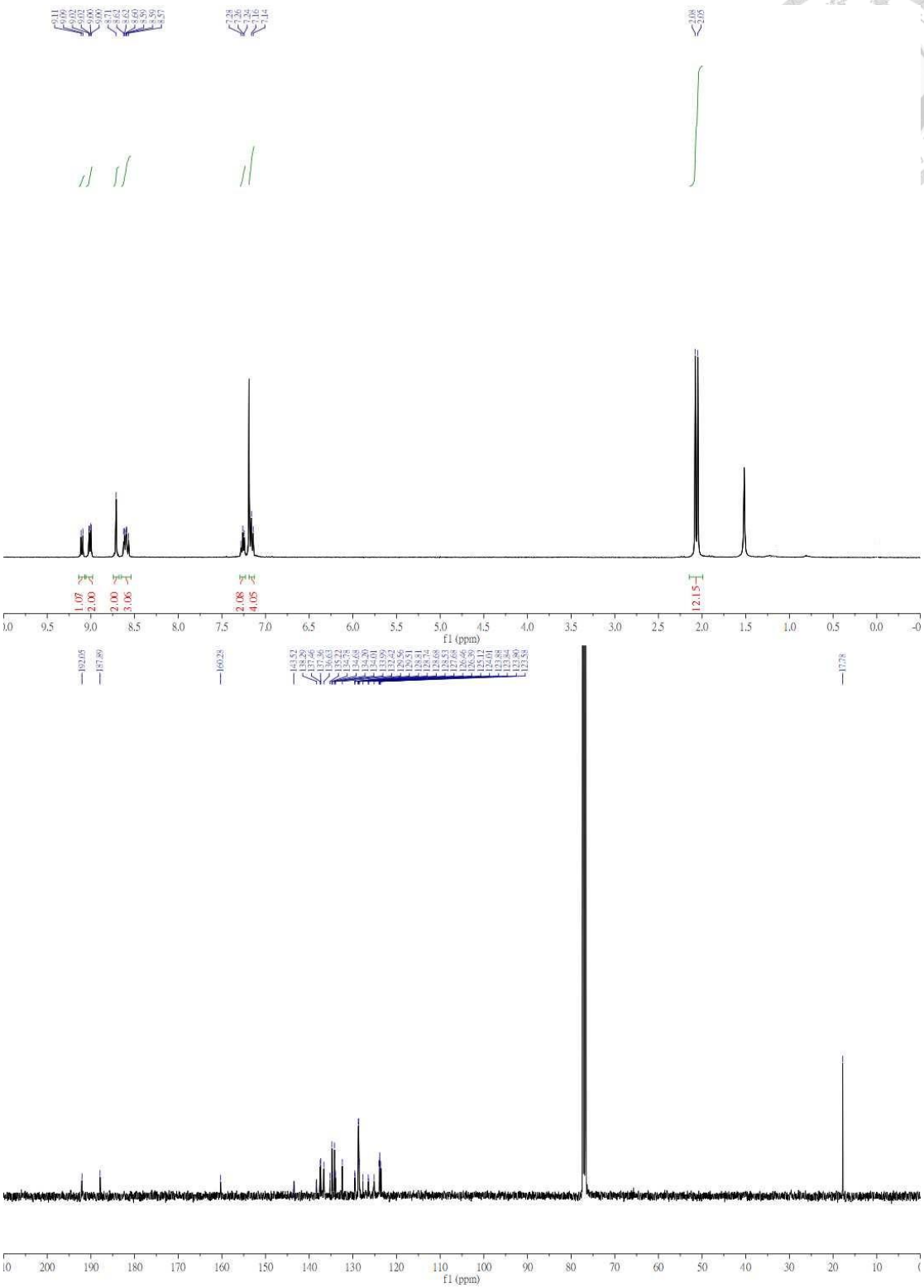

Figure S2-9. ^{1}H & ^{13}C-NMR of **3S-PDI-D**

doi:10.6342/NTU202201631

4S-PDI-D: FT-IR (cm^{-1}): 2959, 2921, 2852, 1580, 1313, 1230. ^{1}H NMR (400 MHz, $CDCl_3$) δ 9.08 (d, *J* = 8.5 Hz, 4H), 8.69 (d, *J* = 8.6 Hz, 4H), 7.35 – 7.29 (m, 2H), 7.22 (d, *J* = 7.7 Hz, 4H), 2.11 (s, 12H).^{13}C NMR (101 MHz, $CDCl_3$) δ 187.9, 143.5, 137.5, 134.3, 134.2, 129.5, 128.7, 128.5, 126.3, 125.2, 124.0, 17.8. HRMS (ESI-TOF) m/z: $[M+H]^+$ Calc'd for $C_{40}H_{27}N_2S_4$ [663.0979]; Found 663.0979.

doi:10.6342/NTU202201631

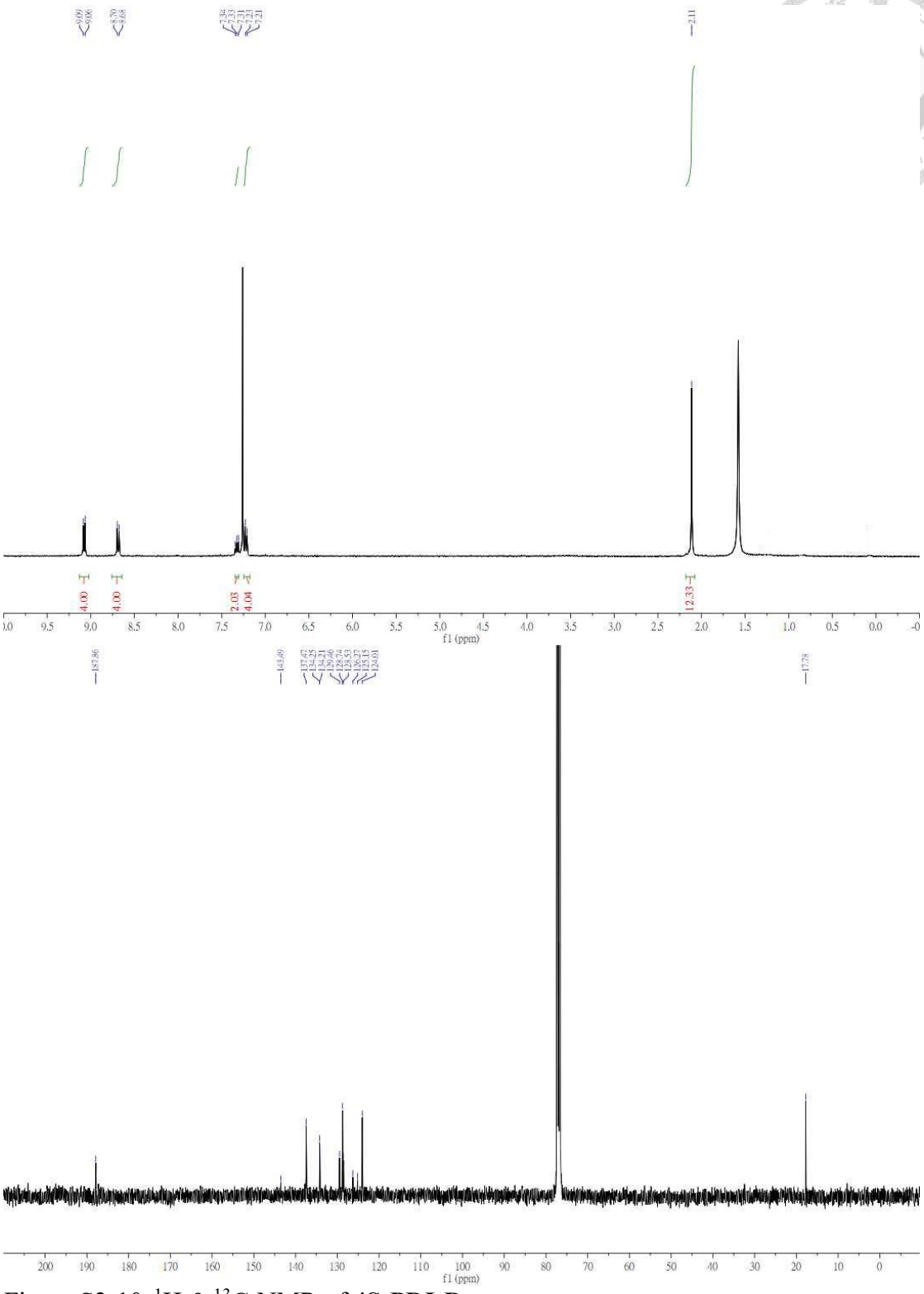

Figure S2-10. ^{1}H & ^{13}C-NMR of **4S-PDI-D**

doi:10.6342/NTU202201631

2.6.1.6 Synthesis of **1**

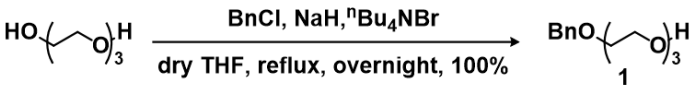

To the solution of triethylene glycol (11.86 g, 78.98 mmole, 10.00 equiv.) and Tetrabutylammonium bromide (0.20 g, 0.62 mmole, 0.08 equiv.) in the dry THF (10 ml) was added 60% sodium hydride (0.47 g, 11.85 mmole, 1.50 equiv.) slowly and stirred in the room temperature for thirty minutes. Next, benzyl chloride (1.00 g, 7.90 mmole, 1.00 equiv.) was added and heated to reflux overnight. After completion of reaction, the reactant was concentrated by rotavapor and then extracted by ethyl acetate and brine. The organic layer was separated, dried over $MgSO_4$ and concentrated by rotavapor. The crude product could be purified by silica column (ethyl acetate: hexane = 2: 1, R_f = 0.25). The pure product **1** was pale yellow liquid (6.97 mmole, 1.67 g, 88 %), FT-IR (cm^{-1}): 3418, 3031, 2867, 1734, 1454, 1351, 1248, 1098, 934, 742, 700. ^{1}H NMR (400 MHz, $CDCl_3$) δ 7.32 (d, *J* = 4.6 Hz, 5H), 4.55 (s, 2H), 3.78 – 3.50 (m, 12H), 2.50 (s, 1H). ^{13}C NMR (101 MHz, $CDCl_3$) δ 138.1, 128.3, 127.8, 127.6, 73.3, 72.5, 70.7, 70.6, 70.4, 69.4, 61.7. HRMS (ESI-TOF) m/z: $[M+H]^+$ Calc'd for $C_{13}H_{21}O_4$ [241.1362]; Found 241.1362.

doi:10.6342/NTU202201631

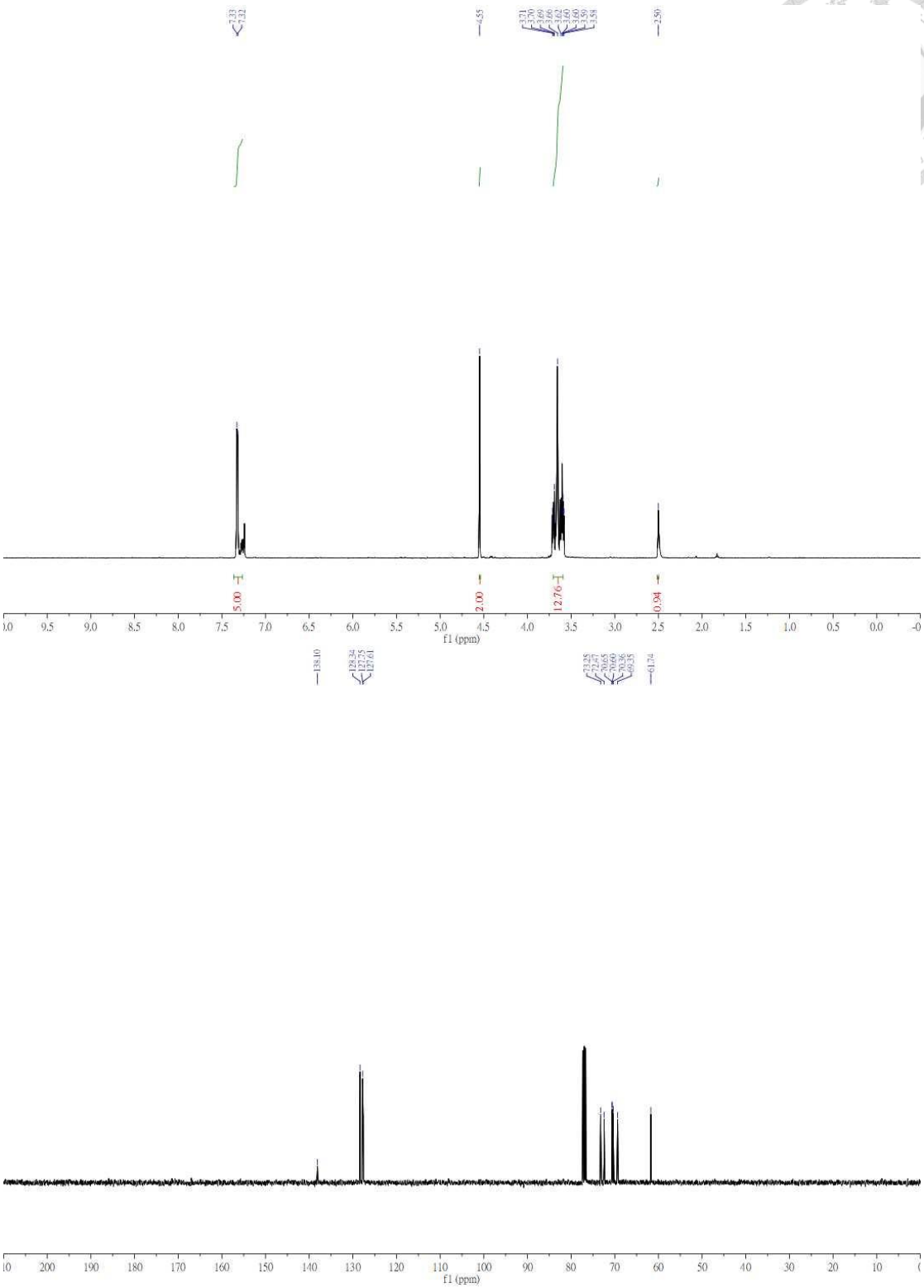

Figure S2-11. ^{1}H & ^{13}C-NMR of **1**

doi:10.6342/NTU202201631

2.6.1.7 Synthesis of **2**

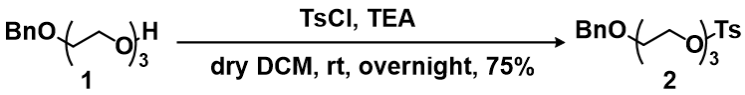

To the solution of **1** (1.00 g, 4.17 mmole, 1.00 equiv.), 4-toluenesulfonyl chloride (0.87 g, 4.58 mmole, 1.10 equiv.) and Triethylamine (0.63 g, 6.25 mmole, 1.50 equiv.) in the dry dichloromethane (10 ml) was stirred at room temperature overnight. After completion of reaction, the reactant was extracted with dichloromethane and brine. The organic layer was separated, dried over $MgSO_4$ and concentrated by rotavapor. The crude product could be purified by silica column (ethyl acetate: hexane = 2:3, R_f = 0.42). The pure product **2** was colorless liquid (3.12 mmole, 1.23 g, 75%). FT-IR (cm^{-1}):3035, 2872, 1718, 1598, 1453, 1356, 1177, 1097, 923, 817, 664. ^{1}H NMR (400 MHz, $CDCl_3$) δ 7.76 (d, J = 8.1 Hz, 2H), 7.28 (dt, J = 5.3 Hz, 7H), 4.52 (s, 2H), 4.23 – 4.00 (m, 2H), 3.74 – 3.46 (m, 10H), 2.40 (s, 3H). ^{13}C NMR (101 MHz, CDCl3) δ 144.7, 138.2, 133.0, 129.8, 128.3, 128.0, 127.7, 127.6, 73.2, 70.7, 70.6, 70.5, 69.4, 69.2, 68.7, 21.6. HRMS (ESI-TOF) m/z: $[M+H]^+$ Calc'd for $C_{20}H_{27}O_6S$ [395.1450]; Found 395.1450.

doi:10.6342/NTU202201631

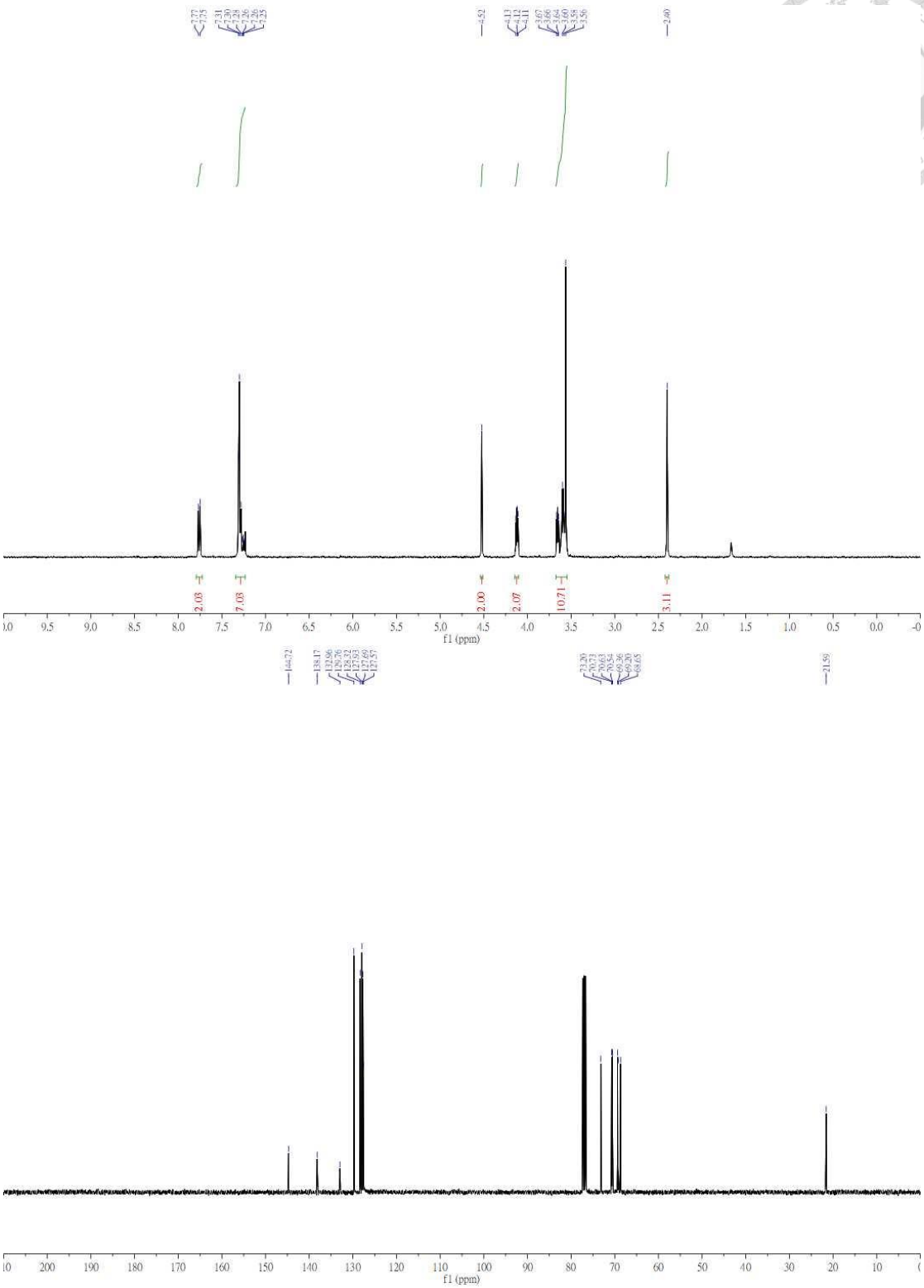

Figure S2-12. ^{1}H & ^{13}C-NMR of **2**

doi:10.6342/NTU202201631

2.6.1.8 Synthesis of **3**

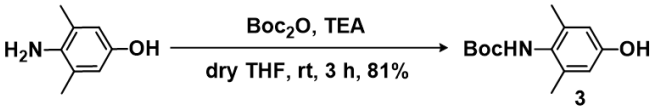

To the solution of 4-amino-3,5-xylenol (1.00 g, 7.29 mmole, 1.00 equiv.) and triethylamine (0.88 g, 8.75 mmole, 1.20 equiv.) in the dry tetrahydrofuran (10 ml) was added di-tert-butyl-dicarbonate (1.91 g, 8.75 mmole, 1.20 equiv.) and stirred at the room temperature overnight. After completion of reaction, the reactant was concentrated by rotavapor and then extracted with ethyl acetate and brine. The organic layer was separated, dried over $MgSO_4$ and concentrated by rotavapor. The crude product could be purified by silica column (ethyl acetate: hexane = 1:2, R_f = 0.40). The pure product **3** was pale yellow solid (5.91 mmole, 1.40 g, 81%). m.p.= 180-182℃, FT-IR (cm^{-1}):3311, 2986, 2923, 1677, 1597, 1508, 1369, 1250, 1152, 852.^{1}H NMR (400 MHz, DMSO) δ 9.22 (s, 1H), 7.99 (s, 1H), 6.40 (s, 2H), 2.01 (s, 6H), 1.39 (s, 9H).^{13}C NMR (101 MHz, DMSO) δ 155.2, 154.1, 136.8, 126.6, 114.1, 77.8, 28.2, 18.1. HRMS (ESI-TOF) m/z: $[M+H]^+$ Calc'd for $C_{13}H_{20}NO_3$ [238.1365]; Found 238.1365.

doi:10.6342/NTU202201631

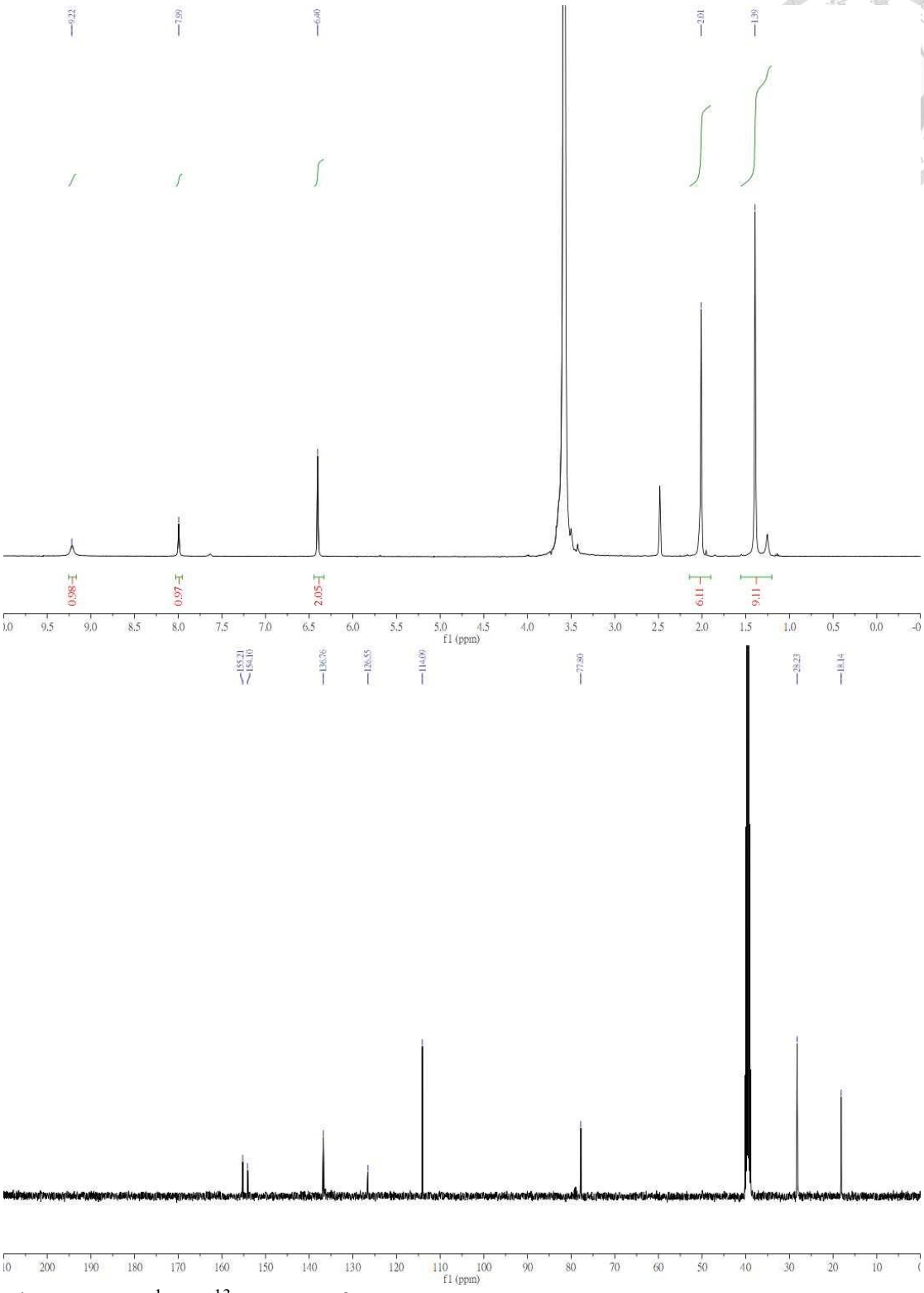

Figure S2-13. ^{1}H & ^{13}C-NMR of **3**

doi:10.6342/NTU202201631

2.6.1.9 Synthesis of **4**

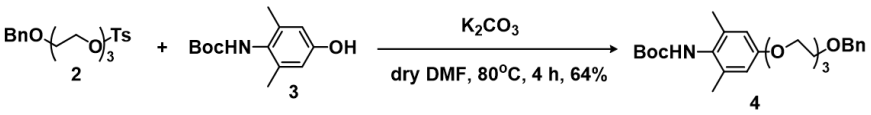

To the solution of **2** (1.00 g, 2.54 mmole, 1.00 equiv.), **3** (0.63 g, 2.66 mmole, 1.05 equiv.) and potassium carbonate (0.42 g, 3.04 mmole, 1.20 equiv.) in the dry dimethylformamide (10 ml) was heated to 80℃ for four hours. After completion of reaction, the reactant was extracted with ethyl acetate and brine. The organic layer was separated, dried over $MgSO_4$ and concentrated by rotavapor. The crude product could be purified by silica column (ethyl acetate: hexane = 1:2, R_f = 0.40). The pure product **4** was light yellow liquid (1.63 mmole, 0.75 g, 64%). FT-IR (cm^{-1}):3318, 2935, 2869, 1719, 1596, 1498, 1365, 1244, 738, 699. ^{1}H NMR (400 MHz, $CDCl_3$) δ 7.33 (d, *J* = 4.6 Hz, 5H), 6.59 (s, 2H), 5.91 (s, 1H), 4.55 (s, 2H), 4.05 (d, *J* = 4.5 Hz, 2H), 3.81 (s, 2H), 3.74 – 3.56 (m, 8H), 2.19 (s, 6H), 1.49 (s, 9H). ^{13}C NMR (101 MHz, $CDCl_3$) δ 157.0, 154.0, 138.1, 137.1, 128.2, 127.5, 127.4, 113.8, 79.4, 73.0, 70.6, 70.5, 69.6, 69.3, 67.2, 28.2, 18.4. HRMS (ESI-TOF) m/z: $[M+H]^+$ Calc'd for $C_{26}H_{38}NO_6$ [460.2621]; Found 460.2621.

doi:10.6342/NTU202201631

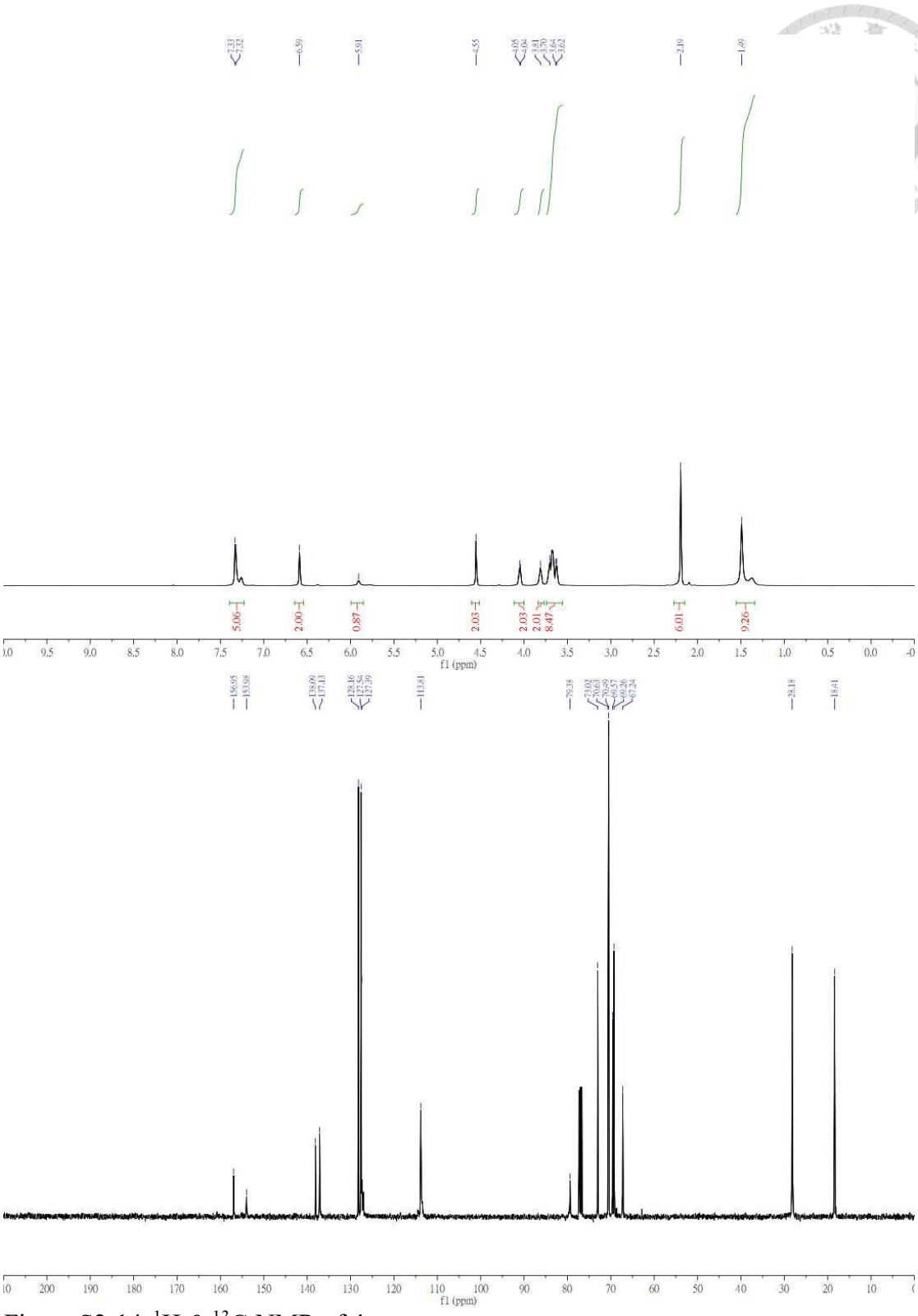

Figure S2-14. ^{1}H & ^{13}C-NMR of **4**

doi:10.6342/NTU202201631

2.6.1.10 Synthesis of **5**

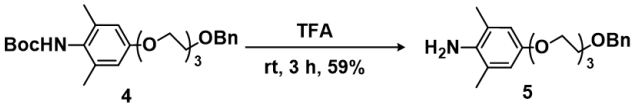

4 5

To the solution of **4** (1.65 g, 3.59 mmole, 1.00 equiv.) in the trifluoroacetic acid (10 ml) was stirred in the room temperature overnight. After completion of reaction, trifluoroacetic acid was concentrated by rotavapor and then extracted with ethyl acetate and $NaHCO_3$ (aq.). The organic layer was separated, dried over $MgSO_4$ and concentrated by rotavapor. The crude product could be purified by silica column (methanol: dichloromethane = 1:10, R_f = 0.90). The pure product **5** was light orange liquid (2.11 mmole, 0.76 g, 59%). FT-IR (cm^{-1}):3445, 2919, 2869, 1602, 1489, 1456, 1100, 746, 699. ^1H NMR (400 MHz, $CDCl_3$) δ 7.34 – 7.24 (m, 5H), 6.55 (s, 2H), 4.55 (s, 2H), 4.12 – 3.96 (m, 2H), 3.87 – 3.76 (m, 2H), 3.72 – 3.61 (m, 8H), 2.28 (s, 6H).^{13}C NMR (101 MHz, $CDCl_3$) δ 150.8, 138.0, 136.3, 128.1, 127.4, 127.3, 122.8, 114.7, 72.9, 70.5, 70.4, 69.7, 69.2, 67.8, 62.7, 17.7. HRMS (ESI-TOF) m/z: $[M+H]^+$ Calc'd for $C_{21}H_{30}NO_4$ [360.2097]; Found 360.2097.

doi:10.6342/NTU202201631

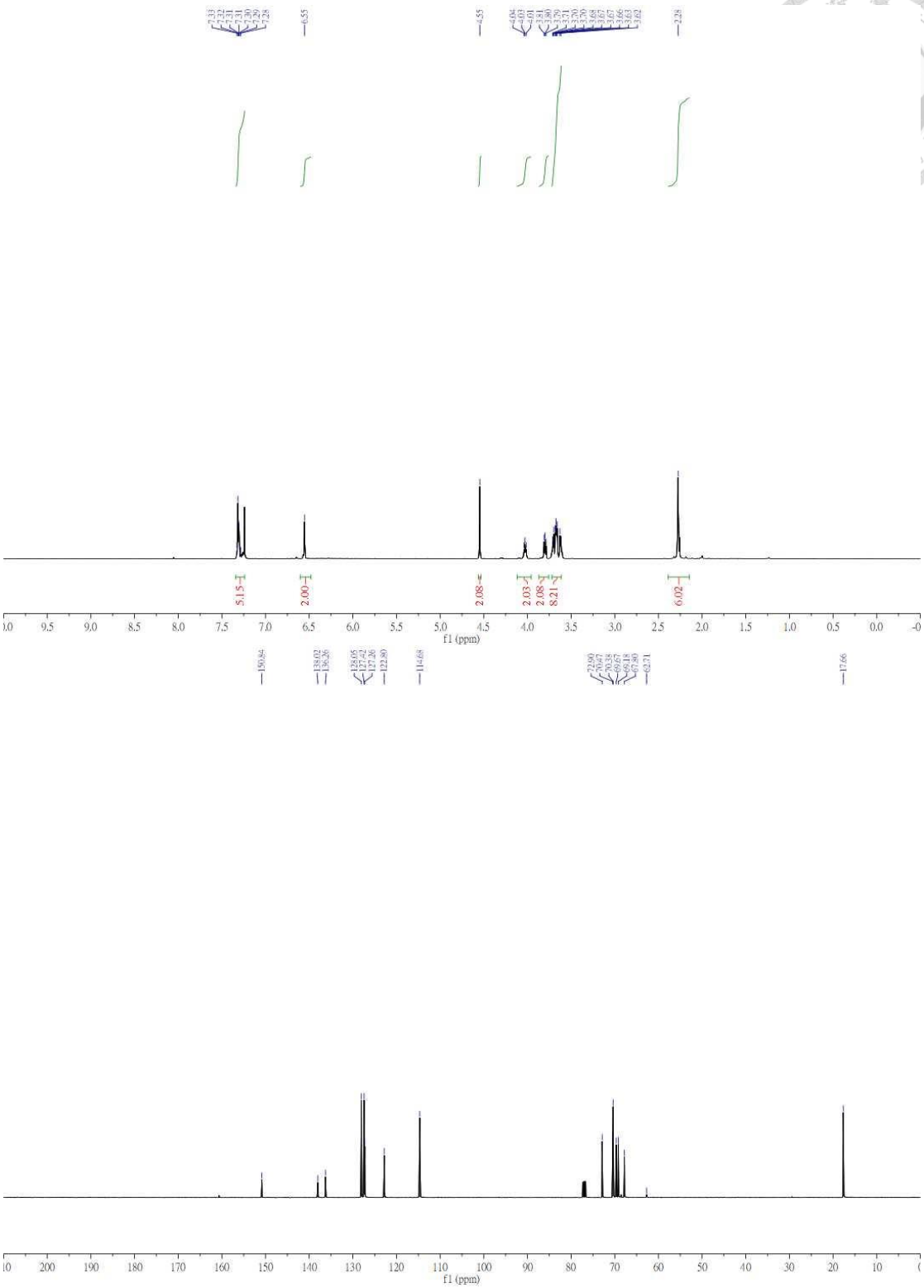

Figure S2-15. ^{1}H & ^{13}C-NMR of **5**

doi:10.6342/NTU202201631

2.6.1.11 Synthesis of **6**

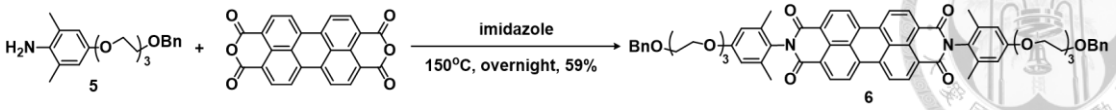

To the solution of **5** (1.00 g, 2.78 mmole, 2.10 equiv.), 3,4,9,10-perylenetetracarboxylic dianhydride (0.52 g, 1.32 mmole, 1.00 equiv.) and imidazole (10.00 g, 146.89 mmole) was heated to 150℃ overnight. After completion of reaction, 1,4-dioxane was added. When the system was cooled down, the mixture concentrated by rotavapor. The crude product could be purified by silica column (methanol: dichloromethane = 1:10, R_f = 0.80). The pure product **6** was red powder (0.78 mmole, 0.84 g, 59%). FT-IR (cm^{-1}):2923, 2864, 1700, 1652, 1596, 1358, 1318, 1255, 1120, 818, 750. ^{1}H NMR (400 MHz, $CDCl_3$) δ 8.72 (dd, *J* = 8.0 Hz, 8H), 7.38 – 7.23 (m, 10H), 6.76 (s, 4H), 4.56 (s, 4H), 4.13 (t, *J* = 4.7 Hz, 4H), 3.85 (t, *J* = 4.7 Hz, 4H), 3.68 (dt, *J* = 22.4, 4.7 Hz, 16H), 2.10 (s, 12H).^{13}C NMR (101 MHz, $CDCl_3$) δ 163.2, 158.9, 138.5, 136.9, 135.2, 132.2, 130.3, 128.6, 128.0, 127.8, 127.0, 126.6, 123.6, 123.6, 114.7, 73.5, 71.1, 71.0, 69.9, 69.7, 67.7, 18.4. HRMS (ESI-TOF) m/z: $[M+H]^+$ Calc'd for $C_{66}H_{63}N_2O_{12}$ [1075.4303]; Found 1075.4303.

doi:10.6342/NTU202201631

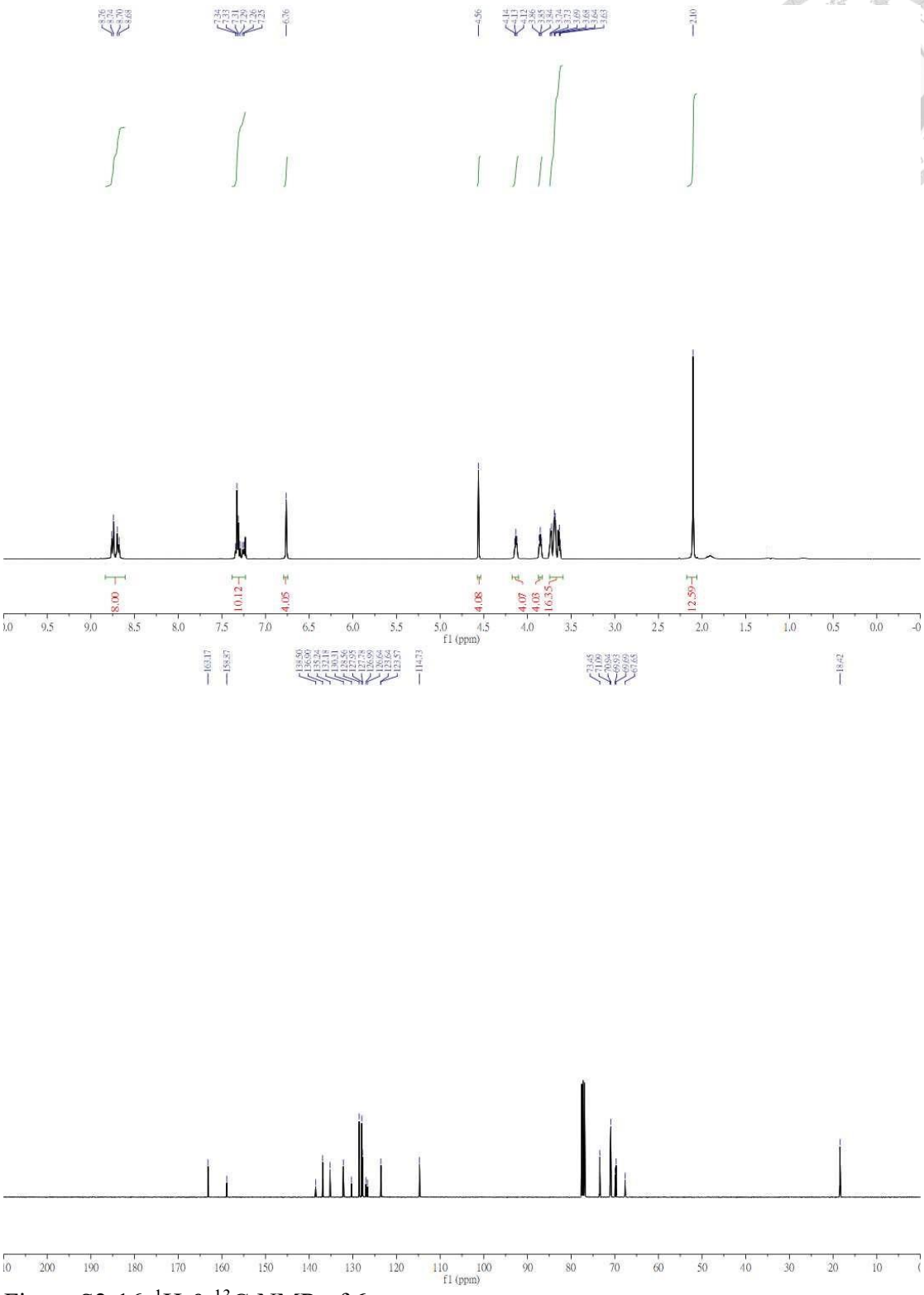

Figure S2-16. ^{1}H & ^{13}C-NMR of **6**

doi:10.6342/NTU202201631

2.6.1.12 Synthesis of **7**

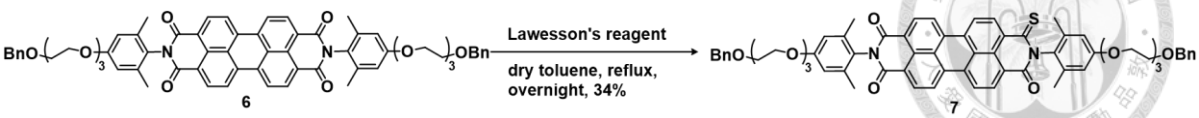

6 7

To the solution of **6** (0.60 g, 0.56 mmole, 1.00 equiv.), Lawesson's reagent (0.34 g, 0.84 mmole, 1.50 equiv.) in the dry toluene (40 ml) was heated to reflux overnight. After completion of reaction, the reactant was extracted with ethyl acetate and brine. The organic layer was separated, dried over $MgSO_4$ and concentrated by rotavapor. The crude product could be purified by silica column (ethyl acetate: toluene = 1:1, R_f = 0.50). The pure product **7** was black powder (0.19 mmole, 0.21 g, 34%). FT-IR (cm^{-1}):2927, 2872, 1700, 1660, 1600, 1362, 1183, 1072, 818, 746. ^{1}H NMR (400 MHz, $CDCl_3$) δ 9.16 (d, *J* = 8.4 Hz, 1H), 8.77 – 8.71 (m, 6H), 8.63 (d, *J* = 8.6 Hz, 1H), 7.34 (t, *J* = 6.6 Hz, 10H), 6.77 (d, *J* = 3.9 Hz, 4H), 4.57 (s, 4H), 4.15 (t, *J* = 4.8 Hz, 4H), 3.87 (t, *J* = 4.7 Hz, 4H), 3.69 (td, *J* = 16.1, 7.9 Hz, 16H), 2.09 (d, *J* = 13.9 Hz, 12H).^{13}C NMR (101 MHz, $CDCl_3$) δ 192.6, 163.0, 163.0, 160.5, 158.7, 158.5, 138.3, 136.7, 136.0, 135.2, 135.0, 134.8, 134.3, 132.4, 132.1, 132.0, 131.4, 130.1, 128.4, 127.8, 127.6, 126.7, 126.6, 126.4, 123.9, 123.6, 123.5, 123.4, 123.4, 114.5, 114.5, 73.3, 70.9, 70.7, 69.7, 69.5, 67.4, 67.3, 18.1. HRMS (ESI-TOF) m/z: $[M+H]^+$ Calc'd for $C_{66}H_{63}N_2O_{11}S$ [1091.4074]; Found 1091.4074.

doi:10.6342/NTU202201631

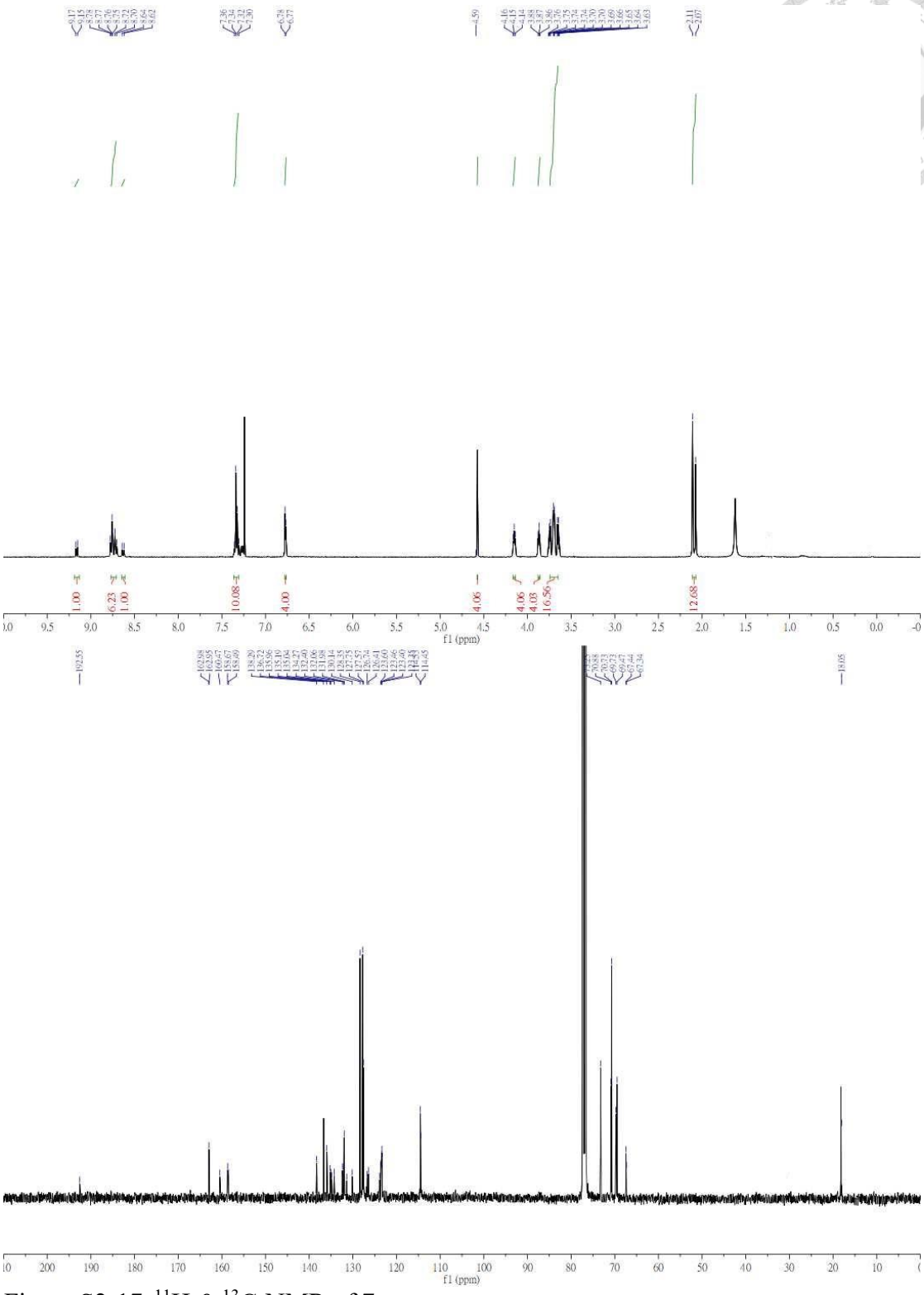

Figure S2-17. ^{11}H & ^{13}C-NMR of **7**

doi:10.6342/NTU202201631

2.6.1.13 Synthesis of **8**

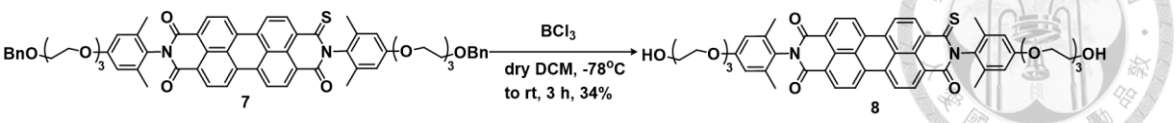

To the solution of **7** (0.15 g, 0.14 mmole, 1.00 equiv.), in the dry dichloromethane (10ml) was cooled to -78℃ and added boron trichloride (0.097 g, 0.83 mmole, 6 equiv.). After addition of boron trichloride, the system was warmed to room temperature and stirred three hours. After completion of reaction, the reactant was extracted with dichloromethane and brine. The organic layer was separated, dried over $MgSO_4$ and concentrated by rotavapor. The crude product could be purified by silica column (methanol: dichloromethane = 1:10, R_f = 0.27). The pure product **8** was black powder (0.089 mmole, 0.081 g, 65%). FT-IR (cm^{-1}):3408, 2928, 2860, 1664, 1362, 1258, 1116, 818, 750.^{1}H NMR (400 MHz, $CDCl_3$) δ 9.14 (d, J = 8.9 Hz, 1H), 8.72 (dd, J = 6.6 Hz, 6H), 8.61 (d, J = 8.6 Hz, 1H), 6.78 (s, 4H), 4.14 (d, J = 8.9 Hz, 4H), 3.94 – 3.44 (m, 20H), 2.11 (t, J = 14.1 Hz, 12H).^{13}C NMR (101 MHz, $CDCl_3$) δ 192.5, 163.0, 163.0, 160.5, 158.5, 158.4, 156.8, 140.5, 136.8, 136.0, 135.9, 135.2, 135.0, 134.8, 134.3, 134.3, 132.4, 132.1, 132.0, 131.5, 130.1, 128.4, 128.2, 128.1, 127.8, 126.7, 126.6, 126.4, 126.3, 125.5, 123.8, 123.6, 123.4, 114.5, 114.4, 111.7, 72.5, 72.4, 70.8, 70.4, 69.7, 68.1, 67.4, 61.8, 29.7, 18.2, 18.0.HRMS (ESI-TOF) m/z: $[M+H]^+$ Calc'd for $C_{52}H_{51}N_2O_{11}S$ [911.3135]; Found 911.3135.

doi:10.6342/NTU202201631

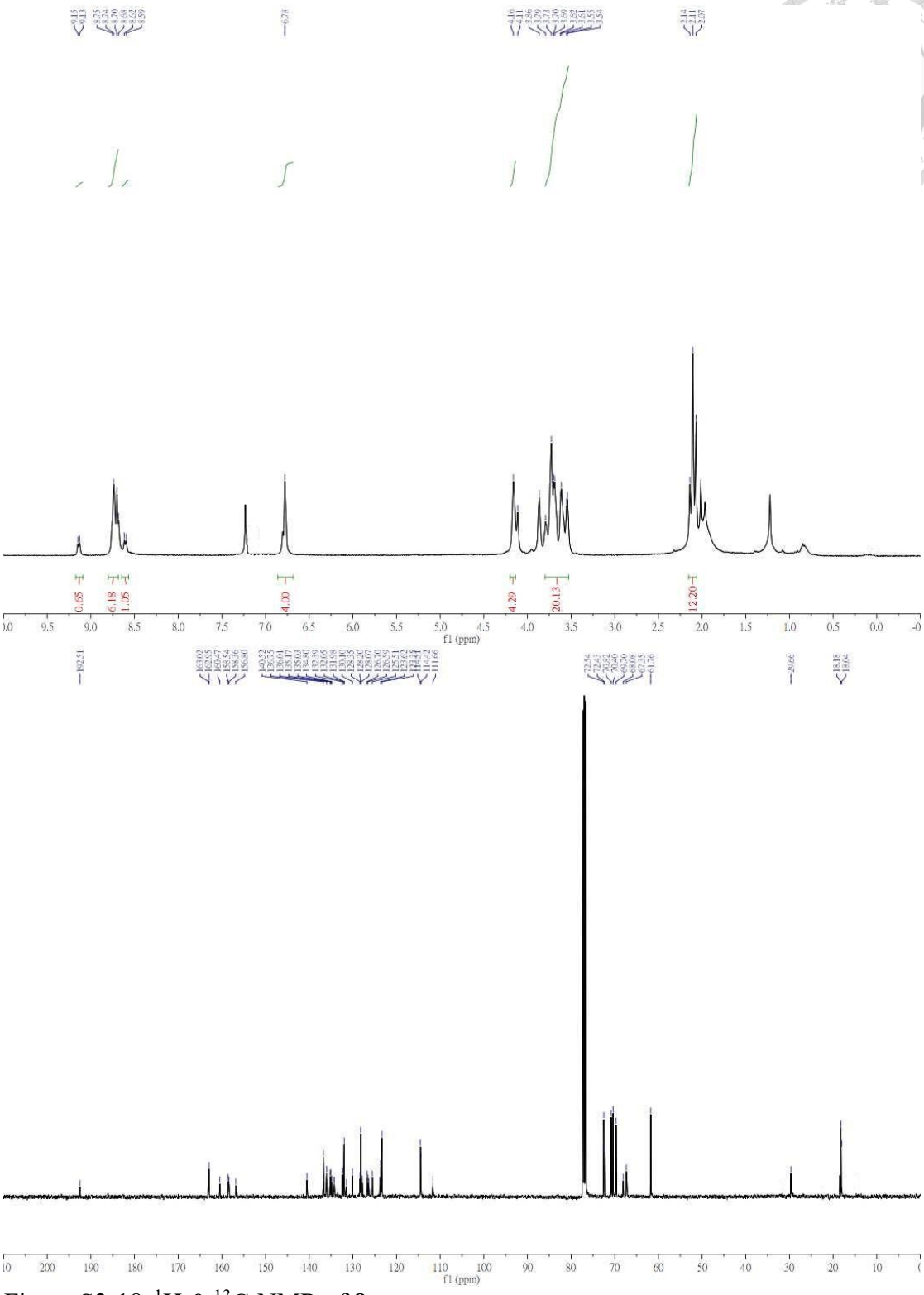

Figure S2-18. ^{1}H & ^{13}C-NMR of **8**

doi:10.6342/NTU202201631

2.6.1.14 Synthesis of **1S-NO₂**

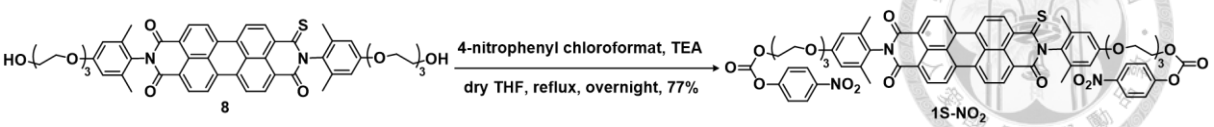

8 → 1S-NO₂

To the solution of **8** (0.04 g, 0.044 mmole, 1.00 equiv.), 4-nitrophenylchloroformate (0.0555 g, 0.264 mmole, 6.00 equiv.) and triethylamine (0.053 g, 0.53 mmole, 12.00 equiv.) in the dry Tetrahydrofuran (5 ml) was heated to reflux overnight. After completion of reaction, the reactant was extracted with ethyl acetate and brine. The organic layer was separated, dried over $MgSO_4$ and concentrated by rotavapor. The crude product could be purified by silica column (methanol: dichloromethane = 1:10, R_f = 0.73). The pure product **1S-NO₂** was deep black powder (0.010 mmole, 0.0127 g, 23%). FT-IR (cm^{-1}):2971, 2924, 1761, 1659, 1525, 1317, 1223, .^{1}H NMR (400 MHz, $CDCl_3$) δ 9.15 (d, *J* = 8.3 Hz, 1H), 8.73 (m, *J* = 8.1 Hz, 6H), 8.62 (d, *J* = 8.5 Hz, 1H), 8.26 (d, *J* = 9.0 Hz, 4H), 7.37 (d, *J* = 9.1 Hz, 4H), 6.78 (s, 4H), 4.52 – 4.39 (m, 4H), 4.23 – 4.08 (m, 4H), 4.00 – 3.66 (m, 16H), 2.09 (d, *J* = 13.2 Hz, 12H). ^{13}C NMR (101 MHz, $CDCl_3$) δ 192.5, 163.0, 160.5, 158.6, 158.4, 156.8, 155.6, 152.4, 145.3, 140.6, 140.6, 136.8, 136.0, 135.0, 134.3, 132.5, 131.9, 130.1, 129.7, 128.2, 126.6, 125.3, 123.6, 123.4, 121.8, 114.5, 114.4, 70.9, 70.8, 69.8, 68.7, 68.3, 67.4, 29.7, 18.2, 18.1. HRMS (ESI-TOF) m/z: $[M+H]^+$ Calc'd for $C_{66}H_{57}N_4O_{19}S$ [1241.3259]; Found 1241.3259.

doi:10.6342/NTU202201631

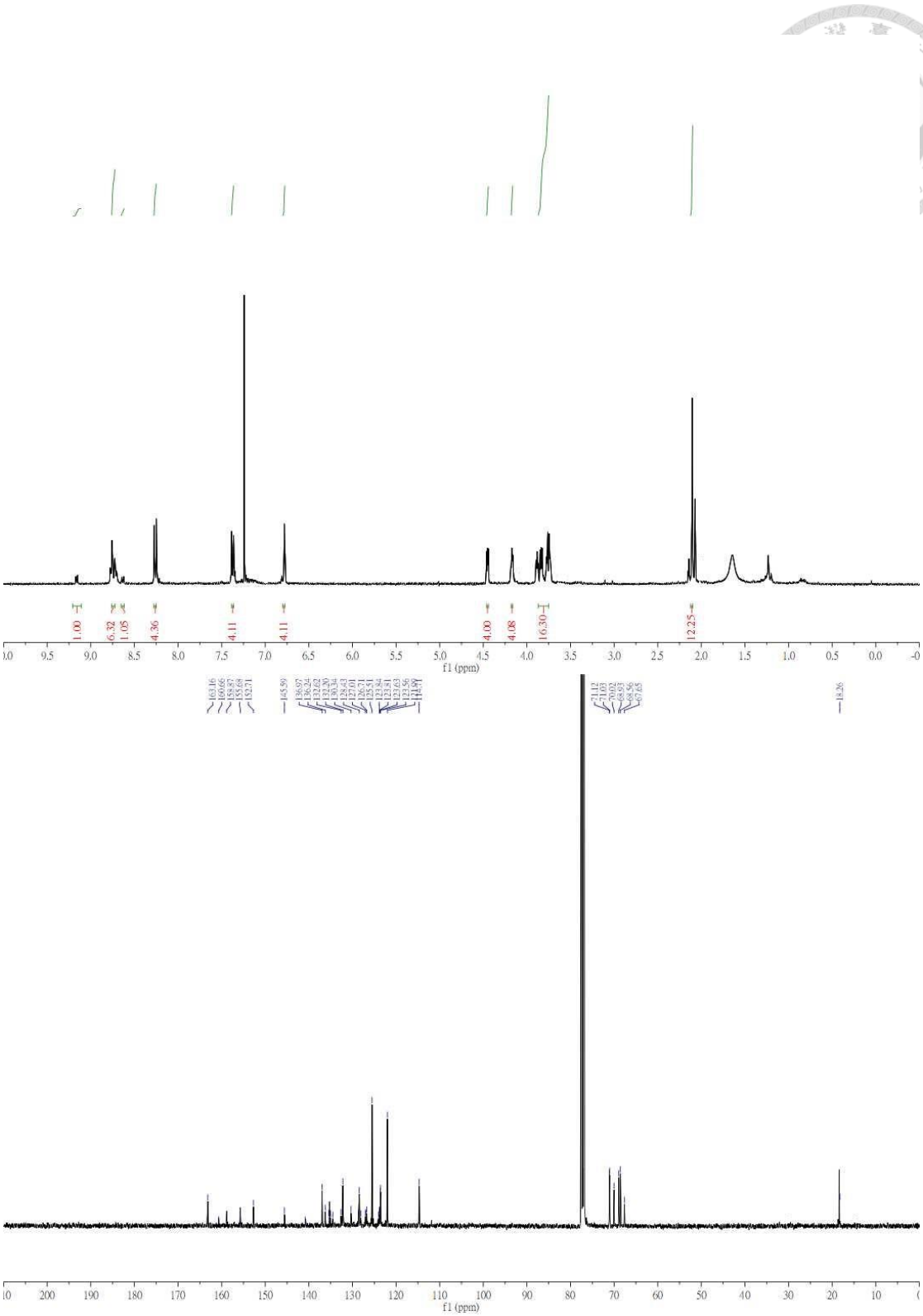

Figure S2-19. ^{1}H & ^{13}C-NMR of **1S-NO$_2$**

doi:10.6342/NTU202201631

2.6.1.15 Synthesis of **1S-FC131**

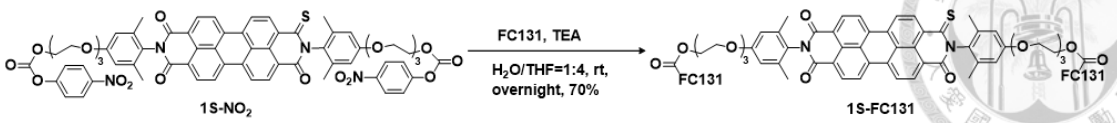

To the solution of **1S-NO$_2$** (0.829 mg, 0.668x10^{-3} mmole, 1.00 equiv.) and FC131 (1 mg, 1.37x10^{-3} mmole, 2.05 equiv.) in the 2ml THF and 0.5ml water was added triethylamine (0.0028 mg, 2.00x10^{-3} mmole, 3 equiv.) under nitrogen protection. The system was kept stirring at the room temperature overnight. After completion of reaction, the mixture was concentrated in rotavapor and vacuum. Then the final compound **1S-FC131** would be obtained without further purification (1.13 mg, 0.468x10^{-3} mmole, 70%). HRMS (MALDI-TOF) m/z: $[M+H]^+$ Calc'd for $C_{126}H_{140}N_{24}O_{25}S$ [2422.01]; Found 2422.01

doi:10.6342/NTU202201631

2.6.1.16 Synthesis of **Cy5-1S-FC131**

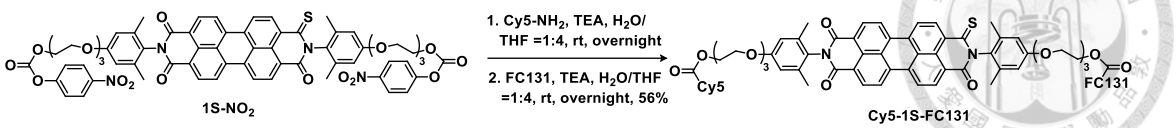

To the solution of **1S-NO$_2$** (8.29 mg, 6.68x10^{-3} mmole, 10.00 equiv.) and Cy5-NH$_2$(0.829 mg, 6.68x10^{-3} mmole, 1.00 equiv.) in the 6 mL (H$_2$O/THF=1/4) solution was added Triethylamine under nitrogen protection. The system was stirring in the room temperature overnight. After completion of reaction, the mixture was concentrated in rotavapor and purified by silica gel (methanol: dichloromethane = 1: 10, Rf = 0.42) to afford **Cy5-NO$_2$**. HRMS (MALDI-TOF) m/z: [M] $^+$ Calc'd for $C_{98}H_{104}N_7O_{17}S^+$ [1682.7204]; Found 1682.7204. The blue powder had been got and mixed with FC131 (1mg, 1.37x10^{-3} mmole, 2.05 equiv.) and triethylamine (0.0028 mg, 2.00x10^{-3} mmole, 3 equiv.) in 6 mL (H$_2$O/THF=1/4) solution under nitrogen protection. The system was kept stirring at the room temperature overnight. After completion of reaction, the mixture was concentrated in rotavapor and vacuum. Then the final compound **Cy5-FC131** would be obtained without further purification (1.77 mg, 7.67x10^{-4} mmole, 56%). HRMS (MALDI-TOF) m/z: [M] $^+$ Calc'd for $C_{128}H_{146}N_{17}O_{20}S^+$ [2273.0645]; Found 2273.0645.

doi:10.6342/NTU202201631

2.6.2 Spectrum

2.6.2.1 Steady-state spectra, PLQY and lifetime measurements

Steady-state absorption and emission spectra were recorded by a double-beam spectrophotometer (Hitachi U-3310) and a fluorescence spectrometer (Edinburgh FS920), respectively. The photoluminescence quantum yields (PLQYs) were obtained by a comparative method relative to Rhodamine 6G (Q.Y.=0.94) in methanol. The time-resolved studies were performed by a time-correlated single photon counting (TCSPC) technique (Edinburgh FLS980) with a picosecond pulsed diode laser as the excitation light source.

2.6.2.2 Singlet oxygen generation test

The singlet oxygen generation ability was determined by O_2 ($^1\Delta_g \rightarrow {}^3\Sigma_g^-$ (0,0)) emission at 1273 nm by using a fluorescence spectrometer (Edinburgh FLS980) with a NIR-PMT detector relative to tetraphenylporphyrin (Φ_Δ=0.60) in deuterated benzene.

2.6.2.3 Z-scan experiments

A mode-locked Ti:sapphire laser (Tsunami, Spectra Physics) produced single Gaussian pulse (800 nm) which was coupled to a regenerative amplifier that generated approximately 180 fs and 1 mJ pulse (800 nm, 1 kHz, Spitfire, Spectra Physics) was applied to measurement of the one-photon absorption properties in the NIR region. An optical parametric amplifier (Light Conversion, TOPAS-C) was then used to generate the excitation light in the near infrared region. The dual beam setup in the Z-scan experiment has been well controlled under stable laser intensity. One of the laser beams after passing

doi:10.6342/NTU202201631

through a beam splitter was concentrated on the sample cell (1 mm) by a lens with a focal length (7.5 cm). The position of the sample cell could be adjusted with the laser beam direction by the motor-controlled stage. The other laser beam was then used to monitor the local power density. The transmitted light from the sample cells was tested by the same photodiode. These nonlinear absorption coefficients for a Gaussian beam profile can be obtained by a curve fitting of the observed open-aperture traces T(z) with the equation (1):

$$T(z) = \sum_{n=0}^{\infty} \frac{(-q)^n}{(n+1)^{3/2}}; q = \frac{\beta I_0 L}{1+\frac{z^2}{z_0^2}}$$

where n, an integer, ranged from 0 to ∞ and has been truncated at n = 1000; I_0 was the input intensity; L was the sample cell path-length; z_0 denotes the diffraction length of the incident beam (Rayleigh range) and z represents the sample position with respect to the focal plane. After obtaining the TPA coefficient (β), TPA cross section (σ_2) can be deduced with equation (2):

$$\beta = \frac{\sigma_2 N_A d \times 10^{-3}}{h\nu}$$

where N_A was the Avogadro constant, d was the sample concentration, and $h\nu$ was the incident photon energy.

doi:10.6342/NTU202201631

2.6.2.4 Two-photon absorption spectrum

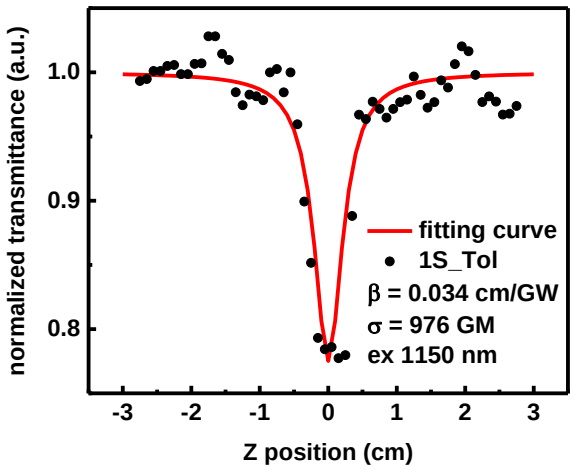

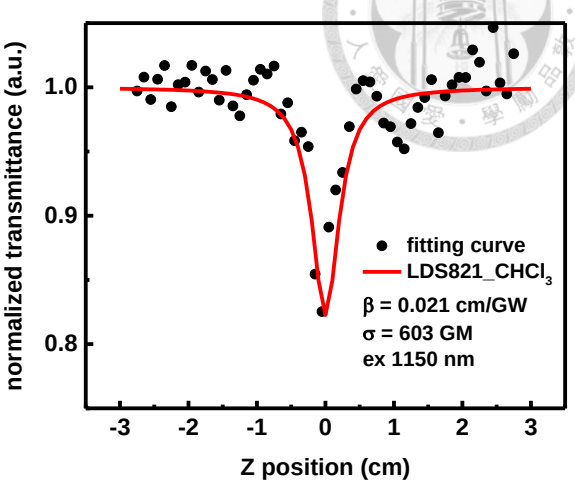

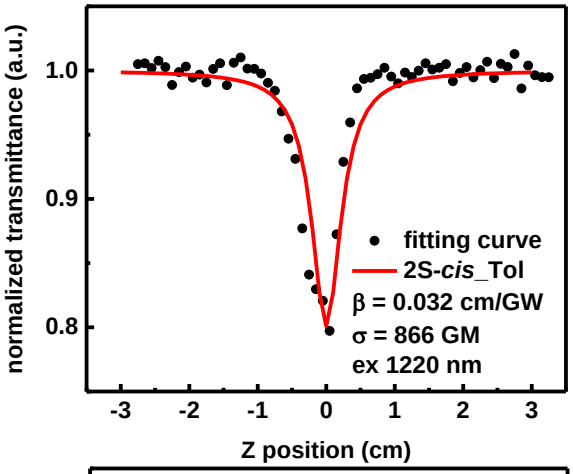

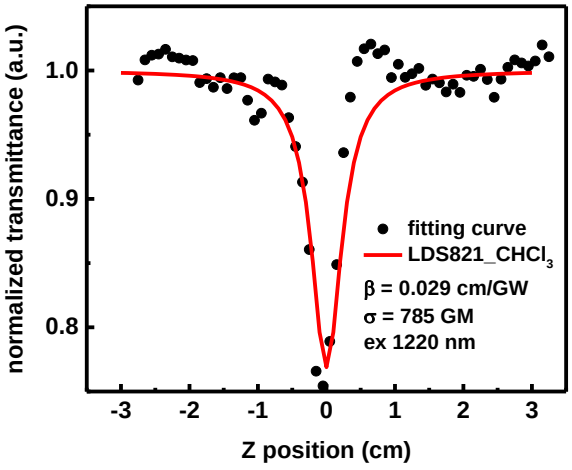

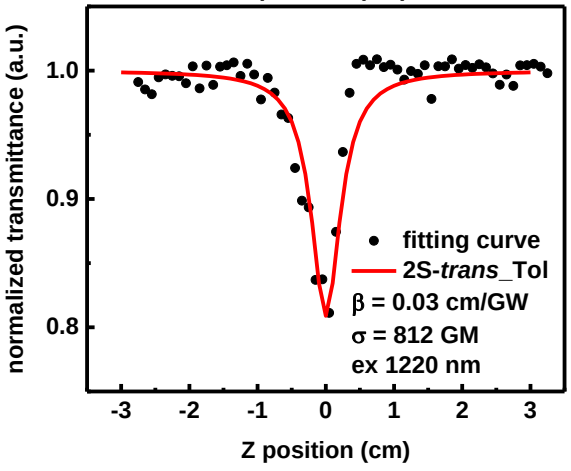

doi:10.6342/NTU202201631

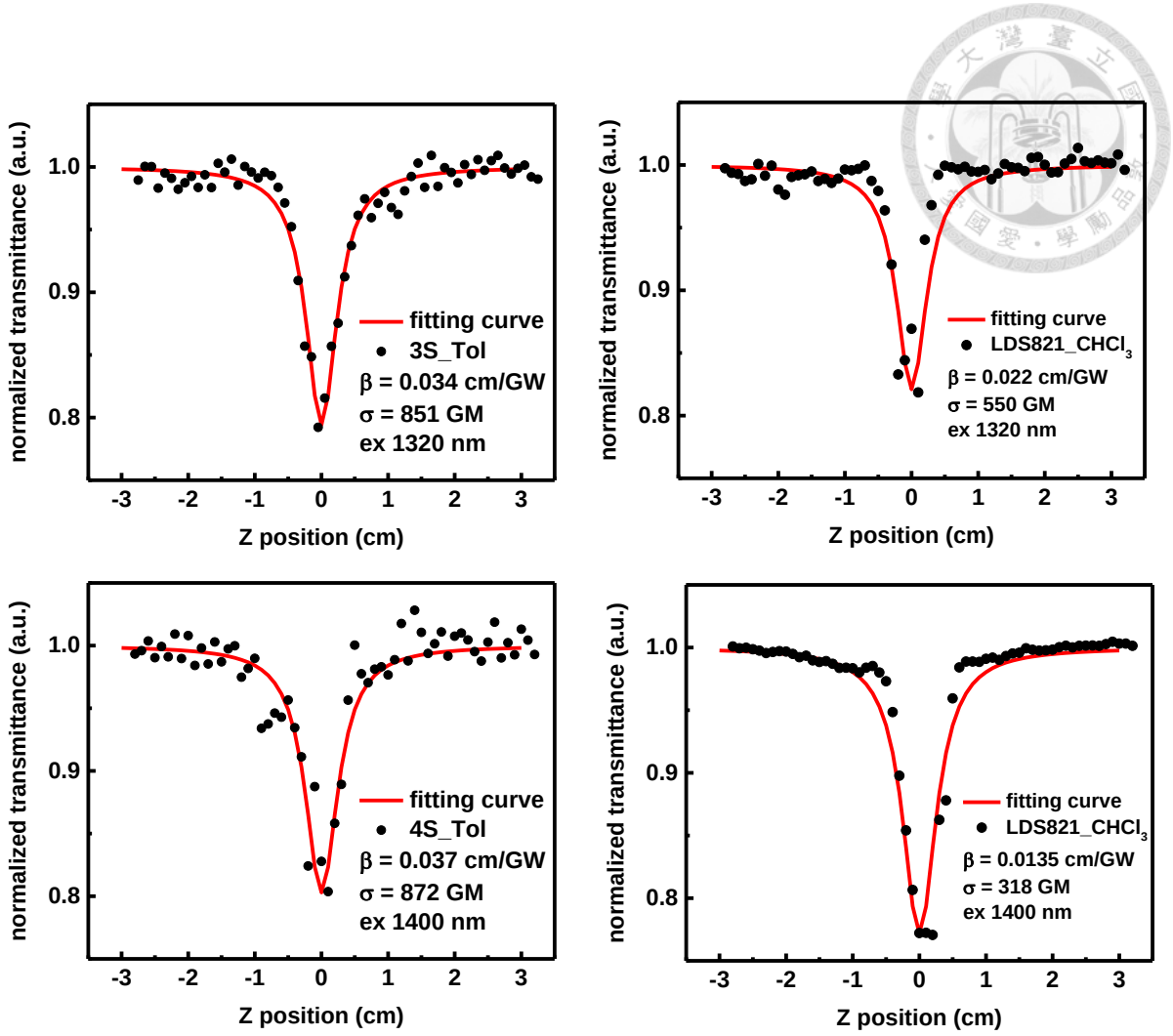

Figure S2-20. Two-photon absorption spectrum

doi:10.6342/NTU202201631

2.6.2.5 Transient Absorption Spectrum

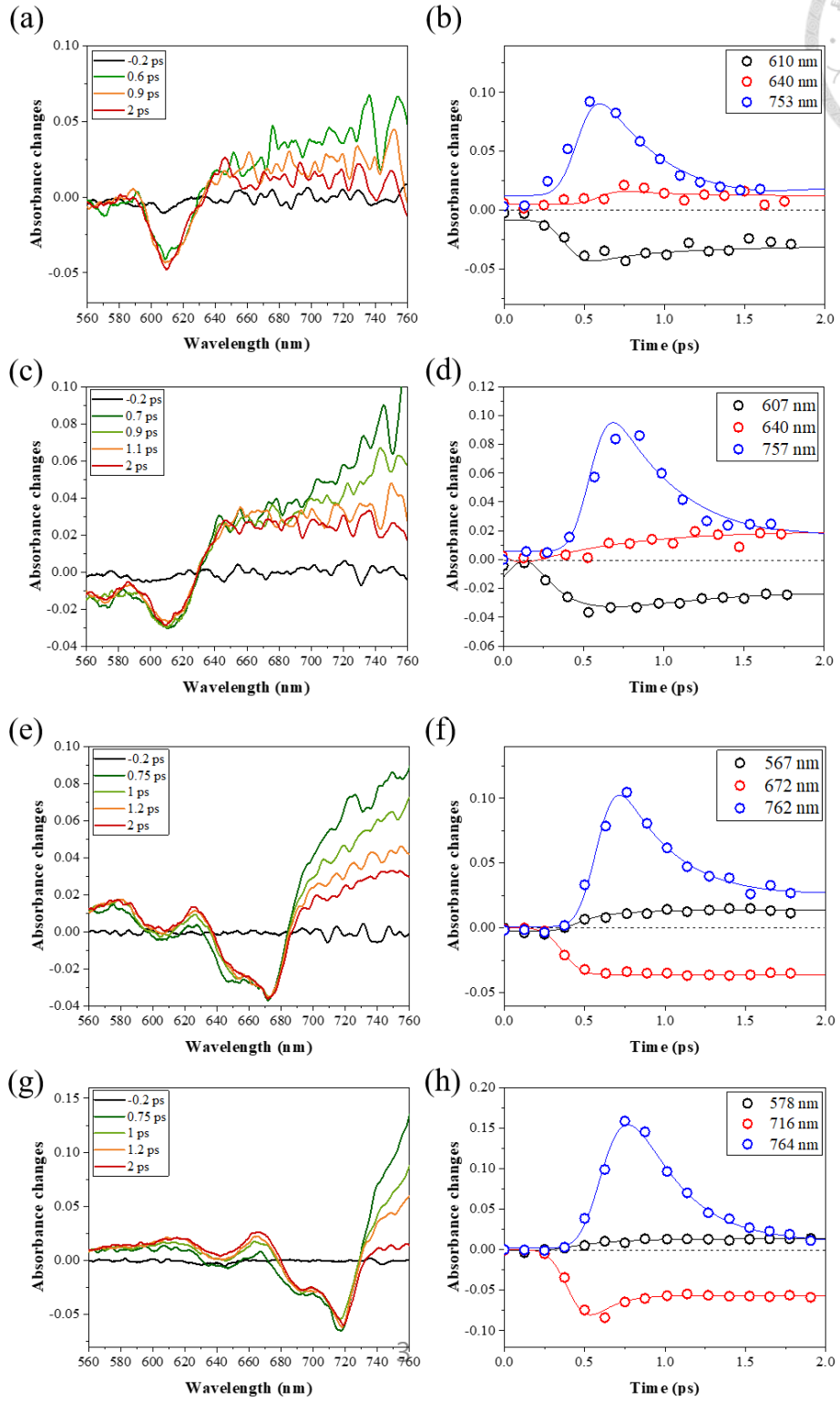

Figure S2-21. Temporal evolution of n**S-PDI-D**s in toluene and the relaxation dynamics of the transient absorption for n**S-PDI-Ds** at various selected wavelengths **2S-*cis*-PDI-D**

doi:10.6342/NTU202201631

(a and b, λ_{ex}: 610 nm), **2S-*trans*-PDI-D** (c and d, λ_{ex}: 610 nm), **3S-PDI-D** (e and f, λ_{ex}: 650 nm) and **4S-PDI-D** (g and h, λ_{ex}: 650 nm)

2.6.3 Theoretical Calculation

All calculations were performed with the Gaussian 16 package at M062X/6-311+G(d,p) level. Density function theory (DFT) calculations were carried out for structural optimization. The energy minima were affirmed with no imaginary frequencies by vibrational frequency calculations. Optical excitation energies and frontier molecular orbitals were obtained by time-dependent density functional theory (TD-DFT) method. Natural transition orbitals (NTOs) are evaluated to characterize the nature of the first excited singlet and triplet states for those with complex transition compositions. The solvent effects were considered using the polarizable continuum model (PCM) with toluene as solvent. Spin-orbit coupling constant are computed by ADF (Amsterdam Density Functional) version 2020.

Table S2-1. NTO analysis of the first excited singlet states (S_1) and triplet states (T_1) for n**S-PDI-D**s

	state	weight	Hole	Electron
1S-PDI-D	S_1	99.9 %	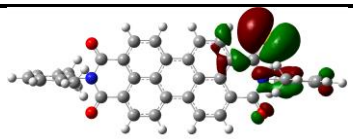	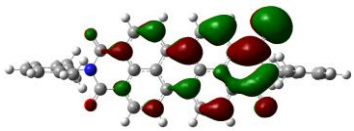
	T_1	95.3 %	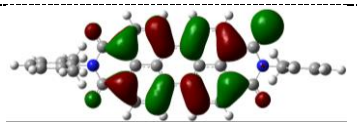	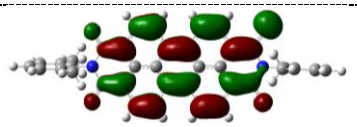

doi:10.6342/NTU202201631

2S-*cis*-PDI-D	S_1	74.4 %	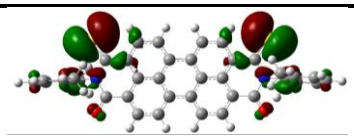	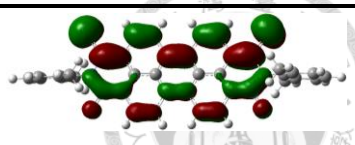
		25.6 %	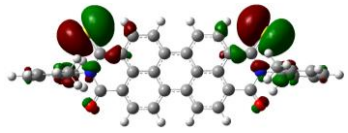	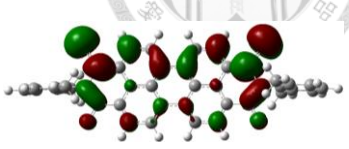
	T_1	94.9 %	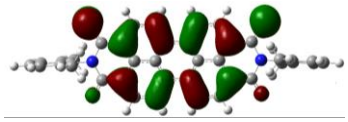	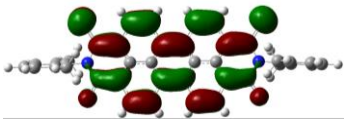
2S-*trans*-PDI-D	S_1	72.4 %	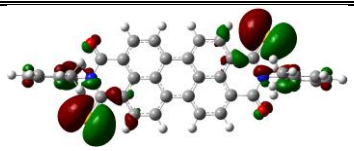	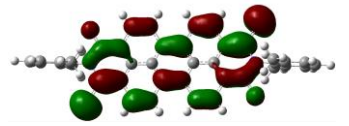
		27.6 %	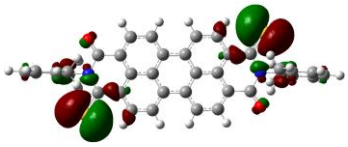	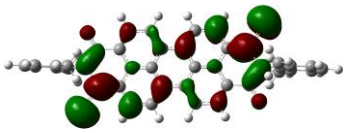
	T_1	94.7 %	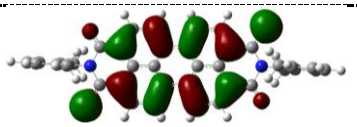	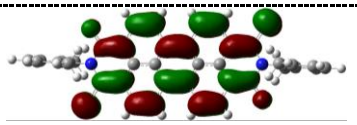
3S-PDI-D	S_1	94.3 %	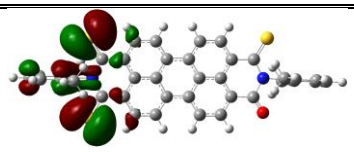	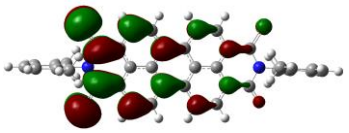
	T_1	96.1 %	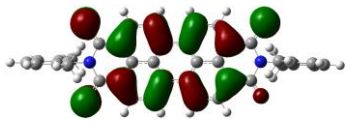	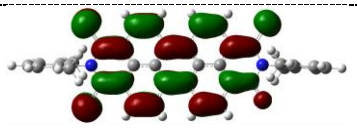
4S-PDI-D	S_1	73.6 %	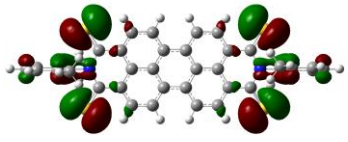	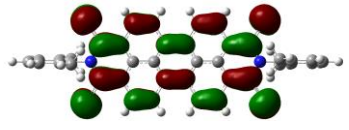
		21.0 %	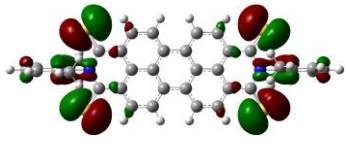	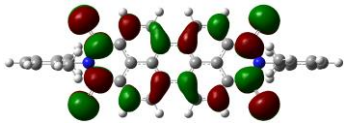

doi:10.6342/NTU202201631

	T_1	97.0 %	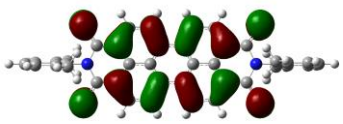	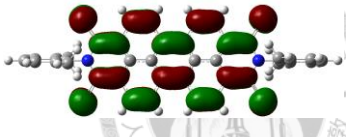

Table S2-2. Optical excitation and molecular orbital contributions for the S_0-optimized and S_1-optimized structures of **nS-PDI-D**s

		no.	E/eV	nm	f	Contribution	weight
1S-PDI-D	**Absorption (@S_0-opt)**	S_1	2.24	553.6	0.0002	HOMO-1→LUMO	63%
						HOMO-1→LUMO+1	22%
		S_2	2.44	507.3	1.2074	HOMO→LUMO	98%
		T_1	1.44	859.0	0	HOMO→LUMO	95%
		T_2	2.03	611.7	0	HOMO-1→LUMO	58%
						HOMO-1→LUMO+1	24%
	Emission (@S_1-opt)	S_1	1.64	754.9	0.0001	HOMO-1→LUMO	73%
						HOMO-1→LUMO+1	15%
		S_2	2.19	565.4	1.2284	HOMO→LUMO	95%
		T_1	1.10	1124.0		HOMO→LUMO	94%
		T_2	1.47	845.6	0	HOMO-1→LUMO	69%
						HOMO-1→LUMO+1	17%
2S-trans-PDI-D	**Absorption (@S_0-opt)**	S_1	2.22	558.7	0.0001	HOMO-2→LUMO+1	23%
						HOMO-1→LUMO	60%
						HOMO-1→LUMO+4	7%
		S_2	2.22	557.3	0	HOMO-2→LUMO	59%
						HOMO-2→LUMO+4	7%
						HOMO-1→LUMO+1	23%

doi:10.6342/NTU202201631

		T_1	1.32	935.4	0	HOMO-5→LUMO+1	5%
						HOMO→LUMO	94%
		T_2	2.01	617.2	0	HOMO-2→LUMO+1	24%
						HOMO-1→LUMO	54%
						HOMO-1→LUMO+4	8%
		S_1	1.60	772.5	0.0001	HOMO-1→LUMO	74%
						HOMO-1→LUMO+1	16%
		S_2	2.06	603.3	1.3684	HOMO→LUMO	98%
	Emission	T_1	1.00	1244.2	0	HOMO→LUMO	97%
	(@S_1-opt)					HOMO←LUMO	7%
		T_2	1.43	865.7	0	HOMO-1→LUMO	69%
						HOMO-1→LUMO+1	18%
						HOMO-1→LUMO+4	5%
		S_1	2.22	559.4	0.0021	HOMO-2→LUMO+1	20%
						HOMO-1→LUMO	60%
						HOMO-1→LUMO+2	5%
		S_2	2.22	559.1	0	HOMO-2→LUMO	60%
						HOMO-2→LUMO+2	5%
2S-*cis*-	**Absorption**					HOMO-1→LUMO+1	20%
PDI-D	**(@S_0-opt)**	T_1	1.32	939.4	0	HOMO→LUMO	94%
		T_2	2.01	618.2	0	HOMO-7→LUMO	5%
						HOMO-2→LUMO+1	22%
						HOMO-1→LUMO	55%
						HOMO-1→LUMO+2	6%

doi:10.6342/NTU202201631

	Emission (@S_1-opt)	S_1	1.60	776.9	0.0001	HOMO-1→LUMO	74%
						HOMO-1→LUMO+1	15%
		S_2	2.04	606.7	1.3477	HOMO→LUMO	98%
		T_1	0.98	1268.7	0	HOMO→LUMO	98%
						HOMO←LUMO	7%
		T_2	1.42	870.8	0	HOMO-1→LUMO	70%
						HOMO-1→LUMO+1	16%
3S- PDI-D	**Absorption (@S_0-opt)**	S_1	1.84	675.3	0.0001	HOMO→LUMO	71%
						HOMO-1→LUMO+1	16%
		S_2	2.14	579.3	1.3814	HOMO→LUMO	98%
		T_1	1.19	1043.2	0	HOMO→LUMO	95%
		T_2	1.64	755.4	0	HOMO-1→LUMO	66%
						HOMO-1→LUMO+1	17%
	Emission (@S_1-opt)	S_1	1.37	905.6	0.0001	HOMO→LUMO	80%
						HOMO→LUMO+1	12%
		S_2	1.94	637.8	1.4242	HOMO-1→LUMO	98%
		T_1	0.91	1355.7	0	HOMO-1→LUMO	100%
						HOMO-1←LUMO	8%
		T_2	1.21	1024.2	0	HOMO→LUMO	76%
						HOMO→LUMO+1	13%
4S- PDI-D	**Absorption (@S_0-opt)**	S_1	1.81	683.4	0.0002	HOMO-2→LUMO+1	19%
						HOMO-1→LUMO	68%
		S_2	1.82	681.4	0	HOMO-2→LUMO	68%
						HOMO-1→LUMO+1	20%

doi:10.6342/NTU202201631

		T_1	1.07	1155.0	0	HOMO-9→LUMO+1	5%
						HOMO→LUMO	96%
						HOMO←LUMO	5%
		T_2	1.62	764.2	0	HOMO-2→LUMO+1	20%
						HOMO-1→LUMO	63%
		S_1	1.33	929.5	0.0001	HOMO-1→LUMO	78%
						HOMO-1→LUMO+1	14%
		S_2	1.81	684.8	1.5078	HOMO→LUMO	98%
	Emission	T_1	0.78	1585.6	0	HOMO-9→LUMO+1	5%
	(@S_1-opt)					HOMO→LUMO	103%
						HOMO←LUMO	11%
		T_2	1.18	1051.6	0	HOMO-1→LUMO	73%
						HOMO-1→LUMO+1	15%

Table S2-3. NTO analysis of the first excited singlet states (S_1) and triplet states (T_1) for **nS-PDI-Ps**

	state	weight	Hole	Electron
1S-PDI-P	S_1	97.1 %	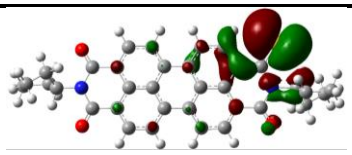	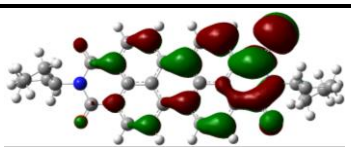
	T_1	95.4 %	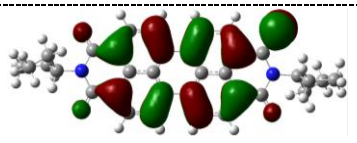	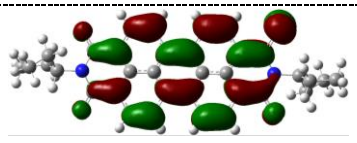
2S-*cis*-PDI-P	S_1	87.6 %	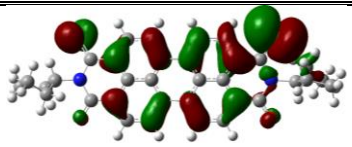	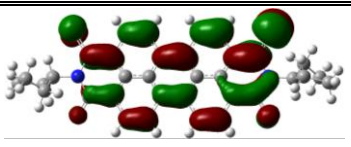

doi:10.6342/NTU202201631

		11.2 %	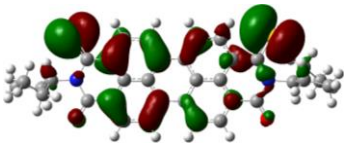	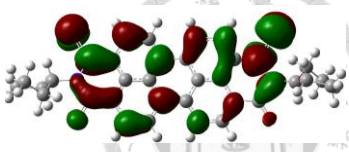
	T_1	94.9 %	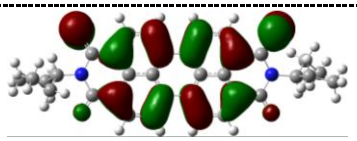	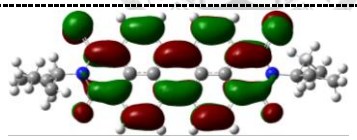
2S-*trans*-PDI-P	S_1	91.4 %	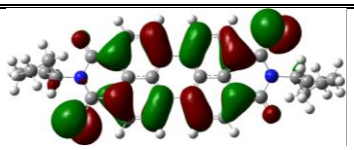	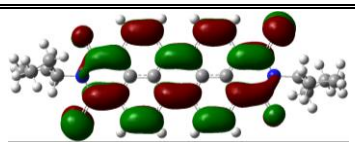
	T_1	94.9 %	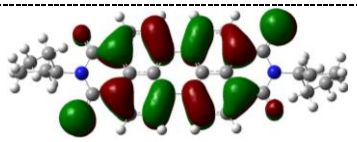	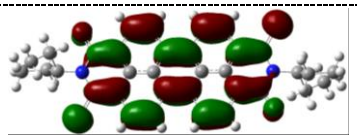
3S-PDI-P	S_1	89.5 %	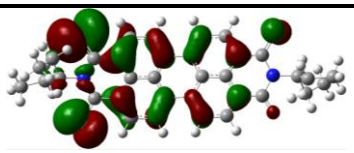	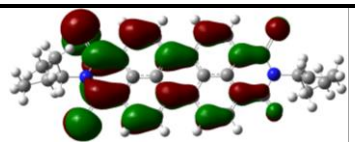
	T_1	95.8 %	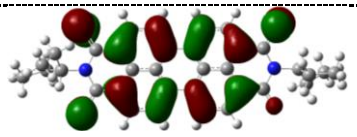	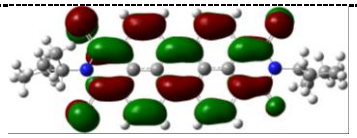
4S-PDI-P	S_1	91.1 %	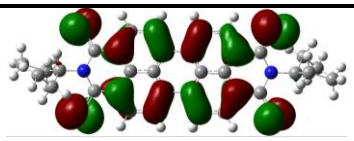	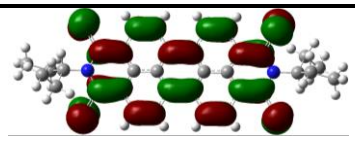
	T_1	96.5 %	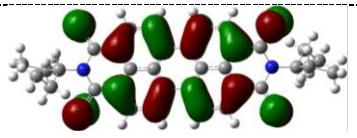	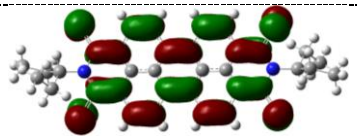

Table S2-4. Optical excitation and molecular orbital contributions for the S_0-optimized and S_1-optimized structures of **nS-PDI-Ps**

	no.	E/eV	nm	f	Contribution	weight
1S-PDI-P	S_1	2.36	524.4	0.1324	HOMO-1→LUMO	57%

doi:10.6342/NTU202201631

					HOMO-1→LUMO+1	22%
					HOMO→LUMO	14%
	S_2	2.46	504.0	0.9996	HOMO-1→LUMO	10%
					HOMO→LUMO	84%
	T_1	1.45	855.2	0	HOMO→LUMO	95%
	T_2	2.17	573.0	0	HOMO-1→LUMO	63%
					HOMO-1→LUMO+1	27%
	S_1	2.28	543.2	1.0019	HOMO-2→LUMO+1	5%
					HOMO-1→LUMO	10%
					HOMO→LUMO	81%
2S-*trans*-	S_2	2.36	525.8	0	HOMO-2→LUMO	63%
PDI-P	T_1	1.33	928.9	0	HOMO→LUMO	94%
	T_2	2.14	579.5	0	HOMO-2→LUMO	55%
					HOMO-2→LUMO+4	9%
					HOMO-1→LUMO+1	24%
	S_1	2.26	549.6	0.6025	HOMO-1→LUMO	25%
					HOMO-1→LUMO+1	11%
					HOMO→LUMO	53%
	S_2	2.32	535.5	0.3977	HOMO-2→LUMO	9%
2S-*cis*-PDI-P					HOMO-1→LUMO	36%
					HOMO-1→LUMO+1	11%
					HOMO→LUMO	30%
	T_1	1.33	935.0	0	HOMO→LUMO	94%
	T_2	2.07	599.4	0	HOMO-1→LUMO	57%

doi:10.6342/NTU202201631

					HOMO-1→LUMO+1	24%
3S-PDI-P	S_1	2.08	595.0	0.5448	HOMO-1→LUMO	31%
					HOMO-1→LUMO+1	10%
					HOMO→LUMO	49%
	S_2	2.19	565.0	0.7122	HOMO-1→LUMO	36%
					HOMO-1→LUMO+1	7%
					HOMO→LUMO	47%
	T_1	1.20	1034.2	0	HOMO→LUMO	95%
	T_2	1.91	650.0	0	HOMO-1→LUMO	61%
					HOMO-1→LUMO+1	16%
4S-PDI-P	S_1	1.98	624.8	1.0564	HOMO-2→LUMO	8%
					HOMO-1→LUMO+1	5%
					HOMO→LUMO	82%
	S_2	2.11	586.6	0	HOMO-2→LUMO+1	20%
					HOMO-1→LUMO	63%
	T_1	1.08	1144.5	0	HOMO→LUMO	96%
	T_2	1.87	663.8	0	HOMO-2→LUMO+1	18%
					HOMO-1→LUMO	56%
					HOMO→LUMO+1	6%

doi:10.6342/NTU202201631

2.6.4 Cell Culture

2.6.4.1 Materials and Methods

Bioresource Collection and Research Center (BCRC) (Hsinchu, Taiwan) obtained four cell lines: A549 (ATCC, CCL-185™), WI-38, IMR90 and HEL299 cells] in this study. A549 cells were grown in a humidified controlled system that contained 5 % CO_2 at 37°C with DMEM media contained with sodium pyruvate (100 mg/L), L-glutamine (550 mg/L), 1 % penicillin-streptomycin and 10 % FBS.The growth medium was refreshed every two days, and cells were sub-cultured and trypsinized with 0.1 % trypsin when they grew to about 90 % confluence. Trypan blue solution, trypsin and 1-(4,5-Dimethylthiazol-2-yl)-3,5-diphenylformazan (MTT) were obtained from Sigma-Aldrich (St. Louis, MO, USA).Dimethylsulfoxide (DMSO) came from J.T. Baker (Phillipsburg, New Jersey, USA). Dulbecco's Modified Eagles Medium (DMEM) media (high glucose), Fetal Bovine Serum (FBS), and penicillin-streptomycin were purchased from Life Technologies (Carlsbad, CA, USA)

2.6.4.2 Procedure of DPBF assay

Stock DPBF solution (250 μM) in DMSO was prepared and added in 96-well plate. DPBF solution in each well was treated with different doses (0.0, 2.0, 4.0 ,8.0 μM). After different degree of photoactivation (0, 2, 4, 8 minutes), the whole well was detected by Bio-Rad microplate at 415 nm. Remaining DPBF % was calculated as follow: Remaining DPBF% = $(A_{sample}-A_{blank})/(A_{control}-A_{blank})$ x 100%

A_{sample}, $A_{control}$ and A_{blank} represented the absorption of cells containing **1S-FC131**, without **1S-FC131** and neither **1S-FC131** or DPBF solution.

doi:10.6342/NTU202201631

2.6.4.3 Procedure of MTT assay

In a 96-wells plate, A549 cells were seeded around a density of 10^4 per well and then retained carefully in a cell incubator at 37℃ for one day before addition of designated drugs.Stork **1S-FC131 or Cy5-1S-FC131** was mixed in DMSO at first and then added in culture medium at a ratio of 1:99 prior to use. The various dosage of **1S-FC131** from 0 to 8 μM (**Cy5-1S-FC131** from 0 to 24 μM) was mixed in A549 cells. After photoactivation of **1S-FC131** or **Cy5-1S-FC131** (590 nm LED light, 0 to 8mins), the dishes were retained in incubator for another 24 h. Finally, 0.5mg/ml MTT reagent in PBS were added to each well. After incubating the cell for 2 h, the medium was removed and then DMSO was added to each well. At last, the absorbance wavelength at 570nm was measured in DMSO by Bio-Rad microplate reader. Cell viability was calculated by equation as below:

Cell viability (%) = $(A_{sample}- A_{blank})/(A_{control}-A_{blank})$ x 100%

A_{sample}, $A_{control}$ and A_{blank} represented the absorption of cells containing **1S-FC131** (**Cy5-1S-FC131)**, without **1S-FC131** (**Cy5-1S-FC131**) and neither **1S-FC131** (**Cy5-1S-FC131)**

IC_{50} was calculated by the trendline equation from cell viability(y) and concentration(x) under 8 minutes.

2.6.4.4 Procedure of selective experiment

In a 96-wells plate, four cell lines (A549, WI-38, IMR90 and HEL299 cells) were seeded around a density of 10^4 per well and then retained carefully in a humidified controlled incubator at 37 ℃ for one day before addition of designated drugs. Stork **1S-FC131** was mixed in DMSO first and then added with culture medium at a ratio of 1:99 prior to use. 8μM **1S-FC131** was incubated in 3 different cells and waited 6 h for affinity binding. After completion of binding, the dishes were irradiated with LED (590nm LED light, 8mins) and retained in cell incubator for another 24 h. Finally, 0.5 mg/ml MTT

doi:10.6342/NTU202201631

reagent in PBS were added to each well. After incubating the cell for 2 h, the medium was removed and then DMSO was added to each well. At last, the absorbance wavelength at 570nm was measured in DMSO by Bio-Rad microplate reader. Cell viability was calculated by equation as below:

Cell viability (%) = $(A_{sample}- A_{blank})/(A_{control}-A_{blank})$ x 100%

A_{sample}, $A_{control}$ and A_{blank} represented the absorption of cells containing **1S-FC131**, without **1S-FC131** and neither **1S-FC131** or cells

2.6.4.5 Procedure of Cell Apoptosis

For cell apoptosis experiment, four confocal dished seeded 1 $x10^4$ a549 cells and culture for 18 h. Then four dishes were conducted in different treatment: group 1 for control, group 2 only for under irradiation in 8minutes, group 3 only for incubation with 8μM **1S-FC131** for 1, group 4 treatment for **1S-FC131**(8μM) and 8 minutes irradiation. After waiting 1 h, the four dishes were staining by Calcein AM (2μM) and Propidium Iodide (2μM) and waited for another 1 h, and then washed by PBS three times. The imaging was taken under 63 immersion lenses with the 1024x1024 resolution at 1000 nm two-photon excitation in the confocal microscopy.

2.6.4.6 Procedure of Cocultured experiment

For the cocultured experiment, in the beginning, A549 cells and WI-38 cells were cocultured in the confocal dishes with fence that could separate dished into two space. The fence was removed after 18 h and keep culture for 6 h. After the dish was conducted in the same condition of group 4, it was stained by Calcein AM (2μM) and Propidium Iodide (2μM) and waited for another 1 h, and then washed by PBS three times. The imaging was taken under 63 immersion lenses with the 1024x1024 resolution at 1000 nm

doi:10.6342/NTU202201631

two-photon excitation in the confocal microscopy.

2.6.4.7 Intramolecular ROS assay

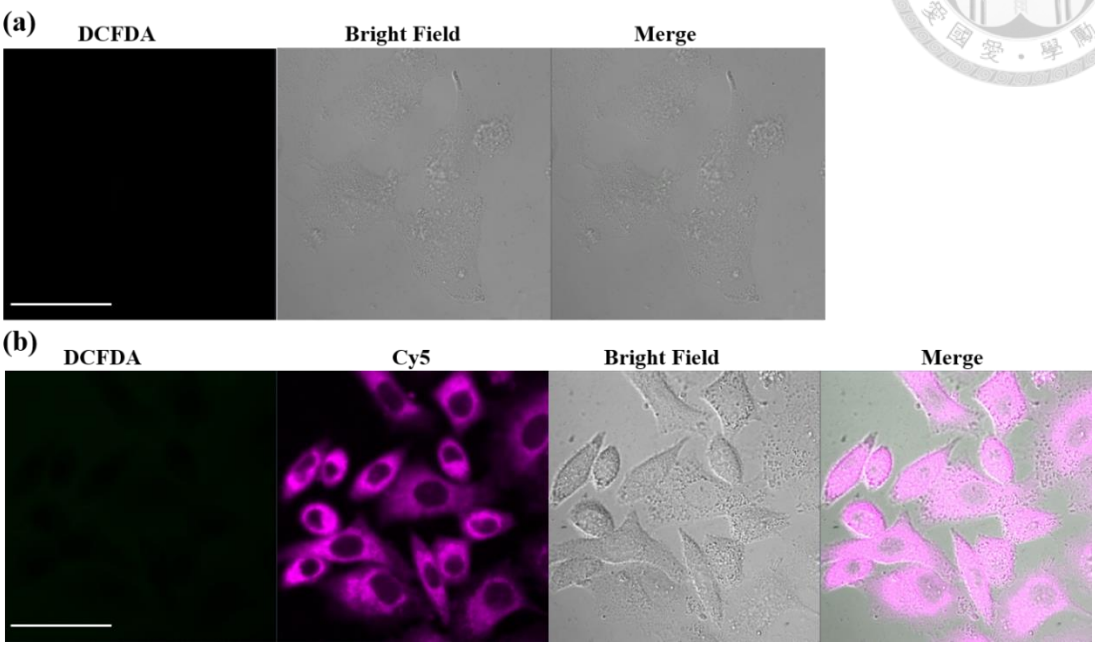

Figure S2-22. Intracellular ROS (hydroxyl radical (•OH) and peroxynitrite ($ONOO^-$)) was determined by DCFDA assay. Confocal microscopic images of A549 cells treated with (a) **1S-FC131** and (b) **Cy5-1S-FC131.** (DCFDA, λ_{ex}: 488 nm) (515-540 nm) (Cy5, λ_{ex}: 488 nm & 633 nm) (650-700 nm) scale bar: 50 μm.

doi:10.6342/NTU202201631

2.6.5 *In vivo* Experiment

A549 cells (1×10^7 cells/mL) were subcutaneously injected into the right upper back of NU/NU male mice (4 weeks old). Mice were kept in IVC (individually ventilated cage) with fresh gas supply. After 1-week tumor growth, mice were grouped (4 mice in each group) for various treatments as described follows: (1) Control (PBS buffer), (2) **1S-FC131** (100 μL, 2 mg/mL) only or **Cy5-1S-FC131** (100 μL, 6 mg/mL) only, (3) Light only (20 min irradiation, 200 mW/cm2), (4) **1S-FC131** (100 μL, 2 mg/mL) or **Cy5-1S-FC131** (100 μL, 6 mg/mL) with light (20 min irradiation, 200 mW/cm^2). Tumor volume was measured using digital calipers every other day, and estimated by the formula: Tumor volume= length × width^2 × 0.5, where length represents the largest tumor diameter and width represented the perpendicular tumor diameter.

In addition, record of weight variations of mice was also carried out every two days. After 14 days, mice were sacrificed and the tumors were removed. Tumor weight and size were then measured. All *in vivo* studies followed and approved by National Taiwan University Institutional Animal Care and Use Committee

doi:10.6342/NTU202201631